

# UW – NANOLAB – Research Activities

**René M. Overney**

Professor

Department of Chemical Engineering

University of Washington

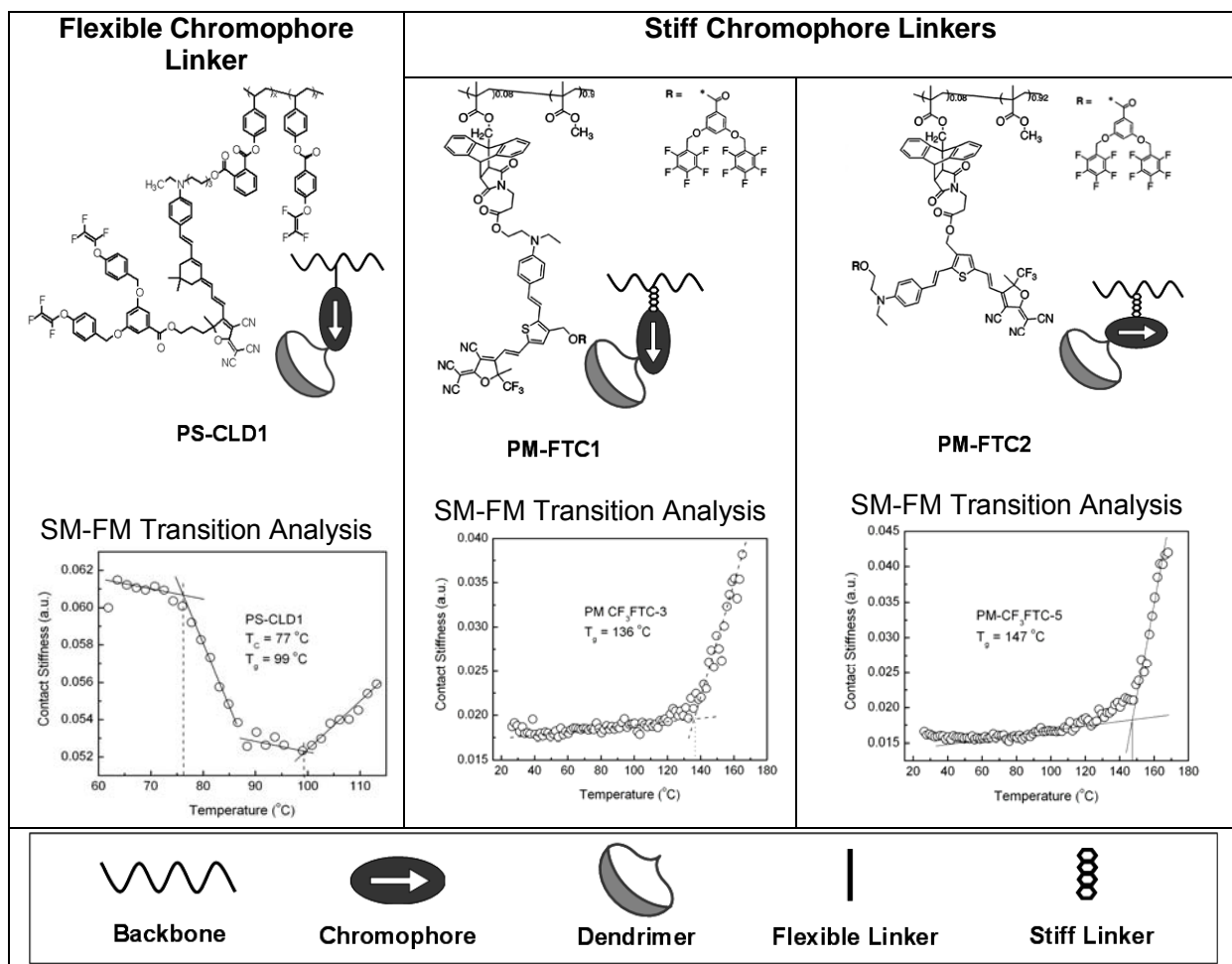
Seattle, WA 98195

## Index

<b>1. Intra- and Intermolecular Constraints.....</b>	<b>2</b>
1.1 Molecular Origin of Transition Phenomena – Enthalpic Processes .....	3
1.2 Cooperativity During the Glass Forming Process – Entropic Processes.....	5
1.3 Self-Assembly Processes – Combined Enthalpic and Entropic Processes.....	7
<b>2. Interfacial and Dimensional Constraints .....</b>	<b>11</b>
2.1 Low Dimensional Flow – Wetting and Dewetting of Polymer Films .....	11
2.1.1 <i>Interfacial Excess Energy Induced Dewetting</i> .....	12
2.1.2 <i>Finite Size Systems – Ultrathin Films</i> .....	13
2.2 Glass Transition in Ultrathin Films .....	15
2.3 Interfacial Dimensional Constraints - Entropic Cooling in Simple Liquids .....	17
<b>3. Tribology Fundamentals .....</b>	<b>19</b>
3.1 Tribo-Dissipation Involving Intramolecular Constraints .....	20
3.2 Liquid-Lubrication: Molecular, Interfacial and Dimensional Constraints.....	24
3.3 Two-Dimensional Polymer Liquids and Reaction Kinetics .....	26
<b>4. Technological Applications - Nanotechnology.....</b>	<b>28</b>
4.1 Electro-Optics .....	29
4.1.1 <i>Organic Optoelectronics</i> .....	29
4.1.2 <i>Photonics</i> .....	32
4.2 Membrane Technology .....	34
4.2.1 <i>PEM Fuel Cell</i> .....	34
4.2.2 <i>Nanocomposite Membranes</i> .....	39
4.3 Digital Storage – Thermomechanical Ultrahigh Density Recording .....	43
<b>5. Classification and Summary.....</b>	<b>47</b>
<b>6. References and Citations Therein.....</b>	<b>49</b>

## 1. Intra- and Intermolecular Constraints

Condensed organic materials designed for nanotechnological applications are impacted significantly by internal and external constraints. Internal (intra- and intermolecular) constraints are inherent to the molecular architecture, and generally result from direct bonding, electrostatic interactions, or steric effects. Internal constraints can be incorporated *a priori* into molecular designs, as a prescription for desired material properties. This is illustrated in Fig. 1-1 with our work on organic non-linear optical (NLO) material systems for photonic application,<sup>4</sup> where the “minuscule” flexibility difference in a intramolecular linker within a vast macromolecule is responsible for a significant alteration of the relaxational phase behaviour below the glass transition at  $T_c = 77$  °C. Studies such as this, involving internal molecular constraints make an important aspect of our research. They involve novel sophisticated nano-tools and methodologies, and are carried out in parallel to material synthesis and recently also computer modelling.

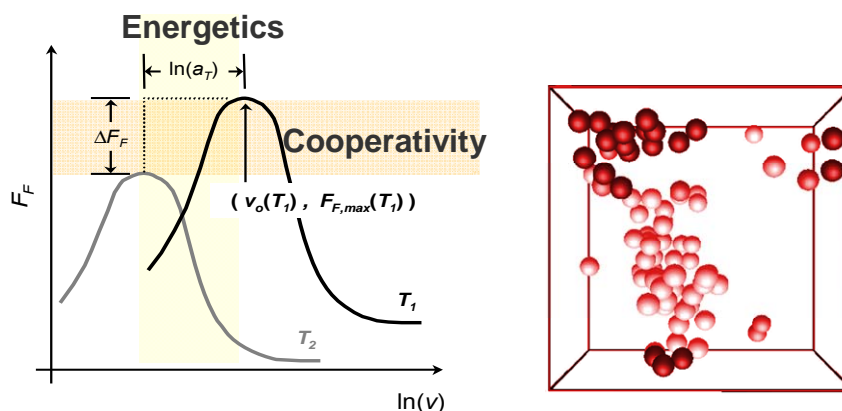


**Fig. 1-1:** Shear modulation force microscopy (SM-FM) analysis of of side-chain dendronized NLO polymers. *Left:* PS-CLD1 with soft chromophore-backbone linker; *Right:* PM-FTC1 and PM-FTC2 with stiff linkers.<sup>4</sup>

Reflecting on effective material design concepts, a bottom-up molecular approach comes to mind, where, with the appropriate synthesis and under suitable processing conditions, materials are designed with desired properties and functionalities. The challenge is to anticipate bulk- or mesophase material properties from the molecular structure. This is generally approached in a reversed fashion by first analyzing the product, i.e. the condensed phase, and then pondering the possible molecular origin for specific properties. Depending on the specificity of the information gained experimentally, a molecular understanding is directly obtained, a molecular model is

developed, or a trial-and-error procedure is put in place. Once a molecular understanding (or a molecular model) for a specific class of materials is obtained, computer assisted molecular engineering can take place, and a wide variety of molecular structures and functionalities directed towards the material design objective can be tested. Thus, to excel from mere trial-and-error procedures and empiricism, experimental tools and methodologies have to be devised that provide direct access to nanoscale mobilities of constrained systems.

Over the past decade our group has pioneered various instrumental techniques that have provided insight into the nanoscale behaviour of constrained materials. In regards of inter- and intramolecular material intrinsic constraints, we introduced a method that is sensitive to the intrinsic friction process, not unlike the Stokes-Einstein friction mobility concept. Our method, referred to as *Intrinsic Friction Analysis (IFA)*,<sup>8</sup> is based on lateral force microscopy<sup>9</sup>. With IFA, we have been studying the energetics and cooperativity of inter- and intramolecular mobilities that are available within well defined temperature windows, Fig. 1-2.



**Fig. 1-2:** *Left:* IFA schematic friction-velocity isotherms that if shifted accordingly (linear superposition principle) reveal energetic and cooperative information.<sup>1,8</sup> *Right:* Schematic visualization of monomer clustering during a relaxation process. IFA combined with dielectric spectroscopy provides a direct method to determine the “cluster” length dimension that corresponds to computer simulations.<sup>8</sup>

Over the past few years, we have employed the IFA technique to a wide variety of materials to illuminate phenomenological processes from a submolecular perspective.<sup>1,3,4,8,10</sup> Besides the fundamental analysis of transition phenomena, we have explored temporal and spatial cooperative phenomena and self-assembly mechanisms. Furthermore, IFA provided first truly molecular scale insight into the material intrinsic activation modes that are cause for energy dissipation during tribological sliding (c.f. subsection 3.1 below).

Some of our striking results involving IFA and other techniques are discussed in this section with specific foci on

- *enthalpic relaxation processes*, as found for side-chain relaxations in condensed organic matter,
- *entropic relaxation processes*, of particular relevance for glass forming materials, and
- *combined enthalpic and entropic processes*, discussed below on self-assembling molecular glasses.

### 1.1 Molecular Origin of Transition Phenomena – Enthalpic Processes

Transition analysis as conducted with differential scanning calorimetry, shear modulation force microscopy (SM-FM – discussed in greater detail below), electron spin resonance and other methods identify temperature regimes with critical boundaries (i.e., transition temperatures). To unravel underlying molecular mechanisms describing the transition in greater detail demands additional mobility analyses, such as dielectric spectroscopy, neutron reflectivity, or as addressed above, IFA. If

the material is confined to thin films, IFA is because of its high signal-to-noise ratio, the preferred technique. The insightful information towards a cognitive molecular design approach (versus trial-and-error) that can be obtained with IFA shall here be illustrated with our research on thin film polymeric NLO materials.<sup>6</sup>

As shown above, the dendronized side-chain NLO chromophore system PS-CLD1, Fig. 1-1, reveals a low temperature transition  $T_c$  at 77 °C. This transition turns out to be crucial for the acentric alignment of the dipolar chromophores, as it provides rotational mobility to the chromophore side-chain. The properties that are of foremost importance for organic NLO materials are the electro-optical (EO) activity that involves an acentric order of the chromophores, and temporal phase stability. One main approach in generating acentric order within NLO systems is to perform an electric field poling process, in which the randomly dispersed chromophores are aligned. For electric field poling, the glass transition temperature ( $T_g$ ) is a key parameter with regard to both the *poling efficiency*, requiring high chromophore mobility often only available near  $T_g$ , and the *temporal stability* of the acentric order, demanding minimal chromophore mobility. These two contradicting factors make the molecular design of NLO systems challenging, requiring many levels of subtle adjustments for device optimization. The induced macroscopic nonlinearity is usually expressed with the electro-optical (E-O) coefficient  $r_{33}$  that is given as

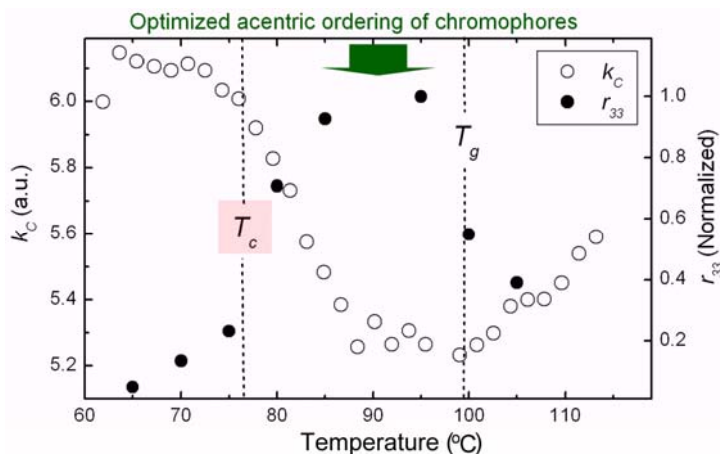
$$r_{33} = \frac{|2N \cdot f(\omega) \cdot \beta \langle \cos^3 \theta \rangle|}{n^4} \quad (1.1)$$

where  $n$  is the refractive index,  $N$  is the chromophore number density,  $f(\omega)$  is the local field factor,  $\beta$  is the second order hyperpolarizability, and  $\langle \cos^3 \theta \rangle$  is the Boltzmann angle averaged order parameter.

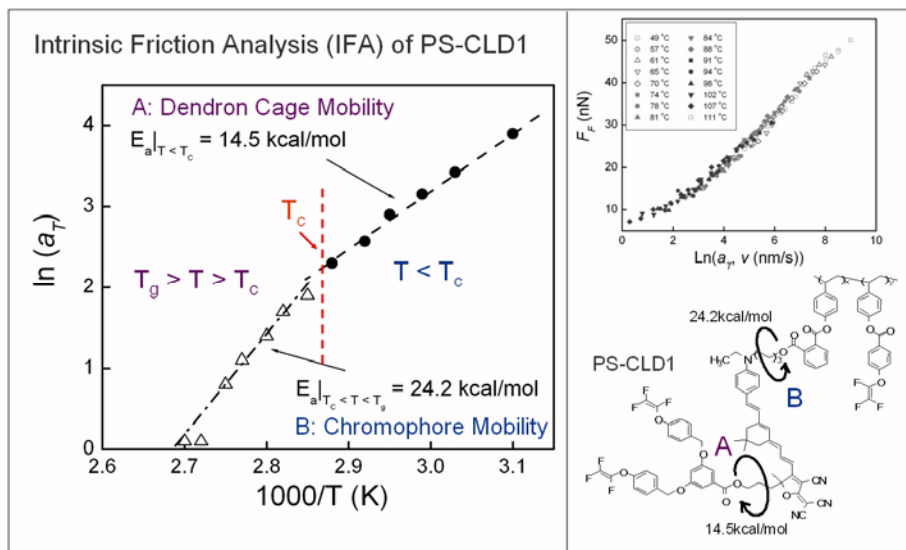
Figure 1-3 illustrates the importance of the low temperature transition  $T_c$ . It can be inferred that the EO coefficient,  $r_{33}$ , significantly increased above  $T_c$ , thus, leading to an improved poling efficiency within  $T_c$  and  $T_g$ . The observed decrease in  $r_{33}$  above  $T_g$  can be attributed to a detrimental effect of excessive large scale mobility (in this case the polymer backbone translational motion) that leads to chromophore pairing, and thus, dipole annihilation. This study is witness to the subtle temperature dependence involving poling of organic NLO materials.

To provide insight into the origin for the beneficiary temperature window ( $T_c$ ,  $T_g$ ), we conducted a mobility analysis involving IFA. Figure

1-4 shows two distinct temperature regimes based on the activation energy signature ( $E_a$ ). The two regimes are separated at the critical transition temperature  $T_c$ . The obtained values for the activation energies were comparable to the dendrimer mobility **A** and the rotational chromophore segmental motion **B** below and above  $T_c$ , respectively. If compared to the two other dendronized side-chain NLO chromophore systems PM-FTC1 and PM-FTC2, introduced in Figure 1-1, which lack a low temperature transition due to stiff side-chain linkages, the critical secondary relaxation at the flexible linkage **B** to the chromophore side-chain results, for PS-CLD1, in the desired chromophore mobility for electric field poling within the temperature window ( $T_c$ ,  $T_g$ ).



**Fig. 1-3:** SM-FM contact stiffness  $k_c$  data (●) from Fig. 1.1 in PS-CLD1 superimposed with corresponding EO activity coefficients,  $r_{33}$  (○). Optimized acentric ordering within  $T_c$  and  $T_g$ .<sup>6</sup>



**Figure 1-4:** Left: IFA Arrhenius plot of the shift factor  $a_T$  employed to superimpose the friction-velocity isotherms to a single master curve, revealing two distinct activation energies. Right/Top: Master curve according to the superposition principle. Right/Bottom: PS-CLD1 model with rotational energy values that correspond to the IFA activation energies.<sup>4</sup>

This study illustrates the immense potential of IFA for investigating inter- and intramolecular mobilities in constrained and finite-size systems.

It is important to note that our discussion involving side-chain relaxations, considers enthalpic contributions to motion only. Contributions from entropic processes are discussed in the next section. Thermally activated enthalpic processes are time-temperature equivalent, i.e., time and temperature are equivalent to the extent that data (in our case friction) at one temperature can be superimposed on data at another temperature by shifting the curves (isothermal friction-velocity plots) by  $a_T$  along the log time axis to a single master curve as shown in Figure 1-4 (Right/Top). The set of horizontal shifts  $\{a_T\}$ , of friction-velocity isotherms, also referred to as thermal shift factors, provides the actual activation energies  $E_a$ , if plotted versus the inverse absolute temperature  $T$ , from

$$E_a = -R \left[ \frac{\partial \ln(a_T)}{\partial (1/T)} \right]_p \quad (1.2)$$

$R$  is the universal gas constant. This log-linear relationship is known as Arrhenius behavior. It should be noted that relaxation phenomena exist that are non-Arrhenius, as found for polymer rubbers above the glass transition temperature (c.f. sec. 1.2). In particular in nano-constrained systems, relaxation processes can also be highly cooperative, which leads to an entropic increase in the “apparent” activation energy.

### 1.2 Cooperativity During the Glass Forming Process – Entropic Processes

While non-cooperative processes, such as observed for side-chain relaxation, Fig. 1-4, are described in terms of the dynamic enthalpy  $\Delta H^*$  alone, cooperative processes also include the dynamic entropy,  $\Delta S^*$ , as given by the activation Gibbs free energy:

$$\Delta G^* = \Delta H^* - T\Delta S^* \quad (1.3)$$

Examples are long-range mobilities, such as the crankshaft motion in polymers during the glass forming process that yield strongly cooperative phenomena. Figure 1-2(Left) illustrates this in the IFA analysis that makes vertical shifting,  $\Delta F_F$ , necessary to collapse the data to a single master curve. As derived by our group,<sup>1</sup> frictional vertical shifting,  $\Delta F_F$ , can be related to the dynamic entropy via,

$$\Delta F_F \approx -\frac{T\Delta S^*}{\phi'} \quad (1.4)$$

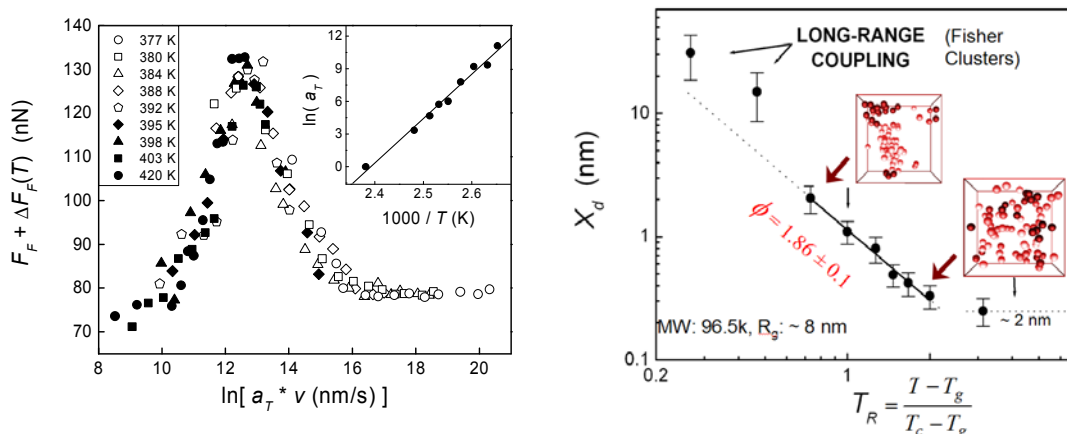
where  $\phi'$  is the contact area normalized stress activation volume. Thus, while horizontal shift factors,  $\{a_T\}$ , relate to the enthalpic behavior of the system, the vertical shift factors  $\Delta F_F$ , relate to entropic cooperative behavior. The deconvolution of the two processes is inaccessible with conventional techniques but exclusive to IFA. Thus with direct access to the molecular mobility, we investigated the very complex process of glass forming.<sup>8</sup>

Since Adam and Gibbs (*J. Chem. Phys.* (1965) **43**, 139), structural relaxation near the glass transition has been visualized in terms of a correlated motion of polymer segments or domains, giving rise to dynamic heterogeneities. While the time scale of dynamic heterogeneities can be directly inferred from scattering experiments, the size of the cooperatively rearranging regions (typically 1-3 nm) is generally not directly obtainable and involves model assumptions. A nanoscopic description of polymer dynamics involves, in general, only two parameters: an appropriate macromolecular length scale and an internal, or monomeric, friction coefficient.

We employed IFA on a polymer rubber melt (polystyrene) close to its glass transition ( $T_g = 373$  K), which resulted in the data presented in Figure 1-5(Left).<sup>8</sup> The log-linear averaged activation energy of  $\sim 90$  kcal/mol coincides well with the apparent activation energy for the  $\alpha$ -relaxation process. Matching the relaxation peaks obtained by a dielectric relaxation spectroscopy (DRS) with the IFA peaks, the cooperation length can be experimentally determined via

$$X_d(T) = v_o(T) \cdot \tau_\alpha(T) \quad (1.5)$$

where  $v_o(T)$  is the velocity corresponding to the  $\alpha$ -peak of the  $F_F(v)$  curves (IFA), and  $\tau_\alpha(T)$  is the  $\alpha$ -relaxation time from DRS. The cooperation lengths  $X_d(T)$  were determined with  $v_o(T)$  and equation (1.5) so that the resulting  $\alpha$ -relaxation times are consistent with those from dielectric spectroscopy, Fig. 1-5(Right). It is important to note that the determination of the length scale of cooperativity did not involve any of the many theoretical models, which makes this experimental methodology unique. The “uniqueness” goes even a step further, as our experimental work can actually be matched to theoretical models involving mode coupling theories and molecular dynamic simulations.<sup>8</sup>



**Fig. 1-5:** Left: IFA of polystyrene (MW: 06.5k) above  $T_g$ . Right: IFA/DRS provides a direct measure of the cooperation length  $X_d$  as function of the reduced temperature  $T_R$ .  $T_c = T_g + 15$  °C is the crossover temperature – an experimental observable at vanishing  $\Delta F_F$ . The slope  $\phi$  has been theoretically confirmed with a molecular dynamic (MD) simulation.<sup>8</sup>

This study illustrates our efforts in studying highly cooperative phenomena. We have recently devised a method to determine the entropic component from vertical  $\Delta F_F$  shifts utilizing the following relationship:<sup>1,4</sup>

$$E_a = RT_R [1 + \ln(k_B T_R / 2\pi\hbar f_R)] + T \Delta S \quad (1.6)$$

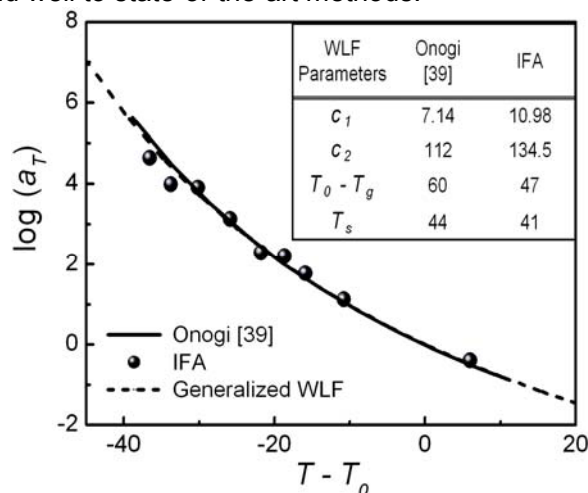
based on the apparent activation energy  $E_a$  of the underlying intrinsic friction dissipation process, the universal gas constant  $R$ , the relaxation peak frequency  $f_R$ , the activation entropy  $\Delta S$ , the relaxation temperature  $T$ , the Boltzmann constant  $k_B$ , and the Plank constant  $h$ . For a purely activated dissipation process, i.e., a process without cooperativity, the entropic term  $T\Delta S$  vanishes. An example for such a process is the  $\gamma$ -relaxation in *PS* (further discussed in 3.1), where the side-chain phenyls rotate independently from one another. The degree of cooperativity can be directly inferred from the vertical shift contribution  $\Delta F_F$  required to obtain a single master curve, as per Eq. 1.4, and as illustrated in Figure 1.6 for polystyrene above ( $\alpha$ -relaxation) and below ( $\beta$ -relaxation) the glass transition temperature. Our experiments show that the cooperative energy contribution  $T_R \Delta S$  to the

total apparent energy can be very significant (e.g., 80% and 20 %, respectively, for the two mentioned relaxations). Considering that in nanoscale confined systems cooperative effects can be expected to be appreciably enhanced due to finite size and interfacial constraints, it is imperative that studies of this kind are of great value not only from a fundamental but also engineering perspective.

To close this discussion, it shall be pointed out that IFA also provides insight into non-Arrhenius processes that are also of great importance for nano-constrained materials. This is here briefly illustrated with the rubbery state of polystyrene close to the glass transition temperature. The non-linear log-behavior of the shift factors  $\{a_T\}$  is typically treated with the Williams-Landel-Ferry (WLF) expression

$$\Delta E_a = 2.303 \cdot R \cdot c_1 \cdot c_2 \cdot \frac{T^2}{(c_2 + T - T_0)^2} \quad (1.7)$$

As shown in Figure 1-7, IFA results are well fitted by the WLF generalized model with fitting parameters that correspond well to state-of-the-art methods.<sup>10</sup>

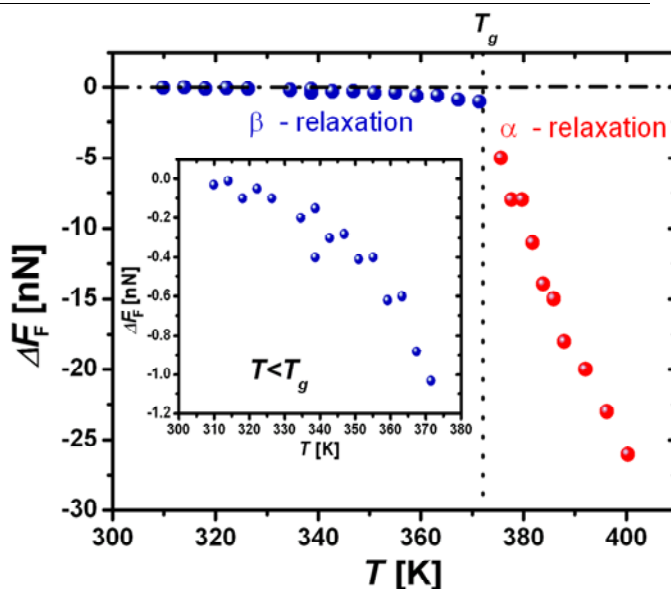


**Fig. 1-7:** The shift factor plotted against reduced temperature for rubbery polystyrene and Ferry's generalized WLF curve Inset: WLF parameters from literature and IFA.<sup>10</sup>

To close this aspect of our review, we found that IFA is well suited for analyzing the molecular mobility close to interfaces, and in thin films. As a local probe, IFA is also well suited for investigating laterally heterogeneous materials, such as phase separated systems (e.g., polymer blends). From a fundamental perspective, we recognized the importance of entropic constraints, in both value and preponderance in internal molecular and external nanoconstrained systems.

### 1.3 Self-Assembly Processes – Combined Enthalpic and Entropic Processes

In the prior discussion, I provided some insight into our group's research on analyzing inter- and intra-molecular mobilities of molecularly or interfacially constrained systems based on enthalpic



**Figure 1-6:** Vertical IFA friction shift  $\Delta F_F$  of polystyrene – a measure of the degree of cooperativity - reveals a significant entropic contribution to the apparent activation energy.<sup>7</sup>

activation barriers and entropic cooperative rearrangements. Of particular interest to us is the study of combined enthalpic and entropic processes, with focus on a wide variety of material systems (e.g., organic monolayer systems, ultrathin organic films, interfacially constrained polymers, and nanocomposites), and technological applications (e.g., organic membrane separation, tribology and adhesion, and energy production and storage) with focus on fundamental aspects (e.g., confined flow and relaxations, submolecular energy dissipation phenomena, local mechanical and electronic transport properties, and constrained phase behaviours).

Of particular interest to us are organic systems that are "imperfect" such as amorphous systems with local order. Although the current research efforts of many groups focus primarily on organic self-assembled crystalline systems, we believe that, by looking at living or organic matter, less perfect molecular arrangements have a higher potential due to increased resiliency. For instance, in organic materials, detrimental effects caused by defects are significantly less pronounced than in crystalline materials. Also, increased molecular mobility in organic amorphous systems, due to intrinsically lower potential barriers compared to crystalline systems, offer increased possibilities towards engineering applications. This aspect has been demonstrated, for instance, just recently in organic electronics, Figure 1-8, involving self-assembling NLO molecular glasses that yield, with over 300 pm/V, the highest ever reported EO activity

Dealing with organic or biological systems makes us particularly aware of the subtle but important differences. Weak interactions with bonding strengths small compared to  $kT$  are of immense importance as they dictate local mobilities. As such, one has to consider to what degree these processes are cooperative on a molecular scale. Highly cooperative phenomena, as those found in glass forming processes, as discussed above, exhibit unusually large apparent activation energies of up to 100 kcal/mol that are indicative of a high degree of complexity in the motion associated with relaxations. Weak interactions play an important role in self-assembled NLO molecular glasses, with structures of high cooperativity that lead to extraordinary increases in, for instance, EO activity – an aspect that is here a little further discussed.

The remarkable increase in EO activity beyond 300 pm/V (Fig. 1-8) is tribute to a new class of NLO materials of self-assembling molecular glasses (HDFD; Fig. 1-9) involving quadrupolar phenyl-perfluorophenyl ( $\text{Ph-Ph}^{\text{F}}$ ) interactions. Although, self-assemblies from  $\text{Ph-Ph}^{\text{F}}$  interactions have been reasonably well-known in material chemistry for many years, and employed for optoelectronic and liquid crystalline materials, its breakthrough as NLO materials has just recently occurred with HDFD.<sup>3</sup>

HDFD, the most basic representative of this new class of self-assembling NLO materials takes advantage of the strong affinity between phenyl (Ph) and perfluorophenyl ( $\text{Ph}^{\text{F}}$ ) moieties, which form face-to face  $\text{Ph-Ph}^{\text{F}}$  stacks of alternating hydrocarbon and perfluorinated moieties due to their complementary quadrupole moments. Both Ph and  $\text{Ph}^{\text{F}}$  moieties are integrated in second generation Fréchet-type dendrimers, which then are incorporated as peripheral dendrons on the  $\pi$ -bridge and the donor-end of the NLO chromophores to allow the chromophores to form an ordered network, as illustrated in Figure 1-9.

Figure 1-9 provides the chemical structure of HDFD, where HD and FD stand for the Ph-dendrimer and  $\text{Ph}^{\text{F}}$ -dendrimer, respectively. Based on the quadrupolar  $\text{Ph-Ph}^{\text{F}}$  interaction and the

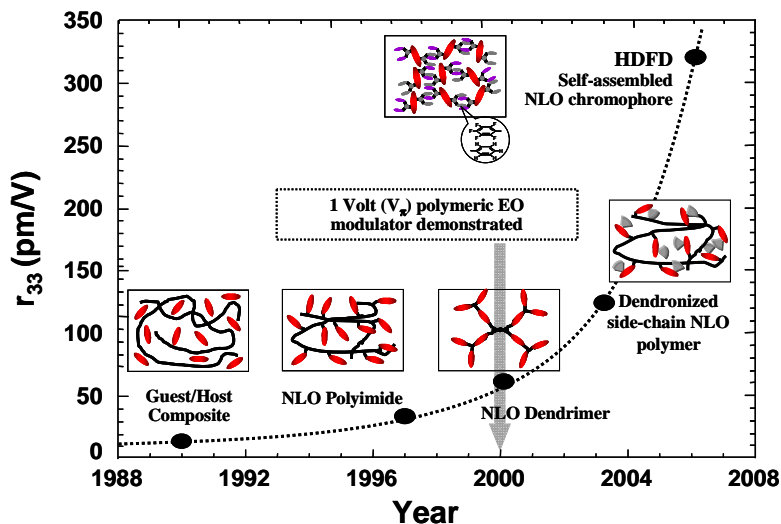
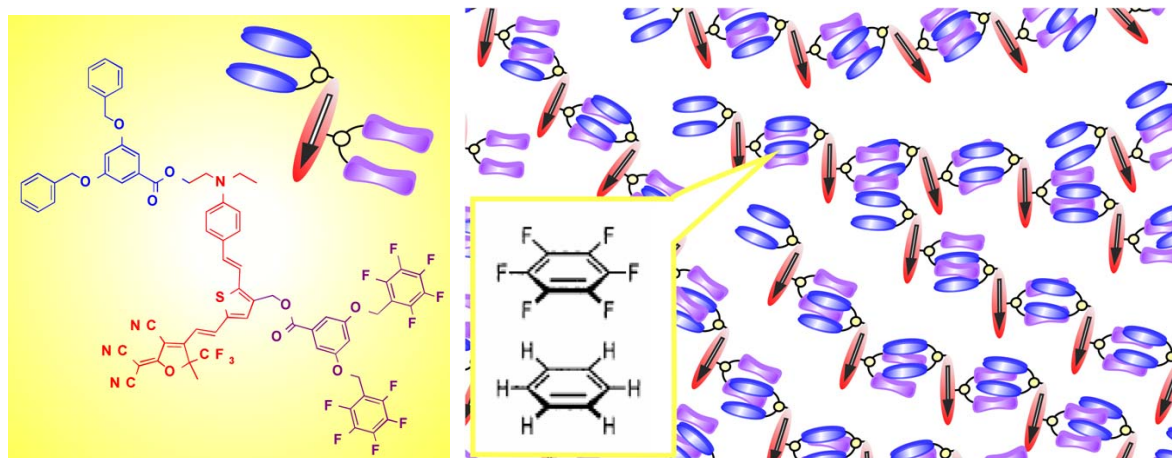


Figure 1-8: Progress in designing high EO activity with organic NLO material.<sup>3</sup>

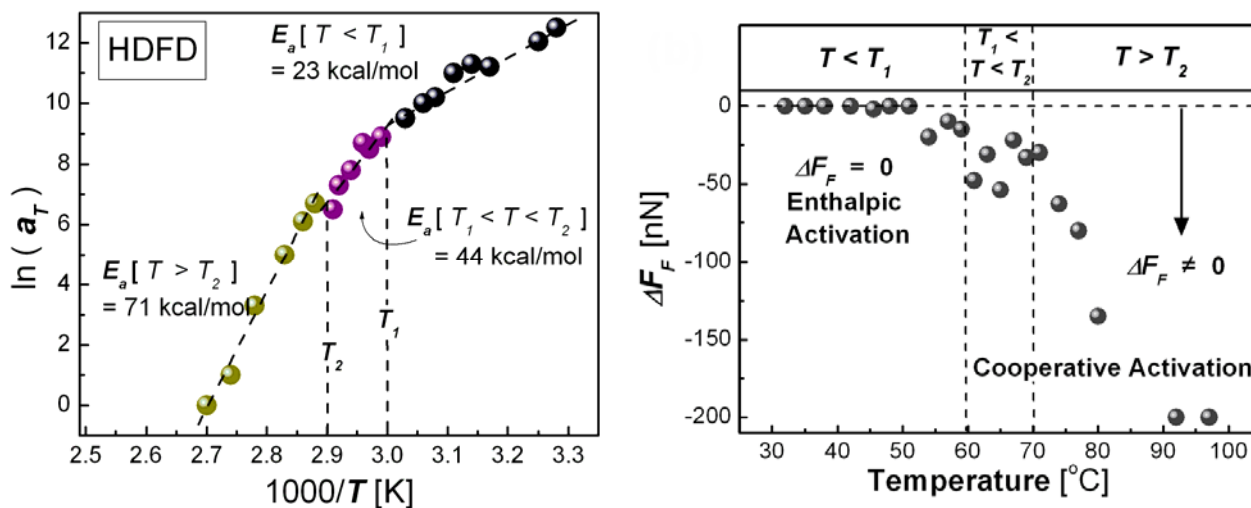


measured ultrahigh EO activities of over 300 pm/V, one is tempted to visualize the self-aggregation processes as highly ordered. However, X-ray analysis indicates that the structure is amorphous. Thus, the orientational stability in this system originates from a mesoscale structural alignment, i.e., a networking system that resembles a polymer chain, Figure 1-9. The obtained high acentric order of the chromophores after electric field poling suggests a network system that contrary to conventional polymers is highly temperature susceptible. Chains can be either broken, reconnected, or can form new connections under appropriate temperature conditions. This highly complex dynamic system exhibits inter-molecular relaxations with enthalpic activation barriers and cooperative phenomena.



**Fig. 1-9:** HDFD – a glass forming chromophore containing molecule with phenyl and pentafluorophenyl rings incorporated as peripheral dendrons on the  $\pi$ -bridge and the donor-end of the chromophores. “Polymerized” self-assembly networking model visualizing the dynamics in intact or broken chains.<sup>3</sup>

To investigate the subtle dynamics and energetics of the HDFD condensed phases, we utilized in principle two microscopic methodology, i.e., IFA and shear modulation force microscopy (SM-FM), which will be introduced below, wherein the scanning probe microscopy (SPM) cantilever is used as a thermomechanical (TM) sensor to detect critical temperature transition values.<sup>3</sup> Guided by SM-FM, IFA was conducted in three temperature regimes defined by the two transition temperatures  $T_1$  and  $T_2$ . IFA results are presented in Figure 1-10 in regards of both the energetics and cooperativity.


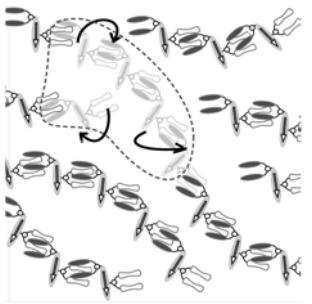



**Fig. 1-10:** (Left)  $a_T$ -shift-factor analyses in three temperature regimes of HDFD with apparent activation energies. (Right) Vertical shift,  $\Delta F_F$  as a function of temperature for HDFD. Entropic (cooperative) contribution is noticeable above  $T_1$ .<sup>3</sup>

Based on the information collected and knowledge of face-to-face phenyl/per-fluorophenyl interactions, the dynamics and cooperativity in the HDFD system can be interpreted as follows, Table 1-1.<sup>3</sup>

- Below  $T_1$ , the activation energy is associated with the dissociation of Ph-Ph<sup>F</sup> pairs that take place randomly in isolated events. It describes the uncorrelated molecular decoupling process of the glassy state of HDFD.
- In the intermediate temperature range ( $T_1 < T < T_2$ ), an increase in the density of dissociation sites leads to a cooperative phenomena, where molecules move in registry.
- Above but still close to  $T_2$ , the assembly breaks down but the molecular building blocks still possess high cooperativity, typical of a polymer melt close to the glass transition.

Table 1-1: Activation Energy and Cooperativity in HDFD.<sup>3</sup>

$T < T_1$	$T_1 < T < T_2$	$T_2 < T$
$E_a = 23 \text{ kcal/mol}$	$E_a = 44 \text{ kcal/mol}$	$E_a = 71 \text{ kcal/mol}$
$T\Delta S^* \approx 0$	$T\Delta S^* = 26-30 \text{ kcal/mol}$	$T\Delta S^* = 52-56 \text{ kcal/mol}$
		
Uncorrelated molecular decoupling in “glass state”	Cooperative decoupling	High cooperativity in “melt state”

Thus, while the dynamic enthalpy, i.e., the dissociation of Ph-Ph<sup>F</sup> pairs in HDFD, reflects a common relaxation mechanism for all three phases, the dynamic entropy exposes the phase variations in terms of cooperativity. With the introduced nanoscale thermomechanical methodology, it is now possible to study entropic phenomena of other molecular structures of self-assembled glass forming NLO system with, for instance, more or less flexible dendrons or larger Ph and Ph<sup>F</sup> moieties. This is research that is currently on-going in our laboratory.

Being able to deconvolute and quantify isolated processes from cooperative relaxation processes in condensed materials, our research efforts involving IFA and complementary techniques have shown to provide fundamental insight into the complexity of inter- and intramolecular constrained systems, which in turn provided the necessary input to design material cognitively. In the following section, we will shift from material specific constraints to our research on externally imposed constraints, such as interfacial and dimensional constraints.

## 2. Interfacial and Dimensional Constraints

While materials such as ceramics, metals, oxides, exhibit size limitations ('quantum well effects') only noticeable below 10 nm, it was found that in complex organic systems such as polymers, interfacial effects could be noticeable over distances of tens of nanometers.<sup>11</sup> Mean-field theories applied to interfacially constrained and size-limited polymer systems failed to describe the rather unexpected *mesoscale behavior* observed experimentally. The extension of the interfacial boundary far into the bulk was unexpected because many amorphous polymer systems were in the past theoretically treated as van der Waals liquids with an interaction length on the order of the radius of gyration, i.e., the effective molecular size. As in the vicinity of solid interfaces, the radius of gyration is compressed, it was reasonable to assume that interfacial effects are confined within this so-called *pinning regime* (~ 1 nm). Inside the pinning regime, it is commonly accepted that the material is structurally altered and exotic properties (for instance, quantum-well effects) are expected. Outside the pinning regime, complex materials, such as polymers, were expected to behave bulk-like.

Already our pioneering experiments, as early as 1994, have shown that such scaling theories fail. They do not explain observed unique mesoscale properties in thin films of thickness of tens of nanometers,<sup>12</sup> because they do not consider long-range coupling (see for instance Fig. 1-5), cooperative phenomena as discussed above, or material heterogeneities (discussed below). Also with mean-field approaches, it is generally assumed systems to be thermally equilibrated. We have tackled over the years a variety of aspects that involved interfacial constraints. From a fundamental perspective, two have been of particular interest to us, involving ultrathin polymer systems: (i) the glass transition, and (ii) low dimensional flow. Another aspect of interest has been interfacial constraints and boundary layer formations in simple liquids. The following subsections illuminate these three topics in greater detail and provide some insight into our research involvements.

### 2.1 Low Dimensional Flow – Wetting and Dewetting of Polymer Films

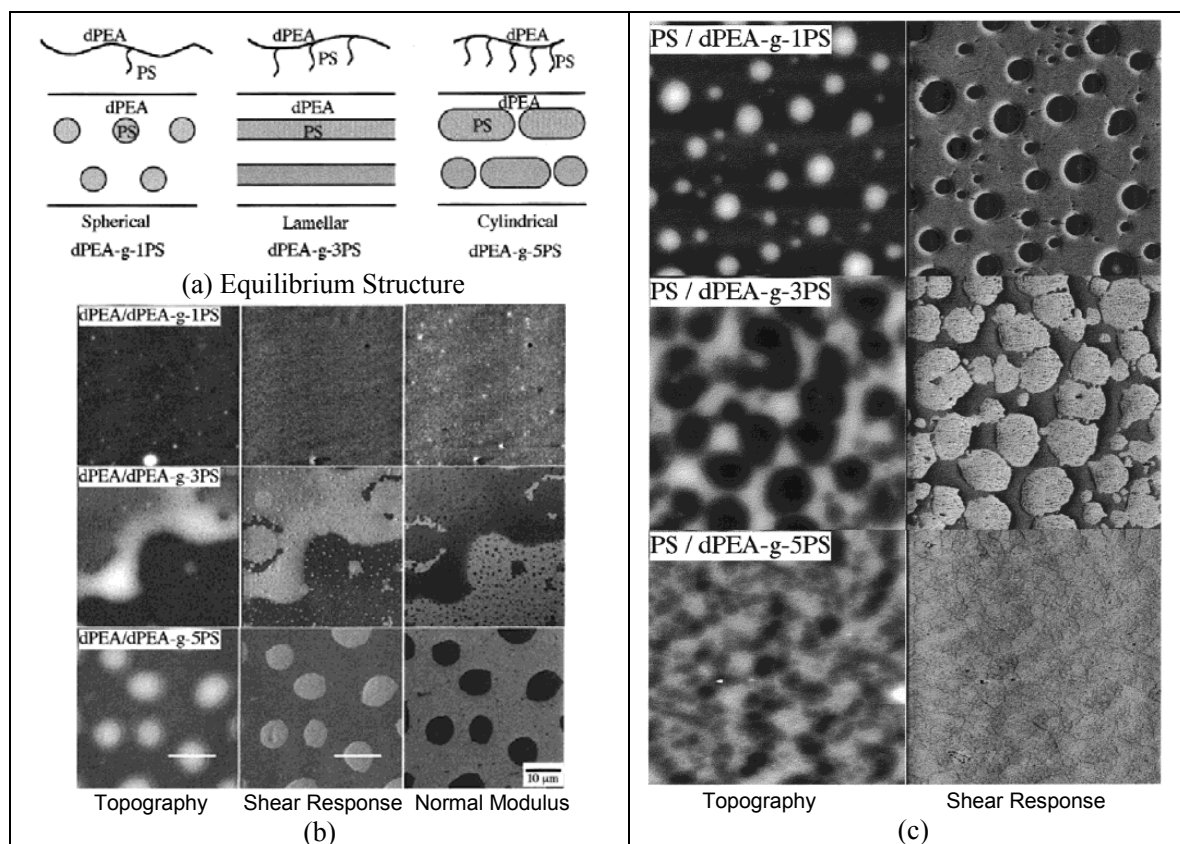
The process of wetting of surfaces by liquids within the mesoscale is very complex and of interest to us for many reasons. In ultrathin film lubrication, for instance, the wettability of the liquid is of enormous importance, as it affects the hydrodynamic slip length (an extrapolated length for non-zero velocities at the wall). Wetting phenomena are important for flow in micro or submicrometer conduits (e.g., membrane systems, and microfluidic flow systems). The spreading of "completely-wetting" polymer liquids on solid surfaces has revealed unexpected spatial and temporal features when examined at the molecular level. The spreading profile is typically characterized by the appearance of a precursor film of monomolecular thickness extending over macroscopic distances, and in many cases, a terracing (also on the order of molecular dimensions) of the fluid remaining in the reservoir (Heslot et al. (1989)). These spatial features have been shown to be consistent with a Poiseuille-like flow in which the disjoining pressure gradients with film thickness drive the spreading process (Karis et al. (1999)). The temporal evolution of the spreading profile in this film thickness regime is, however, found to universally scale as  $t^{1/2}$  even at short times (Heslot et al. (1989)). That the spreading dynamics are reflective of a diffusive transport mechanism, and not of a pressure driven "liquid" flow, suggests that interfacial confinement substantially alters the mobility of molecularly-thin polymer fluids.

Confined flow properties have been addressed in our research from monolayer lubrication,<sup>13</sup> to flow and wetting/dewetting characteristics in homopolymer, graft copolymers and polymer multiphase systems<sup>12,14,15</sup>. The wetting behavior of polymer thin films has received a great amount of attention, because of its importance in practical applications. The effect of an attractive solid interface on the polymer mobility was investigated and found to decrease diffusion significantly.<sup>14,15</sup> In a number of systems, we observed that the wettability of the surface is determined by the ability of the polymer melt to penetrate into the restricted polymer substrate such as a densely adsorbed polymer brush, a self-assembled surface of diblock copolymer with chemically dissimilar blocks, or a cross-linked surface.<sup>12,14,15</sup> Even if the melt and the substrate

are of identical chemical structure, entropy considerations limit the penetration of the melt chains into the substrate, leading to partial wetting. This phenomenon is referred to as “wetting autophobicity”. The physical origins of wetting autophobicity in polymeric systems can be attributed to limitations on the molecular configurations of the restricted polymer substrates.

### 2.1.1 Interfacial Excess Energy Induced Dewetting

In our research involving binary polymer systems, we addressed the role of the molecular architecture of the substrate on the wetting characteristic of polymer melts.<sup>12,14</sup> A series of model graft copolymers of constant molecular weight but different number of grafts was used to investigate the dewetting behavior with chemically identical homopolymer films.<sup>14</sup> The graft copolymers consisted of a deuterated poly(ethyl acrylate) (dPEA) backbone with one, three, or five pendant chains of monodisperse polystyrene (PS) attached randomly along its length (dPEA-g-xPS,  $x = 1, 3, 5$ ). The graft copolymers are ordered on silicon substrates with the lower-energy dPEA back-bone at the vacuum interface. The equilibrium structures are shown in Figure 2-1(a) determined by SIMS. The dewetting behavior of dPEA and PS homopolymer films on the ordered graft copolymer substrates was studied by scanning probe microscopy (SPM) techniques, Fig. 2-1(b) and (c), from which interfacial tensions were deduced.



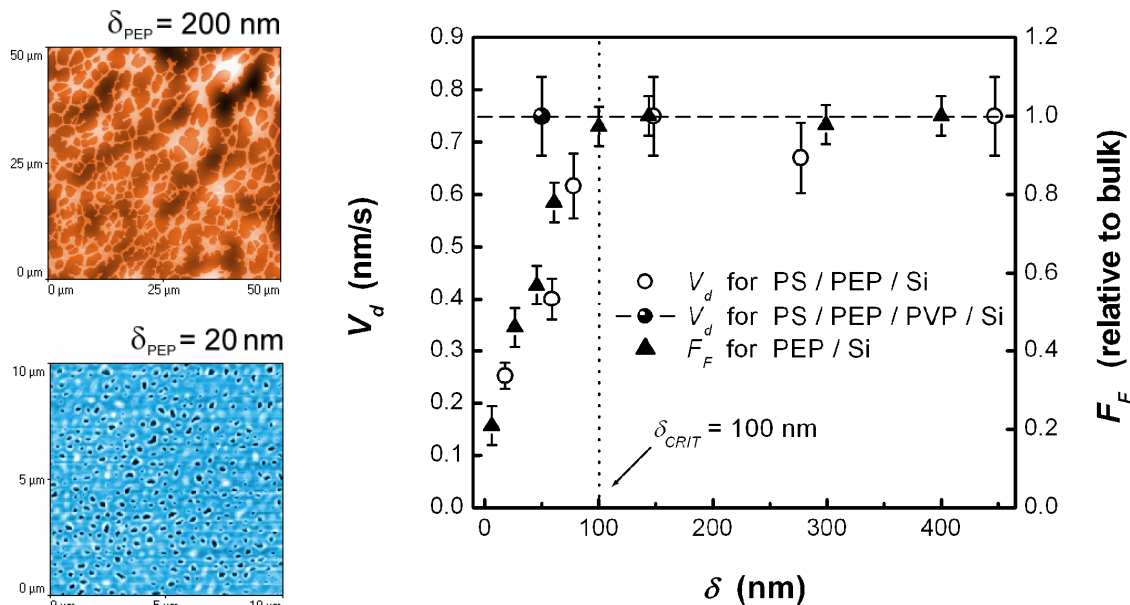
**Fig. 2-1:** (a) Equilibrium structure of dPEA-g-xPS ( $x = 1, 3, 5$ ). (b) SPM measurements of dPEA-g-3PS and dPEA-g-5PS graft copolymers covered by dPEA homopolymer. (c) SPM measurements of the dPEA-g-xPS graft copolymers covered by PS homopolymer. All systems have been annealed at 450 K for 24 h.<sup>14</sup>

The study revealed that for the lower viscosity homopolymer dPEA, the excess energy associated with the interface between dPEA-PS graft copolymer and the homopolymer can destabilize the film and induce dewetting. For the PS homopolymer, because the viscosity is greater than that of the substrate, the dewetting behavior on the dPEA-g-xPS substrate depends

on the substrate viscosity. The order of the dewetting velocity of the PS homopolymer on the graft copolymer was determined as: dPEA-g-1PS > dPEA-g-3PS > dPEA-g-5PS.

### 2.1.2 Finite Size Systems – Ultrathin Films

Subtle relative differences in the surface energies or viscous properties can significantly alter the flow behavior, as shown above, - as can interfacial modifications of the material phase. This last aspect becomes apparent in our dewetting studies on binary films with polystyrene (PS) covering thin films of polyethylene-co-propylene (PEP) that were spun onto silicon substrates (high interaction surface).<sup>12,16</sup> The dewetting kinetics in Figure 2-2 were determined from a time-series of SPM topography images, and reveal a critical PEP film thickness,  $\delta_{CRIT}$ , of  $\sim 100$  nm, below which the dewetting velocity ( $v_d$ ) decreases with decreasing film thickness, and above which,  $v_d$  remains constant. Independent friction force microscopy experiments (a method to determine material phase differences,<sup>5,9</sup> and probe local rheological properties) on PEP alone, Fig. 2-2, attribute the changes in the dewetting process on phase changes in the PEP matrix. While today such observations are not astonishing, they were quite surprising in 1995, when it was common practice to assume that after annealing a film thicker than a few nanometers behaves bulk-like. The dewetting kinetics and friction forces both suggest the presence of a rheologically modified PEP boundary layer adjacent to the silicon surface. For  $\delta_{PEP} < \delta_{CRIT}$ , the decreasing friction represents an increase in the PEP modulus. This translates to an increasing *glass-like* behavior, or loss of mobility, as the silicon interface is approached through the PEP phase. It is this loss of PEP mobility that is responsible for decreasing the dewetting velocity.



**Fig. 2-2:** (Left) PS dewetting of PEP. PS film thickness 10 nm. (Right) Dewetting velocity ( $v_d$ ) and friction ( $F_F$ ) measurements on PS/PEP systems reveal a 100 nm interfacial boundary layer.<sup>12,16</sup>

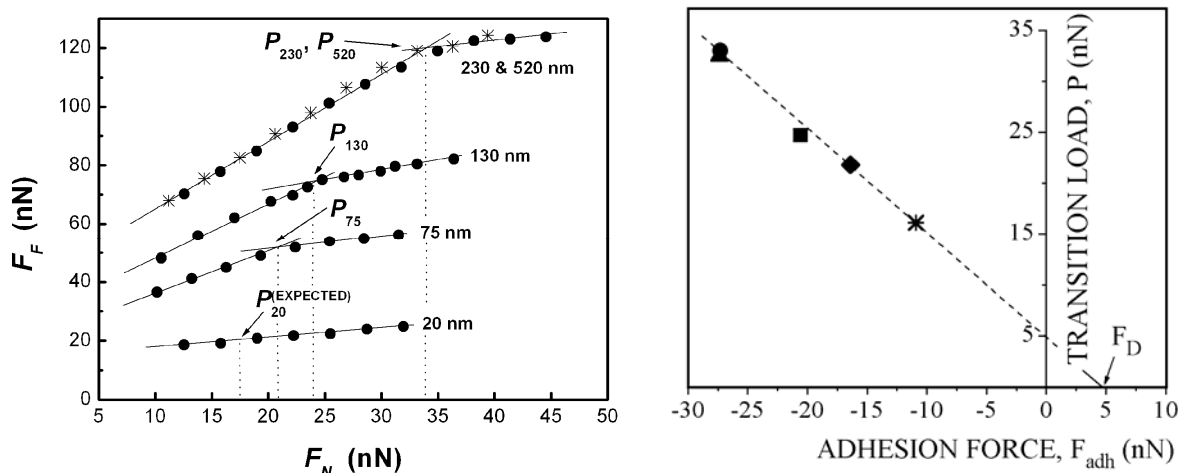
To identify the source of this rheological gradient, the PEP-silicon interactions were effectively masked by first spin casting a low interaction foundation layer of poly(vinyl pyridine) (PVP) on the silicon. The dewetting velocity of the PS/PEP/PVP layered film system, represented in Figure 2-2 by the filled circle and the dashed horizontal line, remained constant, even at PEP film thicknesses below  $\delta_{CRIT}$ . This finding unveils the high interfacial interactions between PEP and silicon as responsible for the apparent PEP vitrification inside the interfacial boundary.

Our nanoscopic friction ( $F_F$  vs.  $F_N$ ) experiments on silicon supported PEP films ( $R_G = 24$  nm) offered further insight to the source of these *far-field* molecular constraints beyond the pinning

regime.<sup>16</sup> A transition in the friction coefficient at a critical load ( $P$ ) is seen in Figure 2-3(Left). The higher friction coefficient below  $P$  portrays a dissipative behavior consistent with viscous plowing through an entangled PEP melt. We found that the transition load,  $P$ , fulfilled the criteria of a maximum load because no further strain occurred at higher load.<sup>16</sup> This allowed us to determine the load independent work of adhesion (per unit contact area), via

$$\gamma_D = \frac{1}{3\pi R} \lim_{P_{\max} \rightarrow 0} F_{adh}(P_{\max}) = \frac{F_D}{3\pi R}, \quad (2.1)$$

which yielded for  $\gamma_D$  a value of 53 dyn/cm. Plotting the transition load versus the instability adhesion force,  $F_{adh}$ , a Dupré adhesion force  $F_D$  of 5 nN could be interpolated at zero load, Fig. 2-3 (right). We found that these values were in excellent agreement with the literature.



**Fig. 2-3:** (Left) SPM friction experiments on PEP films reveal a critical load ( $P$ ) marking a transition from viscous shearing to chain sliding.  $F_N$  is the sum of the adhesion and applied load. (Right) Functional relationship between the adhesion force and the transition load,  $P$ , for 75-520 nm film thickness.  $F_D$  corresponds to the Dupré adhesion.<sup>16</sup>

Our study exposed a two phase low dimensional flow regime comprised of a *sublayer* and an *intermediate regime*. The mobility constraints are ascribed to the strain imposed during spin casting, paired with interfacial interactions in the sublayer and anisotropic diffusion in the intermediate regime. At loads exceeding  $P$ , the reduced friction coefficient represents a chain slipping phenomenon similar to a shear banding behavior. Thus, the critical load may be conceptualized as an effective activation barrier for disentanglement. The boundary layer thickness and information about to the conformational structure within the boundary are elucidated from the film thickness dependence of  $P$ :

- (i) The absence of the disentanglement transition ( $P$ ) in the 20 nm films and the ubiquitous low friction, chain slipping suggests that the PEP molecules are highly disentangled within a *sublayer* immediately adjacent to the substrate.
- (ii) In the 75-230 nm films, the disentanglement transition ( $P$ ) increases linearly with film thickness until the bulk  $P$  is reached. The sub-bulk  $P$  values indicate an *intermediate regime* of partial disentanglement, the extent of which diminishes with increasing film thickness until the bulk entanglement density is recovered. This far-field disentanglement ( $\sim 10 R_G$  from the substrate) is attributed to the strain imposed during spin casting. The preservation of the disentangled structure in the melt reflects an anisotropic diffusion process where partially disentangled chain ends diffuse into the more porous structure of sublayer.
- (iii) Finally, for films thicker than 230 nm, the polymer behaves like the bulk elastomer and loses any memory of the underlying silicon.

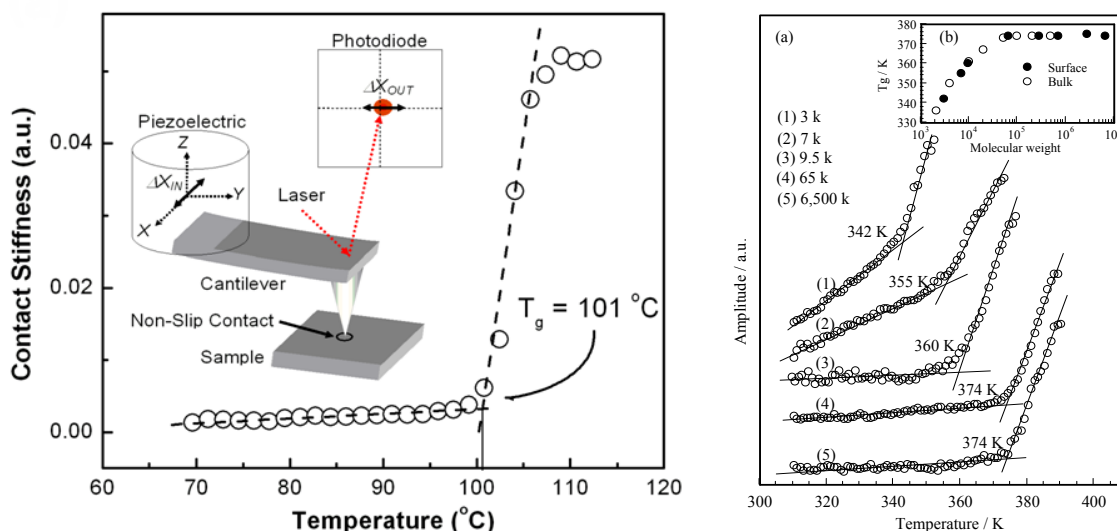
## 2.2 Glass Transition in Ultrathin Films

With the discovery of far-field interfacial effects in complex polymeric systems, we intensified our efforts in studying the impact of interfacial constraints in ultrathin films on one of the technologically most important but apparently nonspecific polymer property, the glass transition temperature  $T_g$ . In experiments, the glass transition is typically referred to as calorimetric glass transition, as the notion exists that  $T_g$  is not an actual material property (or material distinctive critical quantity), but to some degree a manifestation of the impatience of the experimentalist. This perception originated from the existing gap between theory and experiments, which until recently was lacking any correspondence between theoretical glass transition models, such as the mode-coupling theory and calorimetric glass transition experiments.<sup>10</sup>

Our first step was to devise a technique with which to determine the glass transition of thin film systems. Motivated by our success using SPM friction as a phase distinctive tool (see above), we developed a SPM approach based on lateral forces, referred to as shear modulation force microscopy (SM-FM).<sup>17</sup> SM-FM has turned out to be an excellent tool to determine any sort of transitions and relaxations at polymer surfaces. It is a non-scanning method.

*Briefly:* A nanometer sharp scanning force microscopy (SFM) cantilever tip is brought into contact with the sample surface as illustrated in Figure 2-4(*left*). While a constant load is applied, the probing tip is laterally modulated with a "no-slip" nanometer amplitude,  $\Delta X_{IN}$ . The modulation response,  $\Delta X_{OUT}$ , is analyzed after each temperature step using a two-channel lock-in amplifier, comparing the response signal to the input signal. The modulation response is a measure of the contact stiffness. Thermally activated transitions in the material, such as the glass transition,  $T_g$ , are determined from the "kink" in the response curve, as shown in the same graph, and in Figure 2-4(*right*), as function of the molecular weight of the polymer<sup>18</sup>. With a computer acquisition setup great care is taken to stay close to steady state after each temperature step ( $\sim 0.1$  to  $0.5$  °C).

Conceptually, SM-FM is a nanoscopic analogue to dynamic mechanical analysis (DMA), however, because of its small probing volume, SM-FM is probing very close to the material's unperturbed state. This last statement is one of the most important findings of our research involving  $T_g$ . In conjunction with the IFA analysis (c.f. sec. 1.2), we established  $T_g$  to be a truly distinctive critical thermal property of the material. As discussed above, Fig. 1-5(*Right*), it turned out that  $T_g$  is well described by theoretical transition temperatures, such as the mode coupling temperature.



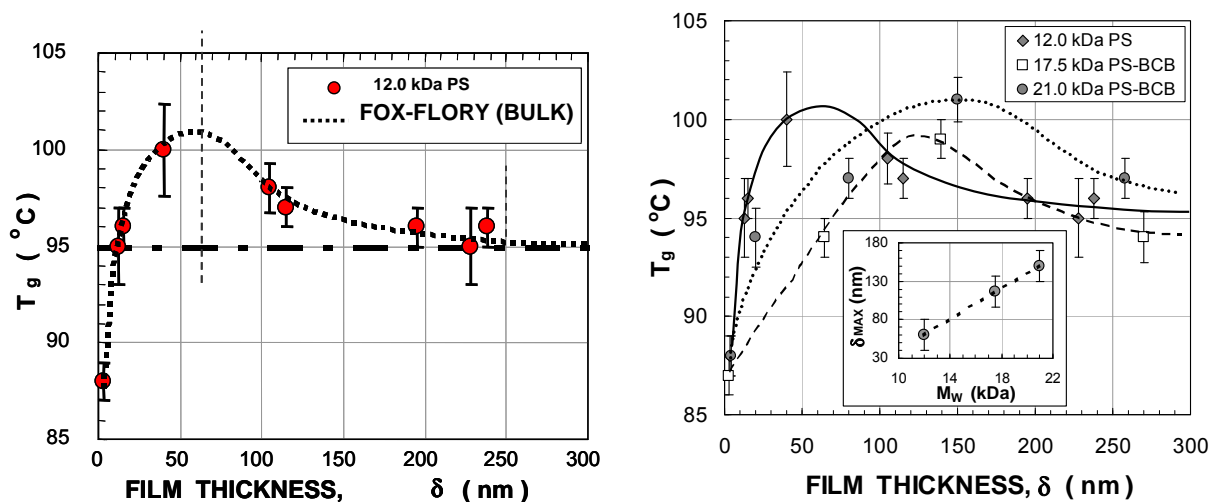
**Fig. 2-4:** (*Left*) SM-FM working principle. Illustrated on atactic monodisperse polystyrene ( $M_w$  90k).<sup>17</sup> (*Right*). (a) SM-FM molecular weight series of polystyrene. (b) SM-FM  $T_g$  values correspond well to bulk values determined by differential scanning calorimetry.<sup>18</sup>

With the successful development of an analysis tool sensitive to near-surface thermal transitions in thin films, we were ready to study the effect of substrate confinement on the glass transition. Although, we recognized the importance of impurities and monodispersity (low molecular weight polymer have a high preponderance at the free surface), it turned out that SM-FM experiments are by far less delicate to perform as originally assumed. We recognized that several factors are intricately responsible for the departure of  $T_g$  in ultrathin films from the bulk value;<sup>7</sup> (i) the proximity of a free surface, (ii) substrate interactions, and (iii) process-induced anisotropy. Here, I briefly summarize our findings on the effects of spin casting on the interfacial  $T_g$  profile of amorphous polymer films, along with the use of chemical crosslinking as a mobility control.

SM-FM  $T_g$  measurements on PS films ( $M_w = 12k$ ) are presented in Figure 2-5 (Left). For film thicknesses,  $\delta > \sim 100$  nm, the  $T_g$  values correspond to the bulk  $T_g$  of  $95^\circ\text{C}$ .<sup>7</sup> As in the friction study presented above, a two phase boundary layer is encountered within  $\sim 100$  nm of the substrate: (a)  $T_g$  values are depressed relative to the bulk in a *sublayer* with a thickness on the order of  $R_G$ , i.e. one order of magnitude beyond the persistence length; and (b)  $T_g$  values exceed the those of the bulk in the *intermediate regime*. Thus, the origin for the non-monotonic  $T_g(\delta)$  relationship is due to shear induced structuring imposed by the film processing condition (spin coating) followed by interdiffusion.<sup>7</sup>

While the dominant change in  $T_g$ , i.e., the decrease is widely acknowledged for ultrathin polymer films, the less pronounced increase has rarely been observed by other groups, due to instrumental sensitivity limitations. We, on the other hand, observed a non-monotonic  $T_g(\delta)$  profile for various spin coated polymer thin films. I will show later (subsection 4.3), the significance of this profile for engineering applications. In the next two paragraphs, our research in this field, involving  $T_g(\delta)$  profile modification by imposing additional constraints will be illustrated.

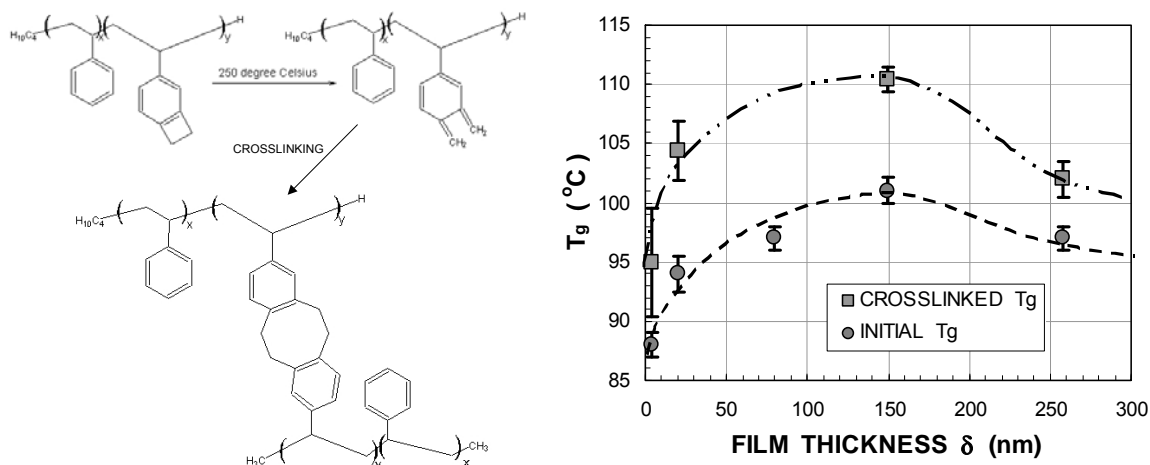
One way of altering interfacial constraints is by changing the molecular weight ( $M_w$ ). Increased  $M_w$  in spin cast films had the effect of shifting the glass transition maximum in the  $T_g(\delta)$  profiles further away from the substrate, as shown in Fig. 2-5(Right).<sup>7</sup> Consequently, the bulk  $T_g$  is recovered for thicker films. The influence of  $M_w$  on the internal structure of the boundary layer appears more pronounced on the sublayer thickness than on the far-field boundary of the intermediate regime. This suggests that the overall boundary thickness depends more strongly on the spin casting shear stresses than on molecular dimensions.



**Figure 2-5:** (Left) (top) Film thickness,  $\delta$ , dependence of  $T_g$  for PS films ( $M_w = 12k$ ) compared to the bulk  $T_g$  from Fox-Flory theory. (Right)  $T_g(\delta)$  profiles as function of the molecular weight. *Inset:* Linear relationship between the maximum thickness  $\delta_{\text{max}}$  (defined by the maximum  $T_g$  value) in each profile with the corresponding molecular weight  $M_w$ .<sup>7</sup>



Furthermore, we imposed internal constraints by crosslinking.<sup>7</sup> Polystyrene-benzocyclobutane (PS-BCB) films exhibited qualitative similar and vertically shifted  $T_g(\delta)$  profiles before and after crosslinking, as illustrated in Fig. 2-6. Thereby, crosslinking yielded an overall  $T_g$  increase ( $7\pm 3$  °C in this case); however, in contrast to the  $M_W$  dependence discussed above, no horizontal spatial shifts occurred.



**Fig. 2-6:** (Left) PS-BCB crosslinking mechanism. (Right)  $T_g(\delta)$  profile for PS-BCB thin films (21kDa PS-4.8 mol% BCB) before and after crosslinking (crosslinked at 250°C under  $N_2$  for 1 hr).<sup>7</sup>

Thus, our research has not only provided us with fundamental insight into constraint-modified transition properties on the sub-100 nanometer scale, but also with control parameters that allow us to adjust transition profiles accordingly to desired material behavior, an aspect, that is discussed in greater detail in subsection 4.3. We also learned from the two imposed constraints that the impact of mobility constraints on the structure within the boundary layer depends on the sequence of the film preparation process.<sup>7</sup> Something that is crucially important and often neglected in theoretical models.

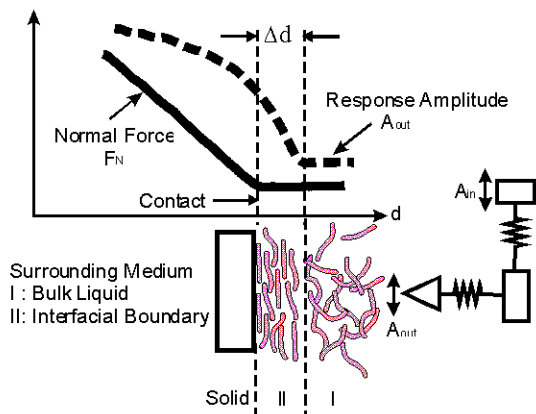
### 2.3 Interfacial Dimensional Constraints - Entropic Cooling in Simple Liquids

At this point of section 2, we switch from condensed solid polymeric and interactive systems to “simple”, low interactive condensed fluid systems. Our interest is in determining how dimensional constraints at 2D interfaces are impacting the phase behaviour of liquids in the boundary regime. This aspect of our research is illustrated with our nanoscopic study of two hydrocarbon fluids of significant different molecular shape.

We were curious about the effect of an ultra-smooth planar surface on self-induced local “structuring”, or more to the point, *entropic cooling*, involving the two hydrocarbon liquids n-hexadecane and octamethylcyclotetrasiloxane (OMCTS). These two material systems sparked our interest as they had been repeatedly studied by surface forces apparatus (SFA), revealing a layering of the liquid molecules under compression involving two smooth interfaces. Curiously, some molecular dynamic simulations claimed to confirm this behavior with only one interface. Our experiment<sup>2</sup> involved ultrasharp probing SFM tips (with  $\sim 1 - 5$  nm radius at the tip apex), which were sinusoidally shear-modulated and lowered within the liquids to the surface with nm/s speeds. Such a shear modulation analysis, as illustrated in Figure 2-7(Top), is very close to equilibrium probing. It combines normal tip-sample interaction force measurements with shear amplitude response information. Differences in the onset of change in the two mentioned signals during an approach provide a direct measure of the boundary layer thickness.

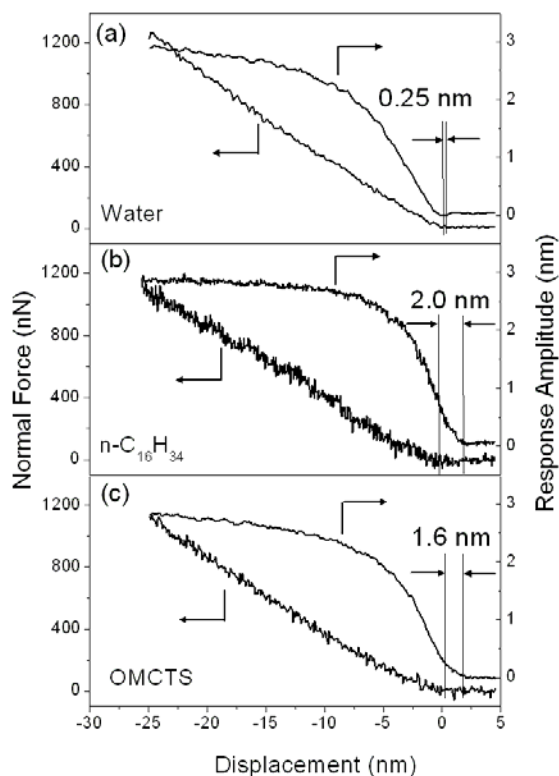
Figure 2-7(Right) presents the results of the two liquid hydrocarbon liquids, and water that served as discriminator for our instrumental accuracy. The experiment revealed only for the linear n-hexadecane an entropically cooled, interfacially layered fluid boundary of 2 nm thickness, while OMCTS, consisting of spherically shaped molecules, exhibited only an interfacial ‘monolayer’.

Thus, while our results regarding n-hexadecane compared well with SFA experiments (i.e., half of the maximum layer thickness involving two surfaces), our OMCTS results were significantly smaller. The major difference between SFA and our SFM experiment is the lateral probing or confining dimension. While during SFM experiment the molecules can easily escape from underneath the tip, it is far more difficult for them to escape from between the micron-sized confining surface planes of SFA. In SFA liquid molecules are temporarily trapped that gives rise to density fluctuations, and thus, oscillatory solvation forces. In our SFM experiment, on the other hand, trapping effects are negligible.



**Fig. 2-7(Top):** Illustration of the shear modulation SFM approach methodology that provides the boundary layer thickness  $\Delta d$  from the difference in the onset of change of the shear modulation response curve and contact force curve.

**Fig. 2-7(Right):** Shear modulated force displacement measurements towards silicon oxide surfaces with an approach velocity of 5 nm/s at 21 °C in (a) water, (b) n-hexadecane and (c) OMCTS. The measurements were obtained with stiff rectangular SFM cantilevers (37-55 N/m), to avoid any snap-in instabilities, and with a shear amplitude of 3 nm (RMS) at 5kHz modulation.<sup>2</sup>



Consequently, we concluded that n-hexadecane molecules due to their highly anisotropic shape experience an interfacial alignment over an interfacial boundary regime of 2 nm that is affecting the SFM shear response. OMCTS on the other hand because of its more isotropic spherical shape is only affected in the molecular pinning regime, i.e., only when the molecules are in direct contact with the solid surface. It is interesting to note that these ultrathin boundary layers have a significant impact on the lubricating shear properties (c.f. sec. 3.2). From a viscometric perspective one would assume hexadecane to be a less effective lubricant as its viscosity exceeds the one of OMCTS in average by about 30 %. Experiments, however, show hexadecane to be the better (the lower friction, and friction coefficient) lubricant of the two.<sup>2</sup> Although astonishing from a viscometric perspective, it is predictable from the here gained molecular insight into the boundary layer formation of a dimensionally constraint system. We will continue this discussion in the next section that deals with fundamentals in tribology.

### 3. Tribology Fundamentals

Our research on confined materials has been strongly influenced by our work in nanotribology. Tribology, although one of the oldest engineering discipline, it is one of the least developed classical sciences to date. The reason is that Tribology like Nanoscience is neither truly a single discipline nor well represented by steady state processes. It involves all the complexities of nano-constrained materials that are experienced over a wide range of scales during a shear occurrence.

Originally, idealized solid lubricant films, such as Langmuir Blodgett (LB) films, served as model systems. Thus, first insight into nanoscopic friction processes were revealed on phase separated monolayer systems, as illustrated in Fig. 3-1.<sup>5</sup> For that reason, we pioneered a SPM based tool that is known today as friction force microscopy (FFM). Our early studies involved various aspects in friction, lubrication, wear and adhesion.<sup>5,9,19-25</sup> The two most influential were the nanoscopic distinction and visualization of material phases,<sup>5</sup> and the first measurement of a truly molecular stick-slip process that was thought, at that time, to manifest the origin of “wearless” friction,<sup>23</sup> Fig. 3-2. The nanoscopic distinction of material phases led later to an entire subdiscipline in nanoscience probing, referred to as “chemical force microscopy”. The wearless molecular scale friction study that confirmed the old Prandtl-Tomlinson molecular stick-slip model from the 1930s, led to various theoretical developments that currently form the state-of-the-art understanding of molecular scale friction, an aspect that is critically assessed and redirected towards intrinsic material properties in our current research (see following subsection).



Fig. 3-1: Friction on phase separated monolayer.<sup>5</sup>

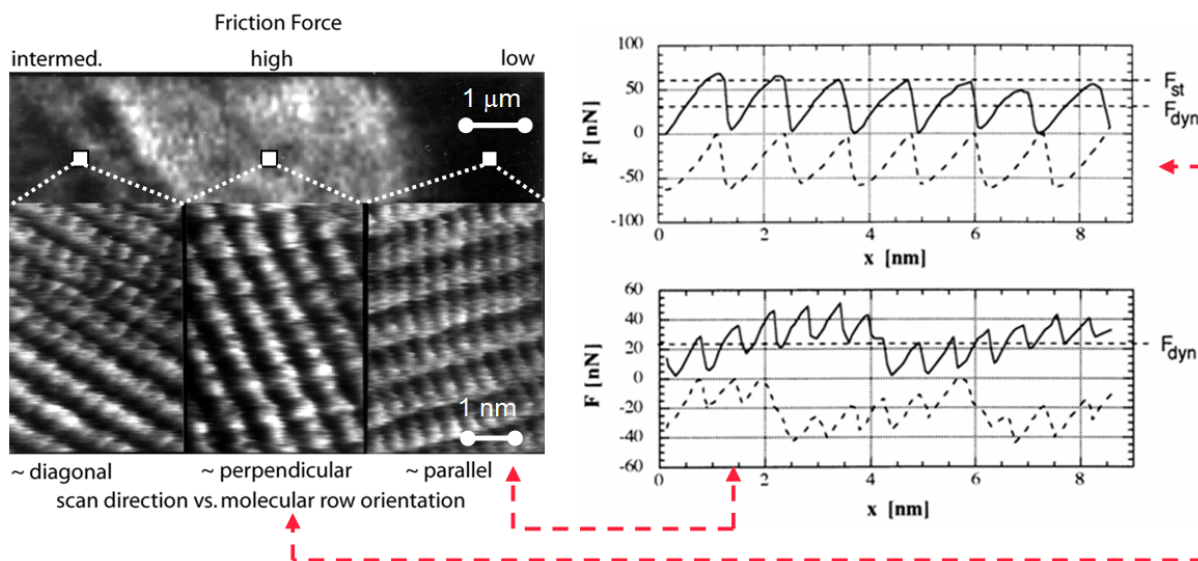


Fig. 3-2: FFM molecular stick-slip study of a bilayer lipid system (5-(4'-N,N-dihexadecylamino)benzylidene barbituric acid). (Left) Macroscopic friction force contrasts (top) are related to the relative alignment of the molecular structure (bottom) in respect to the left-to-right scanning direction. The orientation of the anisotropic row-like structure dictates the friction force values (contrast). (Right) Friction hysteresis curves for “perpendicular (top) and more or less “parallel” sliding directions (bottom).  $F_{st}$ , static friction, is assigned to the maximum force occurrence. The average stick-slip value  $F_{dyn}$  corresponds to the dynamic friction value determined on large scale micrometer scans.<sup>23</sup>

With our increasing involvement in polymers and fluids, our attention in tribology related aspects turned to confinement effect in thin solid polymer films<sup>1,3,4,7,8,10,12,16,18,26-32</sup> and interfacially

confined liquids<sup>2,13,33,34</sup>. In particular one aspect defined our group's research in tribology over the recent years. It is the true material origin for friction dissipation in condensed matter.

In general, tribology research, and I include here most of the experimental and theoretical research that has been conducted, has merely focused on a descriptive formalism of the tribological process. This claim can easily be justified if one tries to cognitively synthesize a lubricant molecule based on fundamental research results. It is unattainable, as the information available concerning the friction dissipation process is not linked to the molecules themselves, but only to generic models or processes. With the discussion above (Figure 3-2), I provided an example of a generic dissipation process – the stick-slip behavior – as illustrated in Fig. 3-3 in its simplest form. Note, there is no information provided in how the material itself is actually involved in dissipating the energy.

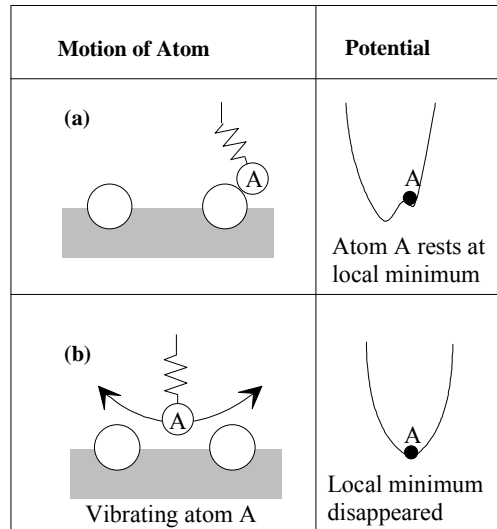
Current molecular models in tribology that go beyond the simplistic Prandtl-Tomlinson Model (Fig. 3-3) are still only employing Langevin equations and Fokker-Planck statistical kernels, and thus, focus on generic periodic potentials that are thermally and mechanically inert. Energy dissipation is described primarily only by viscous dampeners and heat generation, without gaining insight into the molecular dissipation process involving material intrinsic molecular or submolecular modes of relaxation. Thus, effective molecular models necessary to design the next generation of low dissipation tribological interfaces from the bottom-up are missing.

The opportunity to observe and consequently engineer the energy transfer from the one-dimensional frictional sliding motion into the multi-dimensional phase state close to the material's equilibrium condition embodies the main motivation of our current research effort. With the experience and insight our group has gained over the years in nanorheology of confined organic material systems, we started to pursue a path that treats tribological systems in terms of activated processes, involving reaction kinetics and rheology, with activation barriers that are specific to the material involved. This concept and our involvements are described for organic solids and liquids in the following sections.

### 3.1 Tribo-Dissipation Involving Intramolecular Constraints

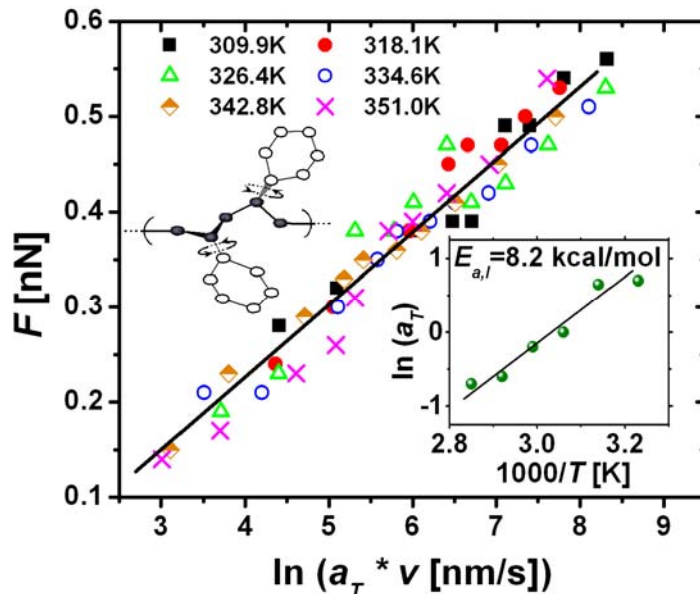
An effective material design concept in tribology involves material synthesis that is tailored from the bottom-up (submolecular scale) towards the desired properties and functionalities. This involves insight into the material behavior under shear stress sliding conditions.

Since Bowden and Tabor's adhesive-concept of energy dissipation, friction has been dealt with from a surface science perspective involving a variety of process descriptions (e.g., wear phenomena and stick-slip processes, and tribochemistry), while material specific relaxation properties moved more into the background. Interestingly, it was Tabor who was one of the pioneers besides Grosch, in considering molecular relaxation properties responsible for energy dissipation in polymer rubbers.<sup>35</sup> This *triborheological description* of frictional dissipation faced significant resistance by *surface bonding-debonding theories* pioneered by Schallamach and others.<sup>35</sup> One of the shortcomings of triborheological description in 1950-60 was the inability to specifically excite material intrinsic molecular modes of relaxations during phenomenological sliding motions. Large and rough contact regimes imposed convoluted signals containing aspects of sliding and cutting among others, and trapped the slow relaxing polymer phases in non-equilibrium states. Also, the material within the interfacial sliding region was rather poorly defined.



**Fig. 3-3:** Generic Friction Model by Prandtl and Tomlinson

In contrast to the macro-techniques used by Tabor and others, the ability to probe a material closer to its equilibrium has been a hallmark of scanning force microscopy (SFM), as already addressed above. In one of our more recent SFM friction studies on atactic and monodisperse polystyrene (PS),<sup>28</sup> involving IFA,<sup>\*</sup> we showed that the sliding motion can couple to very specific submolecular rotational motions within the material, as illustrated in Fig. 3-4 for the phenyl rotation at the PS backbone.



**Fig. 3-4:** Intrinsic friction analysis (IFA) of polystyrene below the glass transition and at low probing pressure ( $L < L^*$ ) reveals an activation barrier  $E_{a,I}$  of 8.2 kcal/mol (phenyl rotation).<sup>1,28</sup>

The coupling of the sliding motion with actuators of the material's relaxation states gave rise to a barrier-hopping fluctuation not unlike the one observed for highly ordered surfaces. Friction-rate isotherms obtained with a SFM tip on glassy polystyrene could also be collapsed to a master curve according to a tribological *ramped* creep model by Dudko and Sang,<sup>28</sup> which considers a single asperity sliding over a corrugated surface potential that is biased due to the motion of the driven tip.

Ramped creep scaling is consistent with the solution of the Langevin equation for a perfect cantilever oscillator, i.e.,

$$M\ddot{x} + M\beta\dot{x} + \frac{\partial E(x,t)}{\partial x} = \xi(t), \quad (3.1)$$

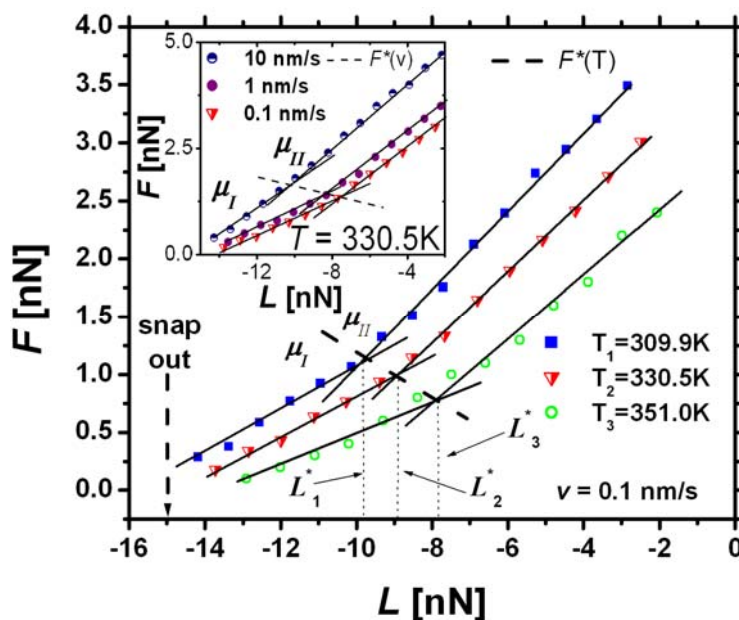
with the total potential energy  $E$ , the position of the tip on the surface  $x$ , the mass of tip  $M$ , the linear dampening factor  $\beta$ , and the thermal noise in the form of the random force  $\xi(t)$ , where  $\langle \xi(t)\xi(t') \rangle \propto k_B T \delta(t-t')$ . Eq. 3.1 is based on a sinusoidal surface potential continuously overcome during the course of frictional sliding. The challenge is the experimental determination of the energy barrier  $E$ , which provides intrinsic information about the material involved. For example, we determined by IFA an energy potential under low pressure conditions of  $8.2 \pm 1$  kcal/mol for glassy polystyrene that could be assigned to the hindered rotation of the phenyl ring side chains about their bond with the backbone.<sup>1,28</sup> In this study, friction could be directly linked to the "molecular deformation properties" (side-chain relaxations) of the underlying molecular building blocks.

Thus, nanoscale friction-rate isotherms, if treated according to the WLF superposition principle (c.f. sec. 1.2), provide submolecular scale information about the relaxation modes available. This information can be (i) used to access the dissipative process on a submolecular

\* For details about IFA see section 1.

scale, and/or (ii) fed back into the manufacturing design process to either cognitively affect the molecular synthesis or material processing.

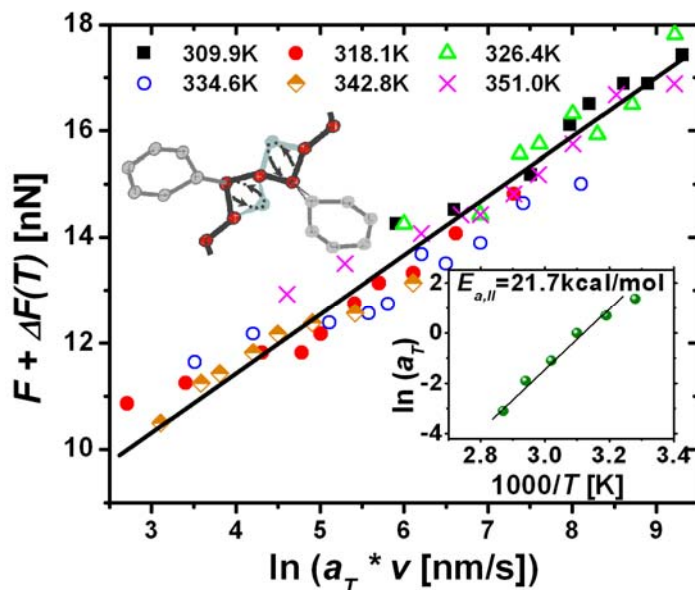
To put the PS study above (Fig. 3-4) in perspective to a classical tribological analysis, I present with Figure 3-5 phenomenological friction-load curves,  $F(L)$ , over a range of temperatures ( $T < T_g$ ) and scan velocities. The first thing, we notice, is the wealth of information in this plot. Below  $T_g$ , each of the  $F(L)$  isotherms reveals a kink at a critical normal load,  $L^*(T)$ , separating each curve into two linear friction-load branches with friction coefficients  $\mu_I(T)$  and  $\mu_{II}(T)$ . This phenomenon is apparent with variations in both temperature and scan rate (Fig. 3-5 inset). It is important to note that the absolute values of  $L^*$  are dependent on the applied pressure, i.e., involve besides the applied load also the cantilever tip size. The friction force at the critical load,  $F^*(L^*(T,v))$ , reveals a linear and logarithmic dependence with temperature and velocity, respectively, as expected from thermodynamic friction models



**Fig. 3-5:** Isothermal friction-load plots for atactic PS subdivided at critical loads  $L_k^*$  ( $k = 1, 2, 3$ ) into two friction regimes with friction coefficients  $\mu_I$  and  $\mu_{II}$ . The dashed line tracks critical loads; i.e.,  $F^*(T) = F_{o,T} - \alpha T$ , with  $\alpha = 8.5$  pN/K and  $F_{o,T} = 3.7$  nN. (Inset) Friction-load plots at constant temperature with  $F^*(v) = F_{o,v} + \beta \ln v$  (dashed line), where  $\beta = 0.076$  nN and  $F_{o,v} = 1.5$  nN.<sup>1</sup>

To elucidate the molecular origin for the two friction regimes, we individually employed IFA to the  $\mu$ -specific branches of the isotherms. The study revealed two apparent activation energies  $E_{a,I} = 8.2 \pm 1$  kcal/mol ( $\sim 0.30$  eV) and  $E_{a,II} = 21.7 \pm 2$  kcal/mol ( $\sim 0.94$  eV) below and above the critical load  $L^*(T)$ , respectively, as shown in Fig. 3-4 and Fig. 3-6. Hence, the cause for the discontinuity in the friction-load curve in Figure 3-5 was found to originate from a transition between two loading (more precisely – pressure) dependent material specific relaxation modes.<sup>1</sup> The known preferential orientation of the phenyl pendant groups towards the free-surface normal explains why these two modes are separated by a well-defined transition load. As illustrated in Figure 3-7, at low load, the phenyls act like surface ball bearings lowering the frictional dissipation significantly. At specific, temperature and velocity dependent critical loads, the phenyls are displaced and the ‘subsurface’ or bulk relaxation mode, i.e., the translational crankshaft motion, takes over as the primary dissipation mechanism. This leads to a significant increase in energy dissipation that is caused to a large extent by molecular cooperativity. The transition forces  $F^*(v)$  and  $F^*(T)$  (see Fig. 3-5) can also be analyzed in a manner analogous to the IFA energy analysis presented above in accordance with the superposition principle. We deduced from  $F^*(v)|_{T=}$

isotherms an activation energy of  $9.9 \pm 1$  kcal/mol, which reflects the phenyl loading capacity at the free surface.



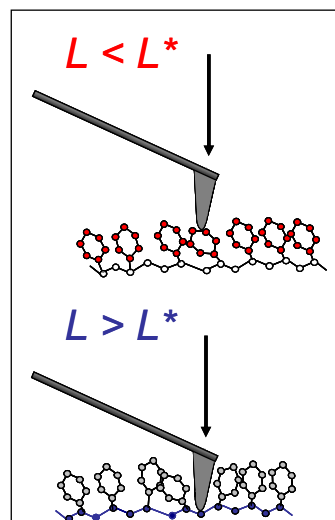
**Fig. 3-6:** Intrinsic friction analysis (IFA) of polystyrene below the glass transition and at high probing pressure ( $L > L^*$ ) reveals an activation barrier  $E_{a,I}$  of 21.7 kcal/mol (isolated polymer backbone motion).<sup>1</sup>

As pointed already out in section 1, the apparent activation barrier contains an enthalpic and entropic component. While the enthalpic component provides the activation barrier for submolecular rotations and segmental translations, the entropic component provides a measure of the cooperative motion involved, also illustrated in Fig. 1-5. The entropic component  $T_R \Delta S$  can be a significant contributor to the total frictional energy dissipation.<sup>†</sup> In the case of the translational crankshaft motion of PS, it raises the energy that is dissipated by 20%.<sup>1</sup> Above the glass transition this number even quadruples.<sup>1</sup> It is important to note that such contributions are omitted by enthalpic friction models based on Eq. 3-1 with  $\langle \xi(t) \xi(t') \rangle \propto k_B T \delta(t-t')$  that consider only uncoordinated energy dissipation processes. Based on Eq. 1.6 and a thermal activation model discussed in more detail in the next subsection, we derived an analytical relationship between the experimental IFA observable for cooperativity  $\Delta F$  (vertical shift - see section 1, Figs 1-2 and 1-6) and  $T_R \Delta S$ , which can be approximated by its significant components, as<sup>1</sup>

$$\Delta F \approx -\frac{T_R \Delta S}{\phi} A. \quad (3.2)$$

Here,  $A$  represents the area of contact and  $\phi$  the stress activation volume, a measure of the spatial effect of cooperativity.

This study illustrates our efforts in attaining a truly fundamental understanding of friction dissipation processes of mechanically compliant material. Further progress in this area will provide us with the means to design molecules (possibly assisted by computer simulation) with submolecular scale prescribed frictional energy dissipation characteristics.



**Fig. 3-7:** Phenyl dominated surface.  $L^*$  resembles a sub-molecular critical load “capacity”.

<sup>†</sup> See subsection 1.2 (Fig. 1-5) for the definition of the reduced temperature  $T_R$ .

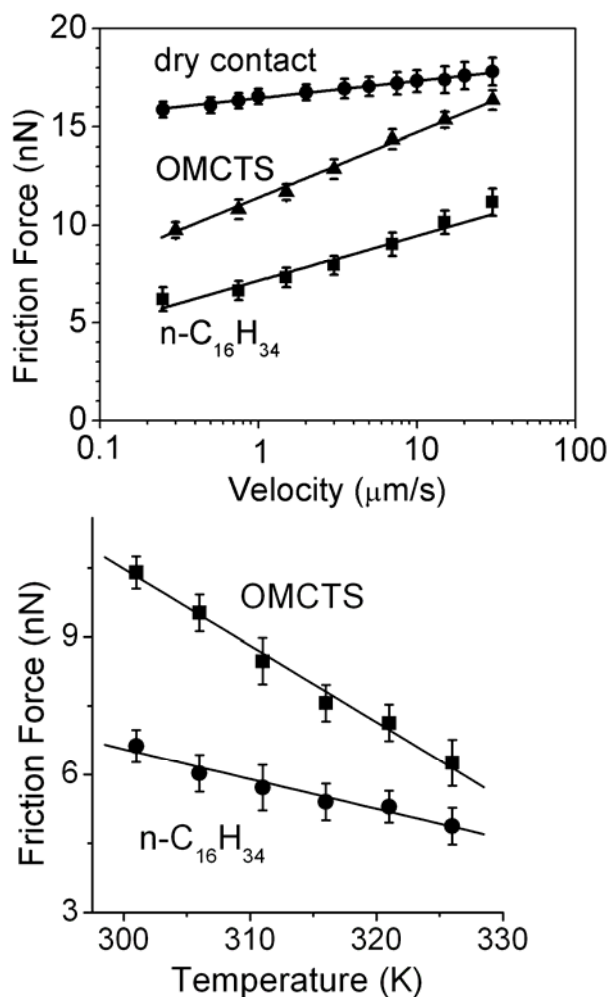
### 3.2 Liquid-Lubrication: Molecular, Interfacial and Dimensional Constraints

Contrary to dry or solid-lubrication, there has been since Reynolds in the late nineteenth century, a much better understanding developed regarding energy dissipation during sliding in liquids than in solids. The reason for the early success in obtaining improved basic insight into liquid lubrication is due to the incorporation of underlying fundamental theories such as fluid mechanics, rheology, and thermodynamics. This has been in general, as pointed out above, the shortcoming of dry friction analysis.

It is well known that the frictional resistance between solids is significantly reduced if lubricated. Various characteristic velocity dependencies have been found for liquid lubrication depending on the lubricant thickness (or more generally on the Gumbel number). In surface forces apparatus (SFA) and in our SFM studies,<sup>13</sup> it has been shown that friction involving liquids can exhibit a logarithmic behavior in velocity, which is contrary to Reynolds linear creep relationship. This transient behavior of liquids finds its counterpart in dry or solid-lubrication, where logarithmic behaviors have also been reported, as discussed above.

From a thermodynamic point of view, sliding discontinuities are caused by activation barriers, which are repeatedly overcome during the sliding process. Utilizing a thermodynamic activation model that goes back to Eyring (refined by Briscoe ~1980), we analyzed the energy dissipation process involving the "simple" liquids, n-hexadecane ( $n\text{-C}_{16}\text{H}_{34}$ ) and octamethylcyclotetrasiloxane (OMCTS).<sup>2</sup> As opposing solid surfaces served silicon-oxide nanoscale sharp SFM tips and ultrasmooth planar silicon-oxide wafers (5 Å roughness). The two liquids have been selected based on their similar chemical affinity to silicon, with distinctly different molecular shape; i.e., linear chain ( $n\text{-C}_{16}\text{H}_{34}$ ) vs. spherically shaped (OMCTS) molecules. We examined the degree of interfacial liquid structuring (c.f. sec. 2.3), and its contribution to localized shear processes. While shear approach curves provided the thickness of entropically cooled boundary layers, Fig. 2-7, a thermomechanical analysis involving friction-velocity data, as presented in Figure 3-8, reveals distinctly different tribological responses.

Friction-velocity plots were obtained with SFM cantilevers that were fully immersed in the liquid lubricant and scanned with a one  $\mu\text{m/s}$ -velocity in an apparent contact with a silicon surface at constant load and temperature.<sup>2</sup> As documented in Figure 3-8, logarithmic friction-velocity relationships,  $F_F(v) = F_o + \alpha \ln(v[\mu\text{m/s}])$ , were found for n-hexadecane and OMCTS. The measurements are compared to "dry"  $\text{SiO}_x\text{-SiO}_x$  contact sliding at 18 % relative humidity. Surprisingly on first sight, n-hexadecane exceeds OMCTS in its performance as a lubricant for asperity sliding within the observed velocity and temperature ranges. This result was unexpected at first as the OMCTS bulk viscosity is 30 % lower in comparison to n-hexadecane. After a modulated shear analysis (c.f. sec. 2.3), it became



**Fig. 3-8:** FFM measurements of n-hexadecane and OMCTS as function of velocity (top) and temperature (bottom).<sup>2</sup>



clear that the bulk-modified boundary layer of n-hexadecane was responsible for improved lubrication properties.

To analyze the lubrication process from an energetic perspective, we expressed the shear velocity as

$$v = v_o e^{-E_a'/(k_B T_R)}, \quad (3.3)$$

with the relaxation temperature  $T_R$ , and the apparent Arrhenius activation energy of the form

$$E_a' = Q' + P\Omega - \tau\phi. \quad (3.4)$$

As illustrated in Figure 3-9,  $Q'$  is the potential barrier height with respect to the plastic deformation,  $P$  is the pressure imposed,  $\Omega$  is the pressure activation volume,  $\tau$  is the shear stress, and  $\phi$  is the stress activation volume. With this *Ansatz*,

we followed Eyring's footsteps and discussed the liquid at rest in terms of a thermal activation model, wherein the individual liquid molecules experience a "cage-like" barrier that hinders molecular free motion, because of the close packing in liquids. The stress activation volume  $\phi$  can be conceived as a process coherence volume, and interpreted as the size of the moving segment in the unit shear process, whether it is a part of a molecule or a dislocation line. This model yields for the stress,<sup>2</sup>

$$\tau = \tau_o' - \beta T, \quad (3.5)$$

a linear relationship with temperature, and

$$\tau = \frac{k_B T}{\phi} \ln\left(\frac{v}{v_o}\right) + \frac{1}{\phi}(Q + P\Omega), \quad (3.6)$$

a logarithmic relationship with the scan velocity. Both are in accordance with our experiments, Fig. 3-8. Considering that the shear strength can be expressed as the friction force,  $F_F(v) = F_o + \alpha \ln(v[\mu\text{m/s}])$ , per unit area  $A$ , the following equation can be directly derived from Eq. (3.6) for constant temperature and pressure:

$$\frac{\phi}{A} = \frac{k_B T}{\alpha}. \quad (3.7)$$

The normalized stress activation volume of our study is provided in Fig. 3-10. As expected, the stress activation length (or coherence length) in a dry contact situation dominates the ones in lubricated junction. However it has to be pointed out that the origin of the activation barrier (or jump probability) in dry SFM friction experiments of incompressible material is not just caused by phonon excitations in the material, which are too fast to be observable, but by instability jumps (stick-slip) of the cantilever tip,<sup>23</sup> as addressed at the beginning of this section. To what extent lubricated SFM tip-sliding measurements reflect trapping probabilities is unknown. As there is a recognizable difference in the stress activation length between n-hexadecane and OMCTS (Fig. 3-10), for two liquids with similar chemical affinity and bulk rheology, we can conclude that the intrinsic molecular response time of the liquid (i.e. self-diffusion) is in part responsible for the liquid-specific  $F_F(v)$  relationship. In other words, n-hexadecane shows higher stress coordination than OMCTS. This interpretation is in accordance with the modulated approach measurements presented in section 2.3.

Studies such as this illuminate constraints imposed on liquids in the interfacial regime. They provide insight into the activation energies involved. In this particular case, we estimated based

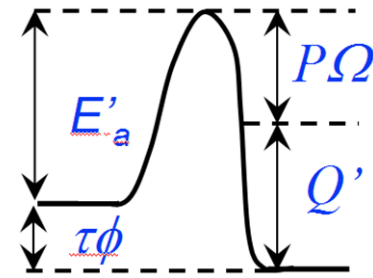


Fig. 3-9: Thermodynamic shear activation model.

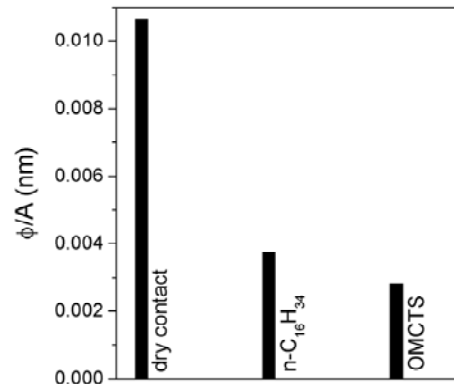


Fig. 3-10: Stress activation volume – a measure of the stress coordination.

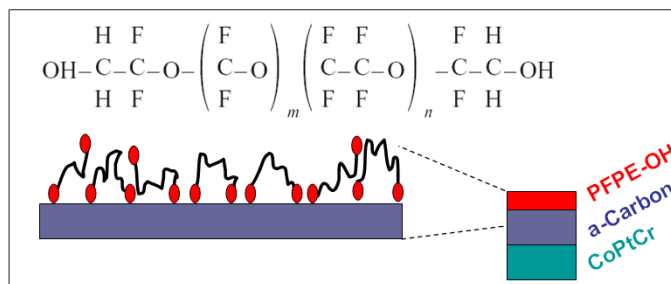
on the characteristic velocity,  $v_0=vd$  (composed of the process frequency,  $v$ , and a jump distance,  $d$ ) the process activation energy  $Q$  to be on the order of  $10^{-20}$  J.<sup>23</sup> Although the entropically cooled boundary layer is far from freezing, it shall be noted that the heat of fusion at the melting point is  $1.99 \times 10^{-20}$  J and  $8.85 \times 10^{-20}$  J for OMCTS and n-hexadecane, respectively. Thus, shear induced phase/structural changes are very likely to occur.

In summary, our research in liquid lubrication has focused on intrinsic constraints, and shear deformation. We have tried to avoid external pressure induced constraints (i.e., molecule trapping), and thus, have stayed as close as possible to the material equilibrated state. The research presented here gave us insight into molecular-shape-induced structuring if dimensional constraints are involved. It also showed the strong impact on frictional dissipation, which cannot be explained by viscometric data. Research that is on-going and planned will also involve to a greater degree temperature and size effects.

### 3.3 Two-Dimensional Polymer Liquids and Reaction Kinetics

Our research has been addressing over the years many aspects involving monolayer systems.<sup>5,9,13,19,20,22-25,36-40</sup> Of recent interest has been the interplay between thermomechanical properties of monolayers and their reaction kinetics towards substrates. This has shown to be of great importance, for instance, in hard drive lubrication involving “smart” lubricant monolayers, where the molecules have to backfill very quickly any lubricant layer defects after a slider impacts.

In collaboration with IBM we have studied the molecular mobility of hydroxyl-terminated perfluoropolyether (PFPE-OH) monolayer films, Fig. 3-11 that are widely used in lubrication of magnetic storage devices. These fluids exhibit spatially terraced flow profiles indicative of film layering, and a spreading dynamics that is diffusive in nature. In magnetic storage devices the hydroxylated chain ends of molecularly-thin PFPE-OH films interact with the solid surface, an amorphous carbon surface, via the formation of hydrogen-bonds with the polar, carbon-oxygen functionalities located on the carbon surface. The bonding of the PFPE-OH polymer to carbon depends on the ability of the PFPE backbone to spatially deliver the hydroxyl end-group to within a sufficiently close distance to the surface active sites.



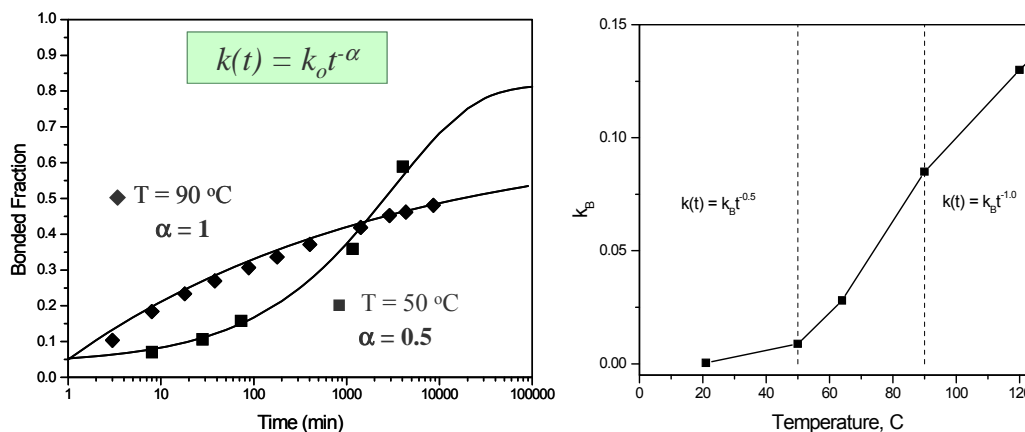
**Fig. 3-11:** PFPE-OH monolayer lubrication of wear protective amorphous carbon (a-Carbon) layer. Chemical formula Fomblin ZDOL<sup>®</sup>, a widely used PFPE-OH polymer.<sup>‡</sup>

Kinetic measurements probing the bonding of the PFPE-OH polymer to the carbon reveal two distinctive kinetic behaviors. Below 56 °C the kinetics are described with a time-dependent rate coefficient of the form  $k(t) = k_b t^{-1/2}$  and at temperatures above 85 °C with  $k(t) = k_b t^{-1}$ . Our kinetic experiments reveal an abrupt increase in the bonding rate constants,  $k_B$ , above ~50 °C as illustrated in Fig. 3-12.

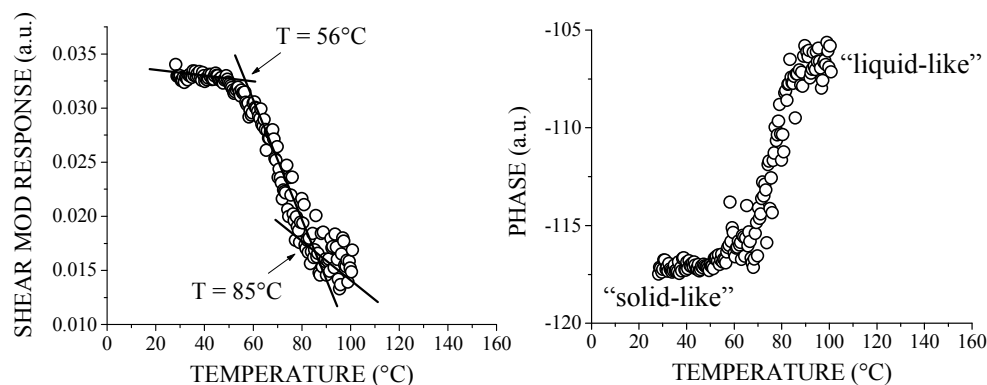
The bonding kinetics in the low-temperature regime is characteristic of a diffusion-limited reaction occurring from a glass-like state of the molecularly-thin PFPE-OH film. The mobility of the PFPE chain in the glass-like state is limited by the propagation of holes, or packets of free volume, which facilitate configurational rearrangements of the chain. The onset of changes in the

<sup>‡</sup> Fomblin ZDOL<sup>®</sup> is a random copolymer of perfluorinated ethylene oxide and perfluorinated methylene oxide

bonding kinetics at nominally  $T > 56^\circ$  signifies a fundamental change in the mobility of the molecularly thin PFPE-OH film. Specifically, the transition in the fractal time dependence suggests that delivery of the hydroxyl moiety to the surface is no longer limited by hole diffusion, and the increase in the initial rate constant indicates an enhancement in the backbone flexibility. These results are consistent with a transition in the film from a glass-like to a liquid-like state, as illustrated in Fig. 3-13, where the enhanced PFPE-OH segmental mobility results from rotations about the ether oxygen linkages in the chain that become increasingly facile. The time dependence observed in the high-temperature rate coefficients,  $k(t) = k_b t^{-1}$ , is characteristic of a process occurring from a confined liquid-like state in which the activation energy increases as the extent of the reaction increases.



**Fig. 3-12:** (Left) Representative kinetic data for the bonding of PFPE-OH (tradename: Fomblin Zdol<sup>®</sup>) to amorphous carbon at  $T = 50^\circ\text{C}$  and  $T = 90^\circ\text{C}$ . Solid lines represent fits using a rate coefficient of the form  $k(t) = k_b t^{-\alpha}$  with  $\alpha = 0.5$  for  $T = 50^\circ\text{C}$  and  $\alpha = 1.0$  for  $T = 90^\circ\text{C}$ . (Right) Change in bonding rate constants  $k_B$ . Temperature dependence of the initial bonding rate constants for a 10.5 Å PFPE-OH film. Vertical lines delineate the non-classical kinetic regimes.



**Fig. 3-13:** SM-FM Analysis on Zdol: (Left) Amplitude response reveals three regimes as found in the kinetic studies. (Right) Parallel measured out of phase response identifies the material phase as frozen below  $50^\circ\text{C}$  and in a liquid-like melt state above  $90^\circ\text{C}$ .

Currently, very limited research is conducted in analyzing reaction processes at interfaces with intrinsic thermomechanical material properties. Typical approaches are limited to statistical considerations and oversimplified rate models. This research illustrates the importance of the underlying molecular mobility on the reaction kinetics. As the molecular mobility within a condensed phase can be affected by a variety of physical constraints (internal, external, size, etc.), it is imperative to expand our efforts in investigation local thermomechanical properties, as it was illustrated in this section, and throughout the entire document.

## 4. Technological Applications - Nanotechnology

Nanotechnology is the meeting ground where today's industrial needs converge with fundamental sciences involving the nanoscale between atomistic and phenomenological theories. Technologies that could benefit from the nanoscale are manifold. They are situated in many areas, such as manufacturing, electronics, pharma and chemicals, biotechnology, and energy related disciplines.

A lot is expected from this new science and technology (c.f. Table 1). In manufacturing, for instance, one expects from the nanoscale to increase the performance of materials, and to discover and profit from unique material and transport properties. Nanostructured materials and processes are estimated to increase their market impact to about \$ 340 billion per year in the next 10 years (Hitachi Research Institute, 2001). In the pharmaceutical industry one predicts that half of the production will depend on nanotechnology in 10 to 15 years (Roco, Kluwer, 2001). Improved catalytic processes based on nanoscience will impact \$ 100 billion per year in the next two decades (Roco, Kluwer, 2001). It is expected that lighter and more durable materials can be processed. Improvements in renewable energy sources such as solar cells, and water filtration and desalination systems are anticipated. The projection is that in 10 to 15 years nanoscience and nanotechnology will reduce the worldwide consumption of energy by more than 10 %, which corresponds to a reduction of 200 million tons of carbon emission ("NNI: The Initiative and Its Implementation Plan," p. 93).

**Table 4-1:** Expectations from Nanotechnology

(Source: Roco and W. S. Bainbridge, Societal Implications of Nanoscience and Nanotechnology, Kluwer)

Affected Areas	Impact	Economical impact per year (in 10 to 15 years)
Manufacturing	- Nanostructuring - Materials properties	\$ 340 billion per year
Electronics	- Materials - Structure	\$ 300 billion per year
Pharma		\$ 180 billion per year
Chemicals	- Nanostructured catalyst	\$ 100 billion per year
Transportation	- Safer and lighter vehicles (based on materials and electronics)	\$ 70 billion per year
Energy (Sustainability)	- Reduction in energy use	\$ 100 billion per year (on savings)

Over the years, our group had the opportunity to contribute to nanotechnological advances in multiple areas, i.e., electro-optics (optoelectronics and photonics), energy production and mass separation systems and involving membrane and nanocomposite technologies, nano-electromechanical systems (NEMS) for electronic applications, biomedical device applications, to name the most effective ones. Thereby our focus has been to identify the origin for "exotic" material behavior, and to provide physical parameters to cognitively tailor synthesis efforts and/or manufacturing process parameters towards material and device engineering. Our efforts have been predominantly centered around organic materials, as they can be tailored with nearly endless variations in chemical structures opposed to inorganic materials that are mostly limited to elemental compositions.

In this section, some of our efforts will be summarized that are related to electro-optics, membrane technologies, and a NEMS application towards thermomechanical ultrahigh density digital storage.

## 4.1 Electro-Optics

In this subsection, I will discuss our involvements regarding two device technologies in electro-optics (optoelectronics and photonics) with focus on organic/polymeric materials. In regards of optoelectronics, I will address how interfacial constraints can be utilized to increase the device efficiency, and how early molecular mobility assessment of the material can provide important optimization parameters for the device manufacturing process. Furthermore, I will summarize our group's contribution in regards of organic NLO materials for photonic applications. Thereby, I will attend to current challenges in regards of device efficiency and stability, and offer solutions based on our group's involvement in molecular scale thermomechanical analysis.

### 4.1.1 Organic Optoelectronics

Over the past decade, material synthesis of novel light emitting polymers have made amorphous, disordered organic semiconducting materials interesting as an attractive alternative to state-of-the art inorganic materials used in light emitting diodes (LED). Polymers are attractive because of their mechanical properties. They can be easily shaped in any form, and their processing steps are fewer, and offer improved economical solutions than current device fabrications. Often, they exhibit unique properties, which present additional opportunities for exploration. For instance, polymers systems involving interfacial constraints, such as blends, have shown superior properties, such as more efficient energy transfer, or enhanced electroluminescence and lasing. We have focused in our research on two aspects: (i) the enhancement of LED efficiency based on interfacial constraints, and (ii) the development of material screening methodologies that provide step-by-step insight in the course of the manufacturing process to identify optimized process parameters.

**(i) Interfacial enhancement of LED material efficiency:** Polymer and organic LED devices involve thin films, on the order of 10 to 100 nm thickness, often in form of a single or two-layer structures that are sandwiched between two electrodes. It was found that in polymer systems, interfacial confinement effects are noticeable over distances of tens to hundreds of nanometers.<sup>11</sup> An example is the LED device performance in intensity and emission color that is strongly affected by interfacial constraints.<sup>11</sup>

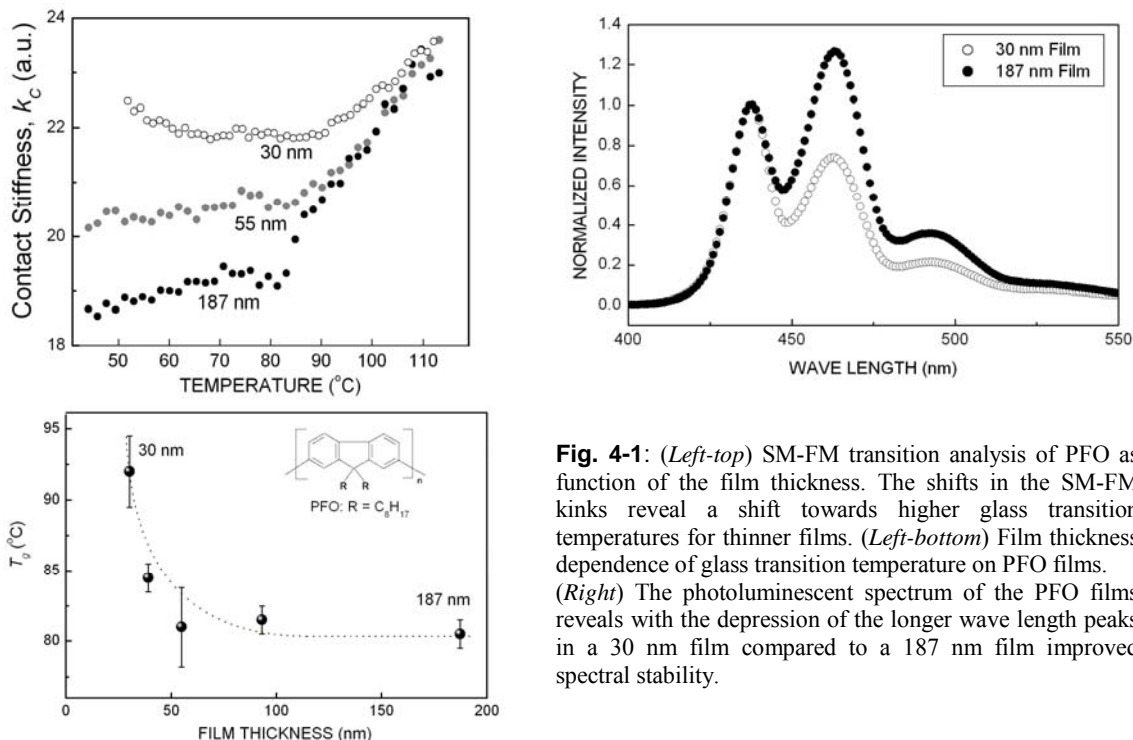
The interfacial confinement aspect shall here be illustrated with our study of poly(9,9-dioctylfluorene) (PFO) a promising blue light emitting LED diode material.<sup>41</sup> Polyfluorenes are of great commercial interest for display applications because of their blue color emission, high photoluminescence yield in the solid state (50%) and good charge transport properties. In dilute non-polar solvent solutions, polyfluorenes exhibit spectrally stable blue light emissions that are assigned to single intrachain excitons. Spin cast into thin films, polyfluorenes exhibit red-shifts, which are attributed to aggregate emissions in the solid state. Also, PFO tends to crystallize due to its rod-like molecular configuration, resulting in an undesired red shift in the photoluminescence (PL) signal, and reduced PL efficiency. To hinder crystallization, we investigated in PFO interfacial constraints towards suppressing molecular mobility.

Figure 4-1 illustrates interfacial constraints that take effect in PFO below a film thickness of ~50 nm.  $T_g$  was found to increase by 10 °C at a film thickness of 30 nm compared to the bulk, Fig. 4-1(*Left*). As an increase in  $T_g$  originates from a conformational change in the polymer, it can be expected that the optical properties are affected. This is confirmed with Figure 4-1 (*Right*), which reveals an altered photoluminescent spectrum for a 30 nm thick film compared to the bulk. Both the thick (187 nm) bulk film, and the thin-confined film show well-structured, vibronic peaks. The first peak (437nm), the second peak (463nm), and the third peak (493 nm) correspond to singlet exciton decay and are indicative of 0-0, 0-1, and 0-2 vibronic transitions, respectively, between the lowest levels of the first excited state to various vibronic levels of the ground state.

According to a study by Winokur *et. al.* (*Phys. Rev. B* (2003), **67** 184106), PFO or other conjugated polymers are, in general, neither homogeneous nor in equilibrium. At room temperature, PFO exhibits primarily a  $\beta$  conformation, i.e. ordered phase. The order-disorder

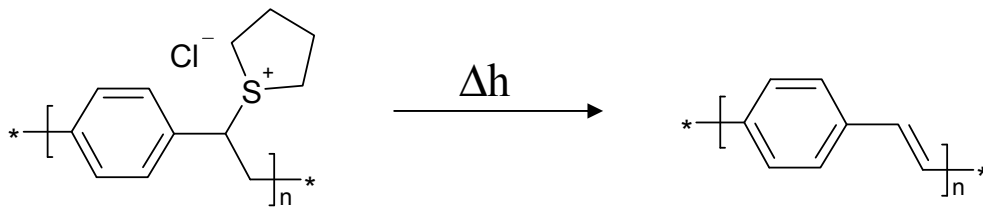
transition (ODT) is known to take place about 5 to 10 °C above the glass transition temperature. Winokur *et. al.* also found that the emission from 0-0 and 0-1 bands are due to residual  $\alpha$  conformation region of the polymer, i.e. the system is a mixture of the ordered  $\beta$  phase with patches of the disorder  $\alpha$  phases. Thus, based on the PL spectrum (Fig. 4-1) the 30 nm PFO films contains more of the  $\alpha$  phase, while the 187 nm PFO films contain more of the  $\beta$  phase. This led us, considering the thickness dependence of  $T_g$ , to conclude that the interfacial constraint in the 30 nm film depressed crystallization, and thus, inhibits the shift of the photoluminescent spectra to longer wavelengths due to intrachain excitons.

This study illustrates how molecular mobility, and, by extension, optical properties can be controlled by introducing dimensional constraints to optoelectronic polymeric systems.



**Fig. 4-1:** (Left-top) SM-FM transition analysis of PFO as function of the film thickness. The shifts in the SM-FM kinks reveal a shift towards higher glass transition temperatures for thinner films. (Left-bottom) Film thickness dependence of glass transition temperature on PFO films. (Right) The photoluminescent spectrum of the PFO films reveals with the depression of the longer wave length peaks in a 30 nm film compared to a 187 nm film improved spectral stability.

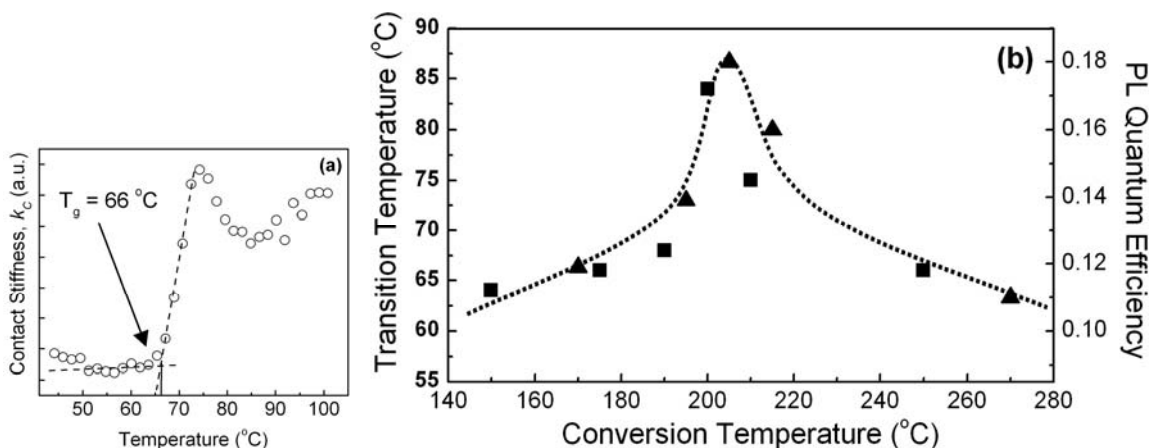
**(ii) Optimization of LED manufacturing conditions based on early material analysis vs. complex device analysis:** An inherent problem with LED materials, i.e., conjugated polymers, is their poor solubility in common organic solvents that prevents them to be easily processed into high quality thin films. One approach to circumvent this problem is the use of solution-processible precursor polymers that can be converted into active polymers. For instance, the precursor for poly(*p*-phenylenevinylene) (PPV), one of the most widely used and researched organic LED polymers, is the PPV sulfonium precursor. The thermal conversion process into PPV is illustrated in Fig. 4-2.



**Figure 4-2:** Thermal conversion of PPV from its sulfonium precursor.<sup>42</sup>

Problems with the post-casting conversion are, however, the generation of by-products, such as the formation of carbonyl groups (via oxidation), and residues of precursors, which require careful consideration concerning the conversion conditions, as they are one of the origin for a reduced electroluminescent efficiency.

Post-casting conversion generally causes smaller sized molecules that exhibit higher mobility, and are found predominantly at the interface. Thus, we studied the near surface glass transition process for thick ( $\sim 100$  nm) PPV sulfonium precursor films containing tetrahydrothiophenium (THT) leaving groups after they were converted into PPV for a range of conversion temperatures.<sup>42</sup> Near surface glass transition values, as determined in by SM-FM, Fig. 4.3(a), were determined as a function of the conversion temperature,  $T_{conv}$ . Figure 4-3(b) shows that the  $T_g$  relaxation process is strongly conversion temperature dependent. Thereby, the magnitude of the transition value is measure of the molecular mobility. In a system that is not well equilibrated, such as spun-cast, thin films of “bulky” polymers, an increase in molecular mobility can lead to enhanced but undesired conformational changes in the polymer matrix (e.g.,  $\pi$ -stacking).<sup>42</sup> Such conformational changes can result, for instance, in the loss of the spectral stability, or in other words, in a decrease of the PL efficiency.<sup>42</sup>



**Fig. 4-3:** (a) Representative thermal-rheological SM-SFM plot of PPV at a conversion temperature,  $T_{conv}$ , of 175  $^{\circ}\text{C}$ . (b) Qualitative comparison of the photo-luminescence (PL) efficiency ( $\blacktriangle$ ) with the rheological transition ( $\blacksquare$ ) as function of the PPV conversion temperature. The rheological transitions were measured with the SM-FM method. A dashed line has been added for trend enhancement.<sup>42</sup>

We superimposed the transition data in Figure 4-3(b) with the PL efficiency, and found as expected a striking qualitative resemblance of the two data sets, if plotted as function of the conversion temperature. The optimum PL efficiency and maximum glass transition value, obtained at around 205  $^{\circ}\text{C}$ , divides the data set into two regimes.

In the lower temperature regime ( $T_{conv} < 205$   $^{\circ}\text{C}$ ), we argued that incomplete PPV conversion is responsible for a low PL efficiency.<sup>42</sup> Unconverted polymer chains shorten the conjugation length, leading to reduced PL efficiency. At the same time, the residual byproduct from the conversion reaction acts as a quenching site through a heavy atom mechanism (spin-orbit coupling between exciton and sulfur atom), which in turn negatively impacts the PL efficiency. It should be noted that the PPV conversion is complete in the bulk system at around 160  $^{\circ}\text{C}$ .

The rheological data suggest that with increasing conversion (thus, PL efficiency), significant conformational changes occur in the material. This is similar to findings that significant geometrical rearrangements are required for the polymer chains to achieve a delocalized conjugated segment. The  $\pi$ -delocalization over adjacent aromatic rings, which increases the conjugation length and segmental stiffness, increases the activation energy for the  $T_g$  relaxation process. The degree of molecular rearrangement as function of the conversion temperature is

also noticeable in the measured film thickness, Fig. 4-4.<sup>42</sup> The thickness is found to steadily increase with  $T_{conv}$  in the lower temperature regime.

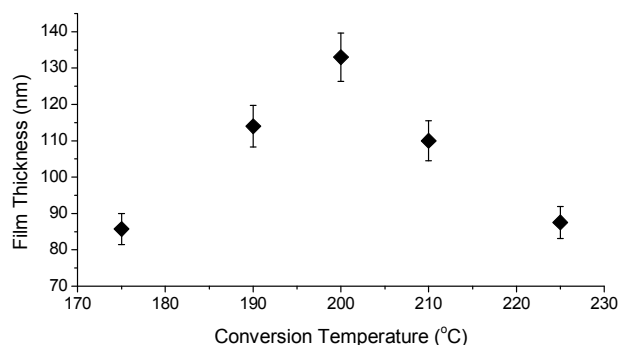
In the upper temperature regime ( $T_{conv} > 205^{\circ}\text{C}$ ), oxidative degradation processes, such as the formation of carbonyl groups, and aggregation processes due to crystallization reduce the PL efficiency.<sup>42</sup> Since oxidative degradation occurs by breaking the vinylene  $\pi$  bond, the flexibility of the backbone chains is consequently increased. This increase in flexibility is known to decrease the value of  $T_g$ . Thus, the decrease in  $T_g$  with increasing  $T_{conv}$  above  $205^{\circ}\text{C}$  can be interpreted as enhanced oxidation in the film. The thickness-conversion temperature plot in Figure 4-4 suggests that in the upper conversion temperature regime, significant reorganizations in the film occur that can be attributed to crystallization, which in turn depresses the PL efficiency.

What is particularly appealing concerning this study is that the PL efficiency can be pre-assessed for a system, which in its final "sandwiched" device form is very difficult to analyze. Such a pre-assessment is desirable, as additional complications involving the electrodes and interfacial transport resistances can be excluded, and analyzed later independently. That indeed nanoscale thermomechanical property analyses predict a variety of transport phenomena has been a repeating and promising scheme of our research. In the next subsection, this notion will be further emphasized with another technological example, this time it is situated in photonics.

#### 4.1.2 Photonics

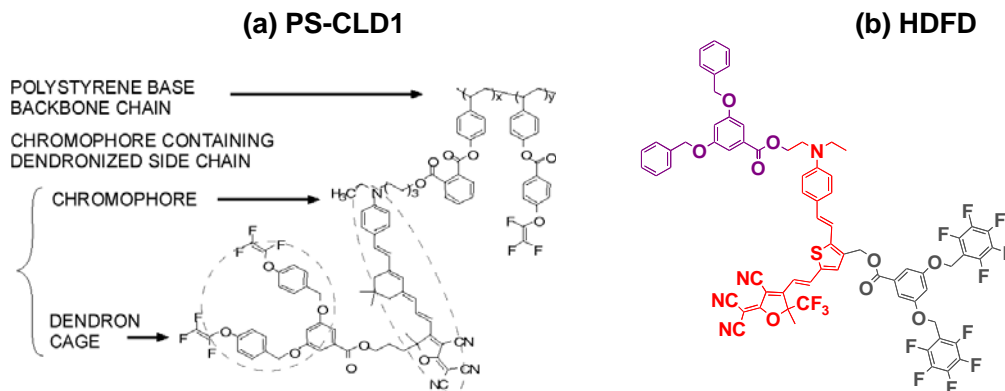
Organic based NLO materials for photonic applications have been of interest due to their superior electro-optic (EO) properties, the mechanical and processing advantages of organically synthesized materials, and most importantly, because of the tunability of their EO properties upon molecular design. Recent advances in the design of chromophores guided by theoretical descriptions of structure-function relationships has enhanced non-linearity by more than two orders of magnitude.<sup>3,6,10,43</sup> In the pursuit of highly efficient electro-optic photonic materials, however, one struggles with translating high molecular non-linearities, involving dipole moment carrying chromophores, into large macroscopic EO activities.<sup>3,6,10,43</sup> Currently, our efforts are directed towards the generation of stable assembly of acentrically ordered chromophores within an organic matrix based on cognitive molecular design approaches. The challenges we deal with are as follows:

Highly dipolar chromophores are susceptible to undesirable aggregation that originates from the anisotropic rod-like molecular shape of the chromophores and their strong electrostatic interaction forces. An apparent solution to reduce chromophore aggregation is to lower the loading density of the chromophores, which in turn, however, moderates the EO activity. A possible way out of this dilemma, and a way to achieve a high loading density with minimal chromophore aggregation, is the "site-isolation" approach, where bulky constituents, e.g. dendrimers, are grafted to the chromophores, as illustrated in Fig. 4-5(a).<sup>6,10</sup> The dendrimers act as chromophore cages thereby screening the electrostatic forces and shifting the overall shape of the chromophores from an anisotropic rod-like shape to a more spherical one. We explored this approach experimentally and theoretically for a variety of systems with positive results.<sup>4,6,10</sup> Another approach to reduce dipole annihilation with high chromophore density involves self-assembled EO molecular glasses through strong phenyl-perfluorophenyl ( $\text{Ph-Ph}^{\text{F}}$ )  $\pi$ - $\pi$  interactions to improve poling efficiency and chromophore alignment stability, Fig. 4-5(b).<sup>3,4</sup> This novel class of EO materials resulted in EO coefficients exceeding those reported for NLO polymers, Fig. 1-8, as discussed in subsection 1.1 (Fig.1-4).



**Fig. 4-4:** PPV film thickness as a function of the conversion temperature determined by profilometry.





**Fig. 4-5:** (a) Dendronized side-chain EO polymer, PS-CLD1.<sup>4,6,10</sup> The dendron moiety is attached to the chromophore containing side chain that is connected to the polystyrene-base backbone. (b) Glass forming chromophore containing molecule with phenyl and pentafluorophenyl rings incorporated as peripheral dendrons on the  $\pi$ -bridge and the donor-end of the chromophores, HDFD.<sup>3,4,43</sup>

An important problem still in need of a solution is the development of an effective field poling process of NLO materials, and the production of high non-linearity with long term stability of acentric order. This problem is generally only addressed by trial-and-error approaches. To approach the problem from a guided fundamental perspective demands knowledge about inter- and intra-molecular mobilities of the complex condensed organic EO materials systems.

The general theme in designing chromophore NLO polymer systems has been to increase the glass transition temperature, thus reducing the mobility of the chromophore moiety. However, this approach also reduces the poling efficiency, due to hindered molecular mobility. Thus, what seemed to be at first sight a suitable approach demands a high degree of delicacy, and, a more subtle approach to achieving mobility has to be taken. While there are many cross-linking approaches reported in the literature, most contain obvious deficiencies. For example, thermoset cross-linking processes are triggered under poling conditions, which hardens the matrix while poling is still in progress. As a result, the EO activity is lowered. Ideally, the poling process should be separated from and followed by the cross-linking process. Moreover, to maintain the achieved polar order of the resulting chromophore alignment, the cross-linking reaction should be triggered only under very mild conditions, preferably without further temperature elevation. To accommodate these requirements, we are currently also investigating NLO side-chain chromophore systems with delayed crosslinking abilities based a reversible Diels-Alder cycloaddition reaction, integrated into a chromone-type chromophore side-chain NLO polymer (Jen, *Macromolecules* **37**, 688-90 (2004)). This approach provides high mobility NLO solid state organic material with excellent solubility for spin casting, and improved thermal stability of the poled order.

Considering the complex molecular NLO building blocks described above, and the desire to locally control the orientation of the chromophore subunits, we employed novel microscopic tools and methodologies, i.e., SM-FM and IFA, as described above in subsection 2.2 and throughout section 1, respectively. We used these tools towards direct investigation of available relaxation processes within the organic matrix (see Fig. 1-1 and Fig. 1-3), their activation energies (see Figs 1-5 and 1-10) and their cooperative phenomena (see Figs 1-5 and 1-10). As discussed previously, dendronized side-chain EO polymers, such as PS-CLD1, and self-assembling NLO molecular glasses (e.g., HDFD) revealed temperature windows bordered by distinct submolecular relaxations appropriate and necessary for effective acentric poling. Energy determinations involving IFA revealed the submolecular origin of relaxation processes, and thus, valuable input for the synthetic design for the next generation of organic NLO materials. In consequence, SM-FM and IFA has proven to be a viable alternative to the current trial-and-error approaches. That chemical synthesis can indeed profit from experiments as described above and yield superior

acentrically ordered NLO materials with higher EO activity was illuminated with an example in Figure 1.2 and a discussion in subsection 1.1.

The electro-optical research, summarized here, considered two distinct approaches for material manipulation. While in optoelectronics interfacial constraints were used to increase the device efficiency, in photonics, intra- and intermolecular constraints were employed. With the study of the conversion process in conjugated polymers, a methodology was introduced that provides a pre-assessment of the electronic transport properties on a step-by-step basis during the device manufacturing process. That indeed also mass transport properties can be pre-assessed with local thermomechanical analyses is addressed in the next subsection.

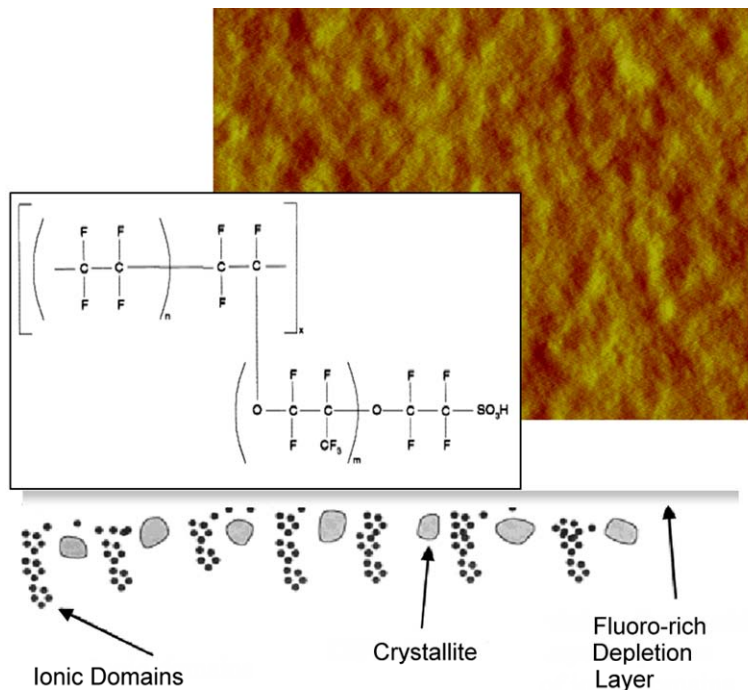
## 4.2 Membrane Technology

Thinking of heterogeneous membranes and mass transfer there are two major constraints that come to mind: (i) The constrained motion of molecules through membranes, and (ii) material constraints within the membranes imposed by material heterogeneities and the presence of interfaces. In this regards, our past and current research interest has been focusing on two polymer transport systems: (a) Polymer electrolyte membranes (PEM) that are known for their complex heterogeneous internal structure, and (b) nanocomposite membranes with imposed interfaces. Here, I will summarize our efforts on water transport through PEM Nafion<sup>®</sup> and reverse selective nanocomposite membranes involving stiff, and high free-volume conjugated polymers.

### 4.2.1 PEM Fuel Cell

To date, the most widely used polymer electrolyte membrane (PEM) material in fuel cell application is Nafion<sup>®</sup>, an ionic copolymer (ionomer). It consists of a poly(tetrafluoroethylene) backbone with short perfluoro-polyether pendant side chains terminated by ionizable sulfonate groups, as depicted in Figure 4-6. A complex organized structure, when swollen in a polar solvent (water or alcohols), is responsible for excellent ionic conductivity and electrochemical and chemical resistance. Our current understanding of the Nafion structure is that it resembles a three dimensional array of inverse micelles that are interconnected by short channels acting as transient crosslinks. The micelles, 30 to 50 Ångstrom in size, consist of ionic end groups from the side chains that are clustered together in solvent-containing aggregates within the apolar perfluorocarbon matrix.

Nafion membranes are rigid systems with poor proton conduction unless a polar solvent is absorbed. For insufficiently hydrated Nafion membranes, the proton transport is slow, and thus, the conversion efficiency negatively affected. On the other hand, excess water can lead to cathode flooding in the system, resulting in a reduced efficiency. Good water management usually requires balancing the electro-osmotic drag and diffusion of water. It has been realized that the microstructural properties of



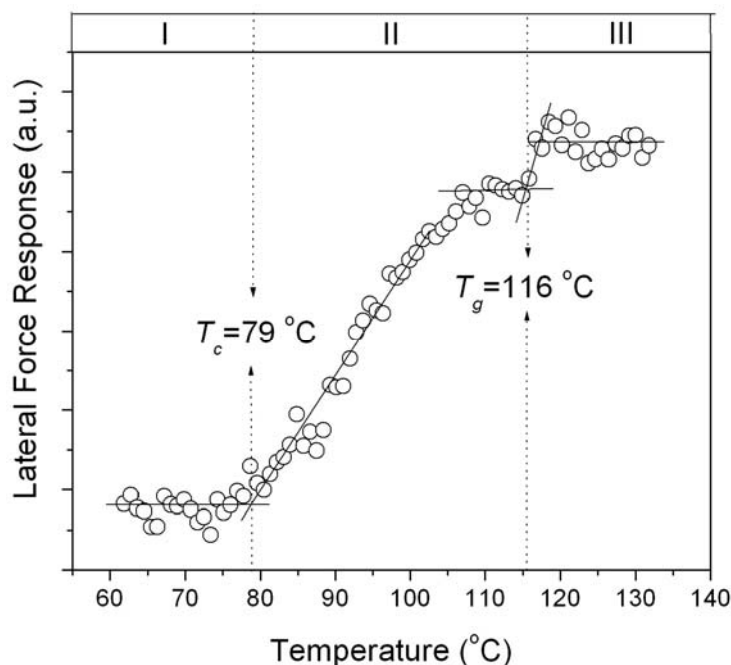
**Fig. 4-6:** PEM Nafion<sup>®</sup>: Chemical Structure, cartoon of condensed phase with ionic domains, imaged by AFM (300 nm horizontal scan).

the membrane are very important in explaining solvent swelling.

Besides water transport, the gas permeability, in particular of oxygen and hydrogen, is of significance for an effective PEM membrane operation. Originally, it was argued that the gas permeation is mainly either through the hydrated ionic cluster region, or through the hydrophobic amorphous region of the membrane. Recent experiments, however, showed that both regions have to be considered for gas transport.

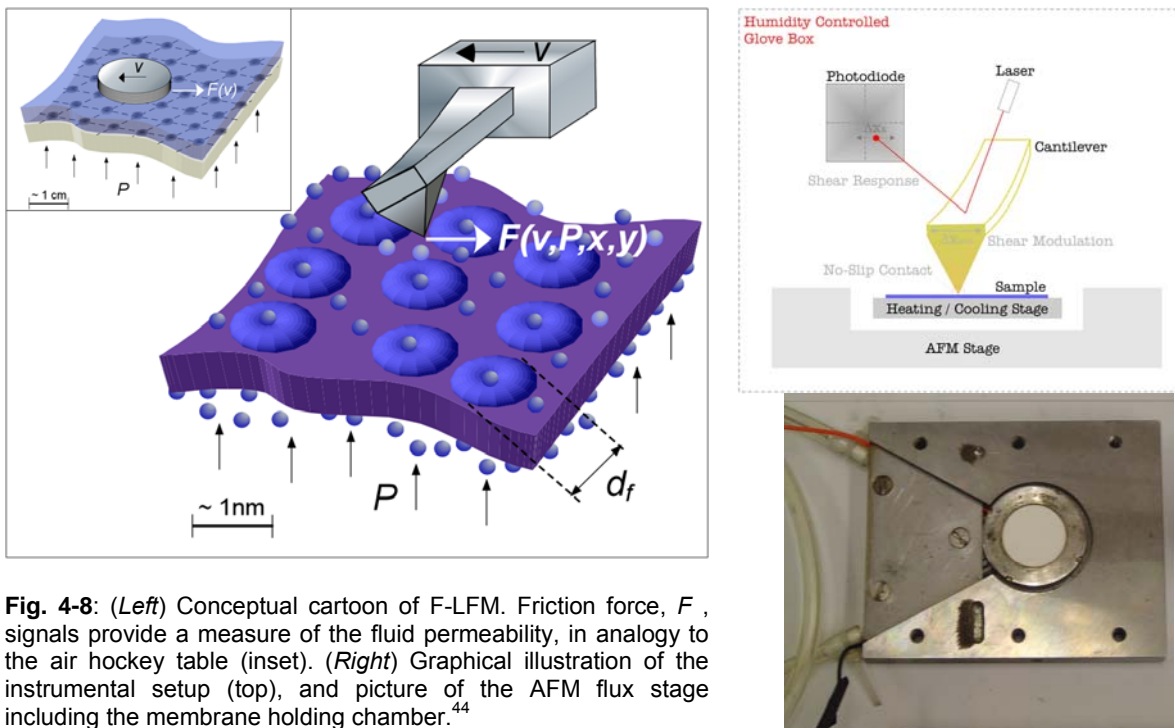
Over the past decades, the main research focus has been on the solvent swollen membrane. It was found that a decrease in resistivity around 80-90 °C is due to a reduction in the activation barriers for proton motion, which is generally attributed to the availability of water to ionize the sulfonic acid groups. Considering the complexity of Nafion that intertwines a rheological polymer cluster network with the intricacy of solvent swelling and ionic conductivity, it is desirable to investigate gas transport and swelling in conjunction with the rheological relaxation properties of the polymer matrix.

We approached this problem first with an SM-FM thermo- mechanical transition analysis applied to non-dehydrated membranes, Fig. 4 7.<sup>44</sup> A structural transition at 79 °C, about 30 to 40 °C below the glass transition temperature of Nafion (H<sup>+</sup> form), was found for the dehydrated membrane. To directly connect this low temperature transition to the membrane's transport ability of water, we had to devise an instrumental approach that is sensitive enough.



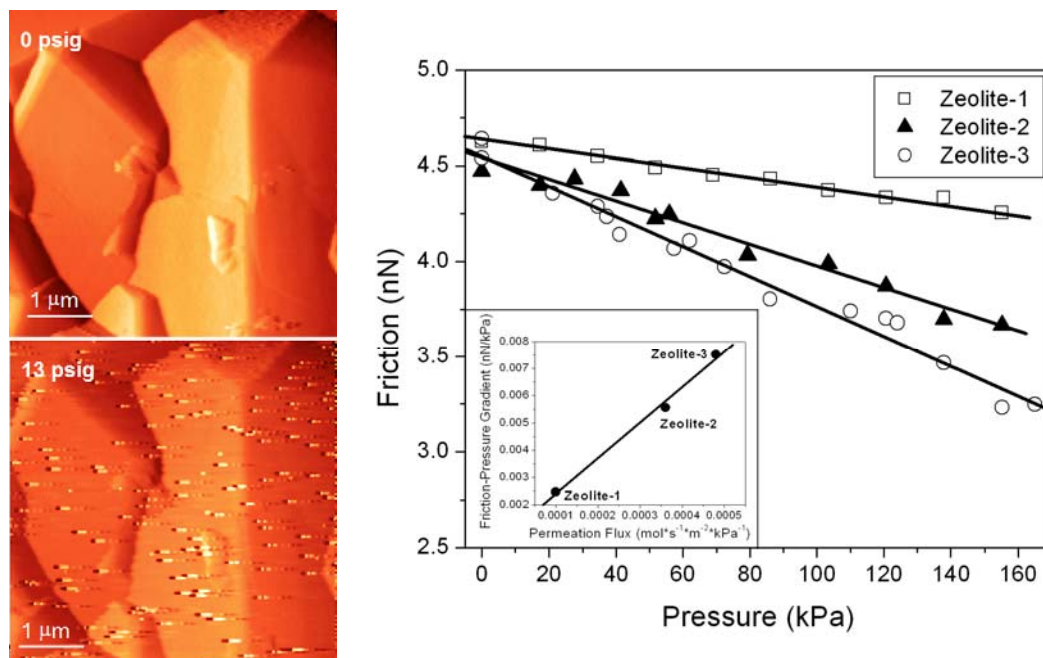
**Fig. 4-7:** SM-FM analysis of dehydrated Nafion (EW of 1100). Shear response forces reveal two transition temperatures that identify three regimes. Regime I and III reflect the glass state and the rubber melt state of Nafion, respectively. Regime II encompasses the creep regime over which the cantilever sinks into the polymer matrix to equilibrate the contact pressure, and the saturation regime that defines the phase between the glass and rubber states.<sup>44</sup>

Considering the intricacy between locally constrained membrane properties, and the selective permeation of analytes and solutes through porous and non-porous, organic and inorganic, heterogeneous systems, it is perceivable to look for a probe that provides *in-situ* microscopic information about the local permeability. Naturally, scanning force microscopy (in particular, lateral force microscopy LFM) comes to mind. Not unlike the principle of an air-hockey table, where the puck experiences the air cushion as a friction reducing medium, it can be imagined that a LFM cantilever sliding over a membrane that is penetrated by a fluid is subjected to "lubrication". This brought forward the development of flux-lateral force microscopy (F-LFM), as illustrated in Fig. 4-8.<sup>44</sup>



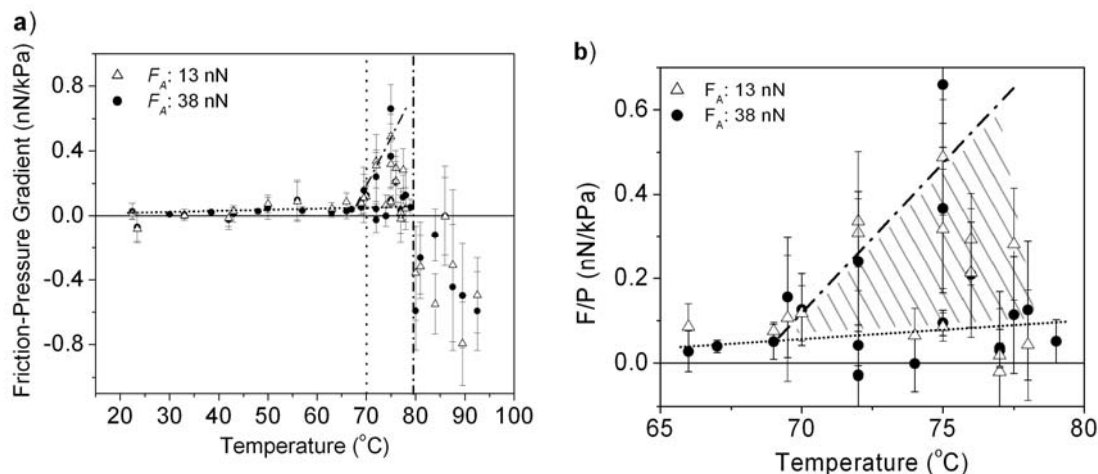
**Fig. 4-8:** (Left) Conceptual cartoon of F-LFM. Friction force,  $F$ , signals provide a measure of the fluid permeability, in analogy to the air hockey table (inset). (Right) Graphical illustration of the instrumental setup (top), and picture of the AFM flux stage including the membrane holding chamber.<sup>44</sup>

Our in-house developed F-LFM technique was calibrated with MFI zeolite membranes (micropore sizes of  $\sim 0.5\text{ nm}$ ) of known macroscopically determined  $\text{N}_2$  permeabilities. From linear lateral force vs. permeate inlet pressure plots (FP plots), Fig. 4-9, we deduced the membrane specific FP gradients, and found them to be proportional to the measured  $\text{N}_2$  permeabilities of three zeolite standard membranes. This result indicated that FP gradients offer a direct measure of nanoscale permeabilities.<sup>44</sup>



**Fig. 4-9:** MFI zeolite membranes. (Left) AFM images illustrate the importance of membrane purging prior to F-LFM analysis due to organic contamination (bottom). (Right) F-LFM analysis reveals direct linear correspondence between FP gradients and macroscopic permeation fluxes.

With F-LFM, we explored the impact of the structural reorganization at 79 °C on water transport in a commercial Nafion 115 PEM membrane. The membrane was placed onto the airtight membrane holding chamber, Fig. 4-8, through which it was exposed to a hydrated nitrogen gas on the upstream side. The downstream side of the membrane, kept dry by a nitrogen < 10% RH nitrogen environment, was probed by a cantilever tip at a constant sliding velocity. The results of this study are presented in Figure 4-10. It provides the first direct observation of water transport through a Nafion membrane. Up to a temperature of 70 °C, the *FP gradients* increase steadily, as found for the permeability of nitrogen through Nafion. Between 70 °C and the low-temperature matrix relaxation at 79 °C two distinct signal responses occur in the *FP gradient* plots, highlighted in Figure 4-10(b), one belonging to the nitrogen transport and the other one to water transport. Above 79 °C, the sign of the *FP gradients* is reversed, indicating that the friction force increases with pressure. In this regime, the cantilever experiences a water-swollen membrane with masked nitrogen transport and dominant water transport. In contrast to the “incompliant” zeolite membrane, the Nafion polymer membrane is elastically and plastically deformed by the tip, which exerts pressures in the contact zone on the order of 100 MPa. Particularly plastic deformations can dominate any other source of frictional dissipation. Thus, as the qualitative behavior of *FP gradients* below 79 °C is a direct consequence of nitrogen and water permeation, above 79 °C, it is dominated by the deformation properties of the swollen Nafion membrane. Based on our study it can be concluded that a structural transition at 79 °C within the Nafion matrix is responsible for sufficient water transport. It explains the poor performance of Nafion membranes below ~80 °C, as water, the osmotic transport system for the protons, is trapped within the membrane. Future research, involving for instance IFA, is necessary to provide molecular scale insight into the transition process at 79 °C. It can be expected that the structural relaxation affects the ionic clusters, and thus, opens up a gateway for water to diffuse.



**Fig. 4-10:** F-LFM measurements Nafion 115 PEM membrane.<sup>44</sup> (a) FP-gradient analysis at an applied load of 13 nN (triangle) and 38 nN (dot). The regime up to the vertical dashed line at 70 °C reflects an increase in the nitrogen flux (visually enhanced by the dotted trend line). Nominally increased fluxes are observed above 70 °C, and below the low temperature matrix relaxation of dehydrated Nafion at 79 °C (indicated by the second vertical dashed line). Above the 79 °C mark, the force pressure gradient is reversed, reflecting the changes of the water-swollen PEM membrane. (b) Zoom into the transition region (dashed area) where the onset of water transport is recognizable. Water and nitrogen transport are occurring simultaneously as indicated by the dashed lines. Two distinct signal responses occur in between 70 °C to 79 °C indicative of the two transports of nitrogen (dotted line) water (dotted-dashed line).

Besides providing fundamental insight into material and transport properties of complex and constrained material our group is also involved in device developments. That shall here be briefly

illustrated concerning an ultrathin design of a PEM fuel cell device using a soft lithographical technique involving poly(dimethyl-siloxane) PDMS.

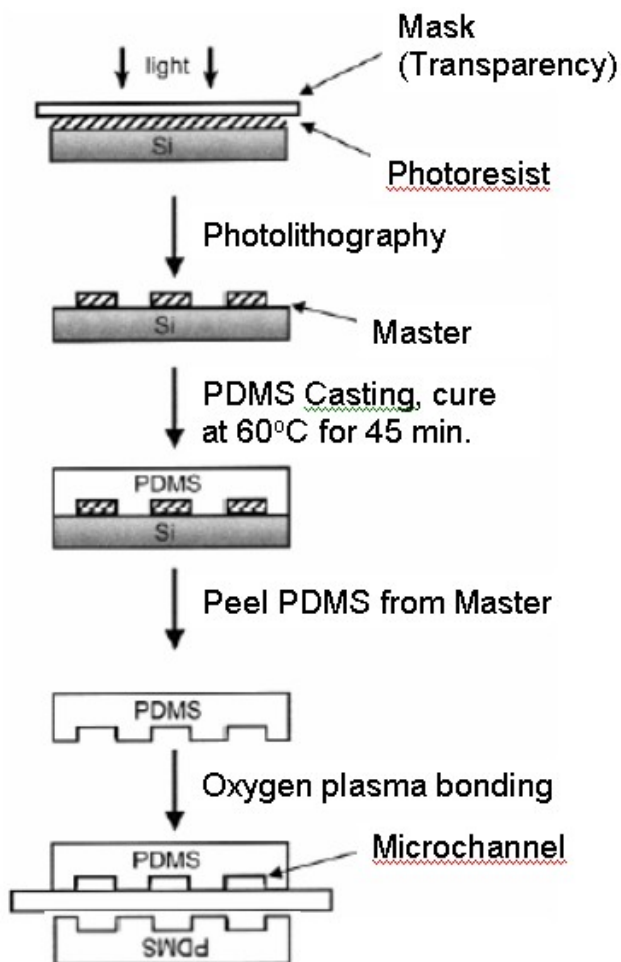
The target of our design have been the generation of flow field plates with micro-channels (see Fig. 4-11) This design was motivated by the desire

- (i) to slow down the flow velocity of the fluids within the flow field plates with dimensional constraints, which results in an increase in the “fuel” efficiency,
- (ii) to lower the manufacturing process by avoiding the expensive graphite flow field plates, and
- (iii) to provide mechanical flexibility to the fuel for multiple reasons.

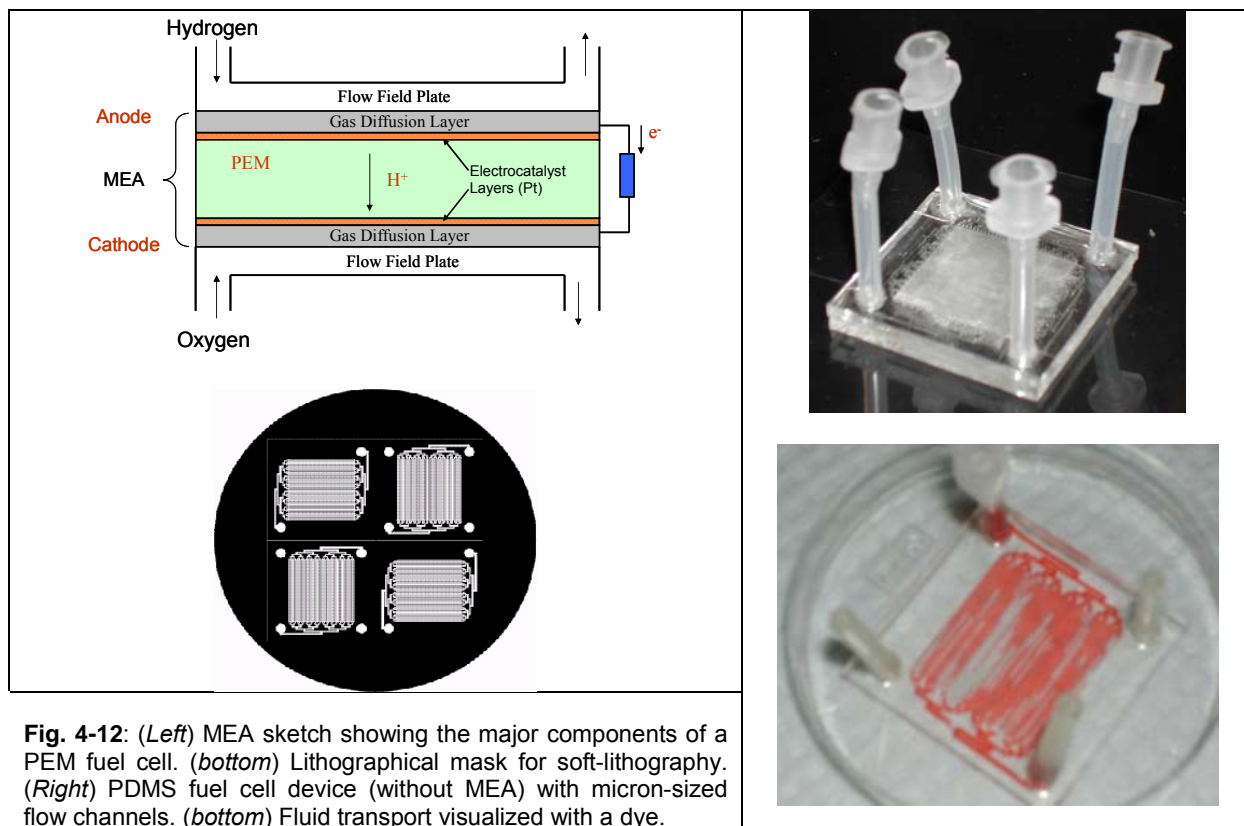
A very costly component in PEM fuel cell stacks is the bipolar/end flow field plates. They account for more than 80 % of the total weight, and are very expensive to manufacture. Currently, the flow field channels are machined or molded into bipolar plates of graphite or compression molded blanks of filled poly(vinylidene fluoride) (PVDF) polymers. A cost alternative to graphite is compression molded thermoset plates with molded-in channels, which cost only one-fifth compared to graphite. Channel flow analyses (Kumar et al. (2003) J. Power Source) indicate that a decrease in the channel width that results in an increase in the pressure drop is improving the fuel cell performance, as it shifts the transfer process type of the reactant gases towards the electrode-membrane reaction interface from diffusion to forced convection.

As illustrated in Fig. 4-12(Left), the flexible membrane electrode assembly (MEA) containing the PEM membrane is sandwiched between the flow field plates in state-of-the art PEM fuel cells. The bulky (non-flexible and heavy) parts are the graphite based flow field plates. With soft-lithography, as described in Figure 4-11, involving flow field masks of the sort presented in Fig. 4-12(Left) with microscale dimensions of flow channels, we fabricated a flexible fuel cell device, Fig. 4-12(Right). First studies showed good flow performance. On-going work focuses on involving material such as PVDF for actual fuel cell operation.

Thus, while our group’s research and engineering involvement in fuel cell applications, has focused on establishing an understanding of the internal complexity within a complex polyelectrolyte membrane system and its impact on mass and consequently electric transport properties, our research effort described in the following subsection is attentive to mass transport in interfacially constraints systems. Our specific attention is on reverse selective transport in nanocomposite polymer membranes.



**Fig 4-11:** Fabrication (soft lithograph) of the PDMS Flow Field Plate.



**Fig. 4-12:** (Left) MEA sketch showing the major components of a PEM fuel cell. (bottom) Lithographical mask for soft-lithography. (Right) PDMS fuel cell device (without MEA) with micron-sized flow channels. (bottom) Fluid transport visualized with a dye.

#### 4.2.2 Nanocomposite Membranes

Of particular interest to the chemical processing industry are reverse-selective membranes (also called solubility-selective or vapor-selective), which can be used for separating larger organic molecules from smaller permanent gases. These membranes find numerous chemical and refining industry applications including removal of higher hydrocarbons from methane, olefin separation from nitrogen, and removal of hydrogen from refinery process gas streams.

While the pore-transport model can be used to understand transport in high free volume glassy polymers, the solution-diffusion model is more generally applied. According to the solution-diffusion model, permeability within a membrane for use in vapor separation can be expressed as the product of the sorption (or solubility) coefficient ( $S$ ) of a penetrant,  $A$ , in the membrane times the concentration averaged diffusivity ( $D$ ) of the penetrant through the membrane:<sup>10,32</sup>

$$P_A = S_A \times D_A \quad (4.1)$$

Sorption in glassy polymers can be understood according to the dual mode sorption model, composed of a combination of dissolution described by Henry's Law and Langmuir surface sorption:<sup>32</sup>

$$S = k_D + \frac{C'_H b}{1 + bp} \quad (4.2)$$

where  $k_D$  is Henry's constant,  $b$  is the Langmuir hole affinity parameter,  $C'_H$  is the Langmuir capacity parameter and  $p$  is the system pressure. Diffusion through membranes is often understood as being primarily a function of free volume, i.e.,

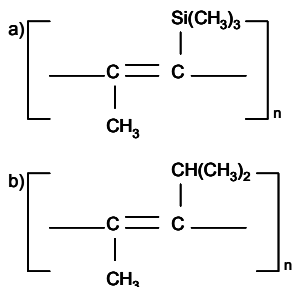
$$D_A = C \exp(-\gamma v_A / V_{FV}) \quad (4.3)$$

where  $C$  and  $\gamma$  are polymer-specific constants,  $v_A$  is a critical void volume necessary for the diffusion of  $A$ , and  $V_{FV}$  is the average void volume of the material. For the separation of multiple

(e.g. two) penetrants, equation (4.1) can be utilized to determine the selectivity,  $\alpha$ , of two penetrants, *A* and *B* as:

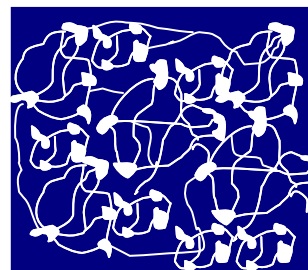
$$\alpha_{A/B} = \frac{S_A}{S_B} \times \frac{D_A}{D_B}. \quad (4.4)$$

Smaller molecules generally have higher diffusivities than larger molecules. Thus, when solubility coefficients are similar, the diffusivity ratio ( $D_A/D_B$ ) dominates in equation (4.4) and selectivity favors smaller molecules (i.e., is size selective). There are, however, polymers where the solubility ratio becomes the dominant term in the determination of selectivity. Included in this group of polymers are: poly(4-methyl-2-pentyne) (PMP) and poly[1-(trimethylsilyl)-1-propyne] (PTMSP) and its analogues.<sup>32</sup> These polymers have been shown to exhibit high reverse-



**Fig. 4-13:** Structures of (a) PTMSP and (b) PMP.

Neat PTMSP (and similar polymers) are understood to have high free volume as a result of the inefficient chain packing of their rigid backbones, bulky pendant groups and poor interchain cohesion. Their free volumes exhibit a bimodal distribution, with sub-nanometer cavities. It has been theorized that these cavities create a series of nanoporous interconnected free volume cavities, thus giving rise to unique high-permeability. This understanding of polymer structure is qualitatively illustrated in Figure 4-14. It is important to note that the polymer system is dynamic, and thus, the channel elements displayed in Figure 4-14 are transient with nanosecond lifetimes. The materials exhibit reverse-selective behavior due to the fact that large organic molecules absorb to the matrix walls within the small free volume elements thereby creating resistance to transport for smaller, permanent gases.



**Fig. 4-14:** Structure of high free volume glassy polymer

By incorporating fumed silica nanoparticles into the reverse selective membranes, it was found that the permeability and diffusivity of the material is increased. Fumed silica addition had little effect on penetrant solubility, indicating that enhanced diffusivity is primarily responsible for increased permeability. Increases in free volume are thought as origin for improved permeability. Subsequent studies with PTMSP/silica nanocomposites have also confirmed an enhancement in free volume with increasing filler content using both <sup>129</sup>Xe NMR spectroscopy (G. Consolati et al. (2006) Polymer Phys) and PALS (A. J. Hill et al. (2005) J. Mol. Structure). A very interesting finding was that at higher silica loadings in PTMSP/FS the permeability of small permeates such as H<sub>2</sub> and methane increased more than the permeability of larger organic vapors such as propane and n-butane.

When fumed silica nanoparticles are incorporated into the polymer matrix the rigid chains are unable to efficiently pack around the particles. This results in a high free volume interfacial region between the polymer and fused silicon particle of low-density polymer that allows gas molecules to diffuse more rapidly, as qualitatively illustrated in Figure 4-15. The morphology of this interfacial region is critical for determining overall transport properties. It has been theorized that conventional solution-diffusion will dominate in the interfacial region as long as void volume



increases do not result in continuous channels. Relatively large continuous channels will allow pore flow transport mechanisms (i.e. Knudsen diffusion) which favor small molecules, resulting in the loss of reverse-selectivity. This phenomenon has been demonstrated experimentally (T.C. Merkel et al, (2003) Macromolecules).

Since the discovery of reverse-selective nanocomposite membranes, much research has been directed toward the study of bulk properties and tailoring them for specific applications. Bulk property improvement through various methods has been achieved by variation of nanoparticle size, variation of bulk filler content and methods for modifying silica particles with functional groups for incorporating nanoparticles into the polymer phase. Although all these property studies have greatly contributed to the understanding of the capabilities of reverse-selective nanocomposite systems, there are still many unresolved key issues, which demand microscopic insight of local variation in the material and transport properties, and more sophisticated processing conditions. The key research issues, our group is focusing on, are obtaining information about local

- impact of interfacial constraints leading to enhanced reverse-selective mass transport,
- effect of the filler particle on polymer material properties,
- experimental confirmation of fundamental interfacial transport models,
- result of filler aggregation on membrane performance, and
- molecular relaxations at the polymer-filler interface that contribute to age susceptibility.

All of these issues are associated with property variations within the nanocomposite membrane and require microscopic probing methods, such as SM-FM, IFA, F-LFM, and heated tip atomic force microscopy (HT-AFM – Fig. 4-16). The objective of our research is to gain basic insight into reverse selective transport by manipulation of filler properties and spacing, with the ultimate goal to develop highly efficient, selective and stable membranes based on fundamentals.

As pointed out throughout this document, tailored nanoscopic tools are paramount for investigating nano-constrained systems. For analyzing the interfacial strength between the nanoparticles and the polymer matrix, we employed heated tip atomic force microscopy towards, a methodology that has been pioneered by our group.<sup>10,32,45</sup> HT-AFM allows for local investigation of interfacial debonding as well as local nano-

thermomechanical analysis. *Briefly*: HT-AFM utilizes gradient doped resistive cantilever materials to integrate heating directly into the cantilever probe. Figure 4-16(a), illustrates the complexity of a resistive cantilever, and provides two plots of the cantilever normal deflection signal  $Z$  as function of the calibrated local temperature (for PS and PMMA). The local temperatures were obtained from calibration plots on a variety of material standards with well known transition values, as documented in Figure 4-16(b). Thereby, the maximum “turning points” in normal

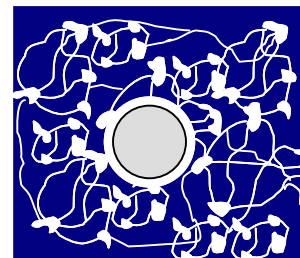


Fig. 4-15: Sketch of membrane structure with single silica nanoparticle.

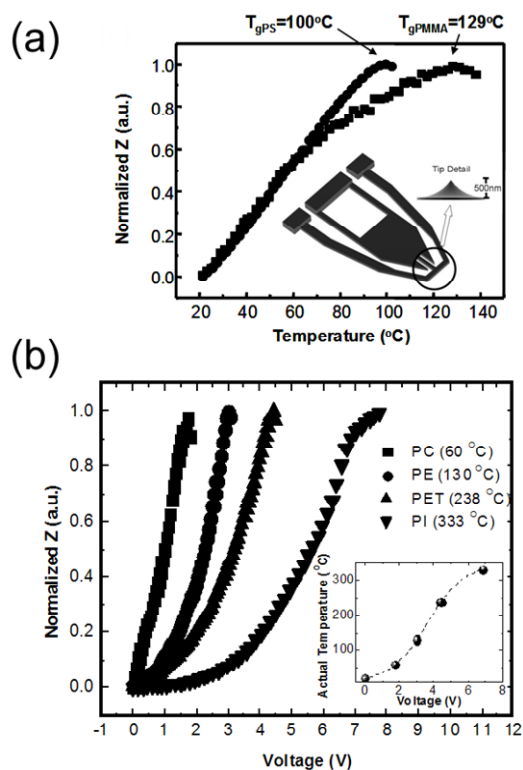
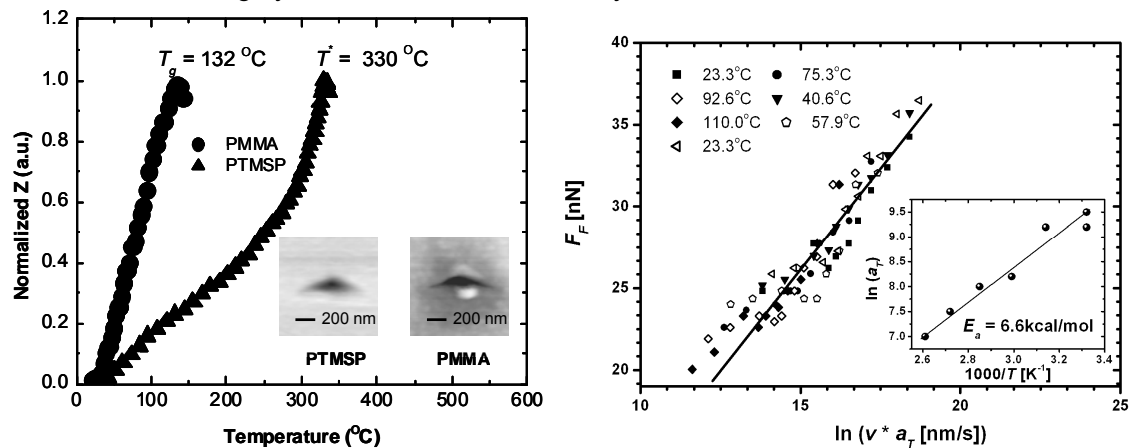


Fig. 4-16: HT-AFM: (a) Lever deflection vs. calibrated local temperature. (b) Temperature calibration based on transition values of calibration standards.

deflection vs. cantilever applied voltage plots, Fig. 4-16(b), are equivalent to the glass transition values of the standards.<sup>32</sup> Compared to substrate heating methods such SM-FM, HT-AFM offers some distinct advantages. Foremost is the ability to heat locally to higher temperatures. Other advantages of HT-AFM over global sample heating include the ability to operate at very high heating rates due to the low thermal mass, and the ability to perform multiple measurements on specimens that are highly sensitive to thermal history.



**Fig. 4-17:** (Left). HT-AFM transition analysis for PMMA and PTMSP. The inflection at  $\sim 200$  °C of PTMSP is indicative of partial degradation. (Right) IFA of PTMSP below 110 °C reveals an activated process of 6.6 kcal/mol that is identified as TMS side-chain mobility.<sup>10,32</sup>

Figure 4-17(Left) exhibits for PTMSP a HT-AFM transition value  $T^*$  of 330 °C. As per our studies, it is indicative of the PTMSP decomposition paired with the glass transition.<sup>32</sup> IFA experiments, Fig. 4-17(Right), revealed as the only activated transition process below  $T^*$ , the trimethylsilyl (TMS) side-chain rotation around the C-Si bond (see Fig. 4-13).

As for practical applications involving PTMSP membranes, the degradation temperature is avoided in the manufacturing process, the TMS side-chain mobility is of vital significance for the membrane properties. If we consider, for instance, in analogy the side-chain mobility of polystyrene, discussed in subsection 3.1, and its orientational preponderance towards the free surface, it is reasonable to assume that also TMS exhibits an enhanced or reduced presence within the free volume regimes of PTMSP. As there is a noticeable difference in the interaction between the TMS group and monoatomic  $H_2$  and diatomic  $CO_2$ , it is reasonable to assume that the TMS contribution towards the relative sorption amount of the two molecules within the free volume of PTMSP is essential. This aspect is currently still under investigation.

Shifting now from neat PTMSP to interfacially constrained nanocomposite PTMSP-fumed silica systems (PTMSP-FS), we can expect as visualized in Figure 4-15, an increase in void spaces. As addressed above, PTMSP-FS is known for its unique improved permeability and reverse selectivity with increased filler concentration up to some level. This behavior however is not unexpected, if we consider our previous discussion. It could be explained by the preferential orientation of the TMS groups in regards of the introduced void space interfaces. Besides a local alteration of the interaction field (some of us would call it “chemistry”), one has however also to consider a physical (phase) change of the polymer matrix towards the composite interface, as discussed in great detail in section 2.

To evaluate the interfacial properties of PTMSP-FS composites, we employed HT-AFM, and investigated the adhesive strength between PTMSP and silica, by controlled debonding of single nanoparticles from the glassy matrix.<sup>32,45</sup> Figure 4-18 reveals that debonding occurs consistently at a temperature tens of degrees below the decomposition temperature of PTMSP. This suggests increased polymer mobility in the interfacial region. The debonding strength was inferred from the torsional bending force of the HT-AFM probe when impacting the particle. With this, HT-AFM has

shown to provide two additional attributes besides of being a thermal transition also to embody a highly sensitive force sensor and a thermomechanical manipulator.

We could also determine the debonding force. It was deduced by integrating the impact peak from onset to peak force, i.e.,<sup>32</sup>

$$E_{db} = \int_{\alpha} \Delta F dx . \quad (4.5)$$

where  $\alpha$  is the impact duration to peak force,  $\Delta F$  is the force relative to the baseline friction, and  $x$  is the lateral position of the scanner. With this a total debonding energy of  $1.5 \times 10^{-5}$  nJ could be determined. The same experiment conducted with PS and PMMA showed it very difficult (high forces) to remove silica particles from the matrices. As the adhesive forces of PS and PMMA bracket the one of PTMSP, the debonding observations of the three polymers provides the first direct evidence that the actual PTMSP surface coverage of the particles is significantly diminished, due to interfacial void formations as addressed above.

In conclusion, our research on reverse selective polymer membrane materials and nanocomposites revealed the mobility of side chains and the formation of interfacial voids very likely responsible for the unique increase in reverse selectivity and permeability in PTMSP-FS nanocomposites. On-going research in our labs involving nuclear magnetic resonance (NMR) experiments and dielectric spectroscopy will provide further insight into the interfacially driven mass transport properties.

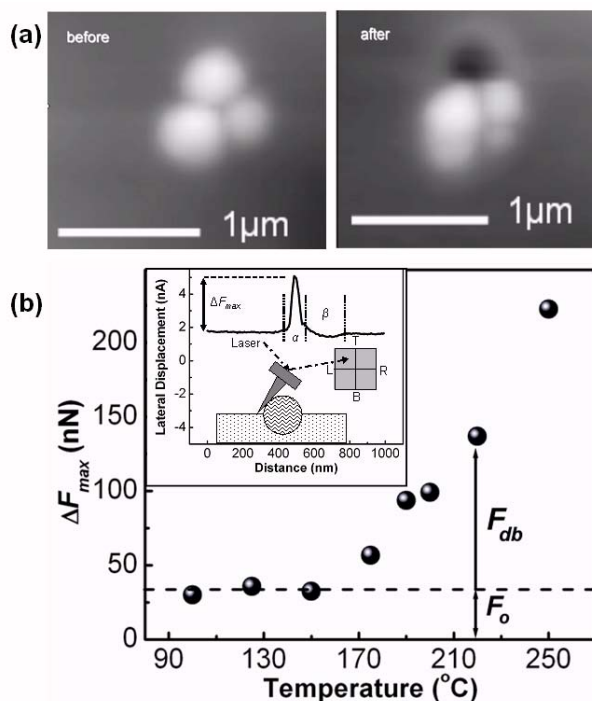


Fig. 4-18: (a) PTMSP-FS nanocomposite images before and after a HT-AFM tip temperature of 250 °C. (b) Lateral impact force  $\Delta F_{max}$  (see inset) as function of temperature. Debonding occurred above 200 °C.  $F_o$  and  $F_{db}$  indicate the base force and debonding force, respectively.<sup>45</sup>

### 4.3 Digital Storage – Thermomechanical Ultrahigh Density Recording

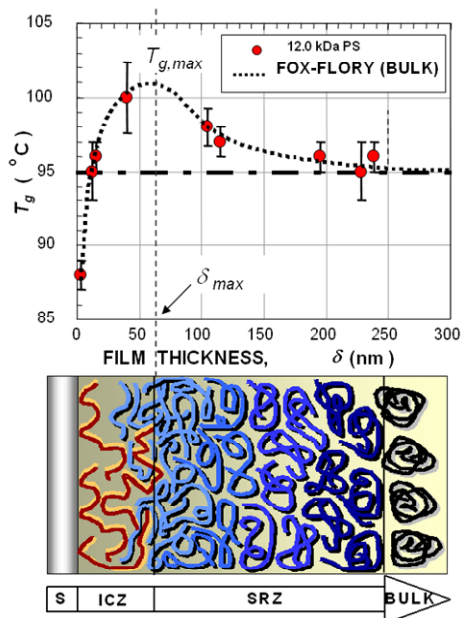
In the previous subsections on technological applications, the focus has been in understanding and influencing transport properties based on constraints in materials. I illustrate here how also Nanoelectromechanical System (NEMS) processes can benefit from material constraints. The focus is on ultrahigh density storage by means of nanoindentation.

In section 2, I summarized some of our results concerning interfacial constraints on ultrathin films. In particular in spin cast polymers, we found within the 100 nm boundary region to the substrate a non-linear glass transition profile, as redrawn in Figure 4-19. While analyzing a novel device technology of an ultrahigh density digital storage recording scheme pioneered by IBM, originally named the *Millipede NEMS project*, and today known as *thermomechanical data storage (TDS)*, we realized the importance of the anisotropic interfacial mobility for this application.<sup>29,31</sup> The TDS methodology entails a nanometer sized thermal-indentation bit writing process in ultrathin (~30 - 50 nm) polymer films. For films that exceeded the critical thickness  $\delta_{max}$  at which the glass transition reaches a maximum in the  $T_g(\delta)$  profile, we found excessive rims around the TDS bits, while less pronounced rims were detected for  $\delta < \delta_{max}$ . Our study not only revealed the importance of the local transition property (mobility) towards stress adsorption in the

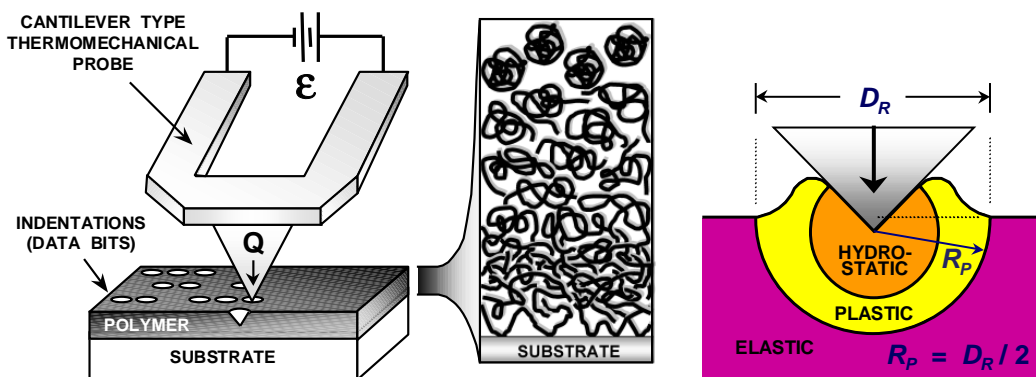
polymer matrix, but also provided first solutions by tailoring  $T_g(\delta)$  profiles accordingly (c.f. sec. 2.2). Our findings<sup>29,31</sup> shall here be a little further reiterated.

The thermomechanical data storage methodology, one of the few true NEMS applications, relies on writing, reading, and erasing nanometer sized data bits in thin polymer films, offering densities up to  $Tb\text{ in}^{-2}$ . In essence, the TDS writing operation is a high speed (MHz), elastic-viscoplastic polymer indentation process, Fig. 4-20, involving on the order of 1000 resistively heated and parallel operated cantilevers. The polymer storage media must be designed to achieve the narrow range of physiochemical properties necessary for: high data density, fast data rates, high durability, long shelf life, and low power consumption. The ideal polymer should be easily deformable for bit writing; however, the written bits must be stable against dewetting, thermal degradation, and wear.

The writing and erasing processes rely on local deformation of the polymer film, and to exploit the enhanced molecular-chain segment mobility above the glass transition point, these processes are conducted at a local temperature above  $T_g$ . Elastic recovery of displaced material is prevented by rapidly quenching the indentation site to below  $T_g$ , with the probe tip in place. As a result, the deformation is *frozen in* because the motion of molecular-chain segments is effectively inhibited below  $T_g$ . In order to preserve the recorded data, any further deformation of the polymer film must be limited during read-back and scanning; therefore, these operations are conducted below  $T_g$ , where molecular-chain segmental mobility is effectively inhibited.



**Fig. 4-19:** Anisotropic glass transition profile in polystyrene towards a solid silicon surface reveals anisotropy in the material structure and dynamics as sketched.<sup>7</sup>



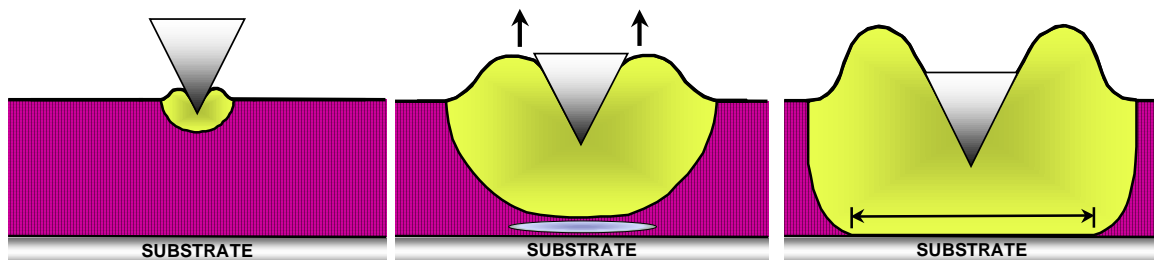
**Fig. 4-20:** Scanning Probe, Thermomechanical Data Storage: Creating uniform bit indentations in sub-100 nm thick polymer films requires an understanding of the interfacial rheology. (Left) TDS illustration with resistively heated cantilever. (Right) Illustration of a phenomenological matrix deformation model with rim formation.

In addition to achieving the appropriate  $T_g$ , the polymer film should exhibit a large drop, by orders of magnitude, in the shear modulus ( $G$ ) at  $T_g$ . When the probe tip is indented into the polymer during writing and erasing (above  $T_g$ ), the polymer is strained, and elastic shear stresses are incorporated into the film in the vicinity of the indentation. Unlike the deformation of a simple liquid, the indentation represents a metastable state of the deformed volume. The driving force for recovery of the initial unstressed state is directly related to the magnitude of the incorporated

elastic stresses. In the interest of bit stability, elastic recovery should be avoided; hence a low shear modulus, leading to reduced internal stresses during the indentation process (above  $T_g$ ), is desirable. To further promote longevity of recorded bit indentations, the strain applied to the polymer film during the reading/scanning operation, below  $T_g$ , must be minimized, and a higher shear modulus is desired. The higher modulus, assuming a constant adhesion force, will result in reduced friction forces, thus a reduced potential for wear.

The thermomechanical storage technique also requires specific attention to the local thermal transport properties of the polymer media and underlying substrate. Ideally, the heat transfer to the polymer should be limited only to the indentation site so adjacent data bits are not subject to thermal degradation, and the excess heat should be removed through the supporting substrate, a heat sink. This requires that the polymer medium has a very low thermal conductivity relative to the substrate. The heat transfer from the probe tip to the polymer is highly nonlinear, making it very difficult to reproducibly control tip penetration into the polymer, and hence, to maintain small uniform bit indentations. In order to overcome this difficulty, the depth of the tip penetration must be limited. The use of ultra-thin polymer films (<100nm) on a hard impenetrable substrate is a necessary and sufficient means to limit tip penetration. With this configuration, the hard substrate prevents the tip from penetrating farther than the film thickness.

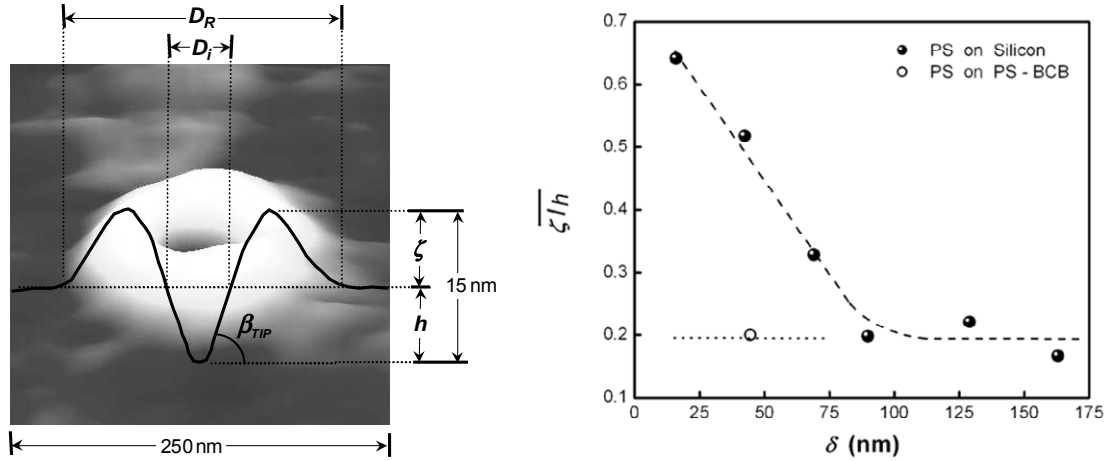
Each indented bit generated with the TDS process represents a metastable state of the deformed volume, and will either initiate spontaneous dewetting (film instability) or strive for recovery of the initial unstressed state (bit instability). The delicate balance between these instability nodes constitutes one optimization scenario in the design of polymeric storage media. Furthermore, media (and data) wear must be minimized during scanning operations. In particular, topographical protrusions, in the form of piled-up *rims* around the indented bits, Fig. 4-20 (Right), are regions susceptible to wear. The presence of rims also adversely affects the writing density. Rims interact non-linearly with adjacent bits, lowering the signal-to-noise ratio of bit detection and requiring a relaxation of the indentation pitch (data density). From the perspectives of media wear and data density, a suitable polymer storage media exhibits a weak propensity for rim formation during indentation. Interfacially constrained systems like TDS, are impacted during indentation by material rheological gradients (i.e.,  $T_g(\delta)$  profile) in addition to mechanical constraints (illustrated in Fig. 4-21) from the underlying substrate. The combined influence of rigid dimensional constraints and material anisotropy during indentation has been addressed in our research with high-rate, SPM indentation studies typical of the TDS process.<sup>29,31</sup>



**Fig. 4-21:** Evolution of the plastic zone: (Left) Bulk behavior (self similarity), (Middle) Strain shielding (substrate effect, results in enhanced rim formation), (Right) confined plasticity (interfacial shear behavior).

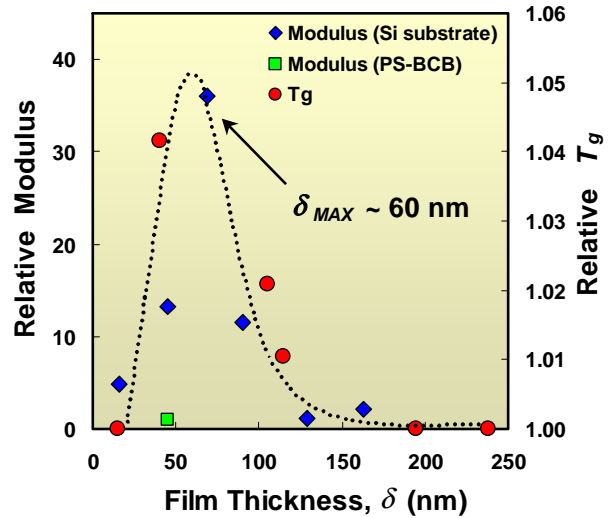
A representative indentation is presented in Figure 4-22(Left) Our research showed that the rim height  $\zeta$  is influenced by both process conditions (e.g. normal force,  $F_N$ ) and the film thickness, and scales with the indentation depth  $h$ . Thus, substrate constraints are best assessed via the ratio of the rim height to the indent depth,  $\zeta/h$ . In Figure 4-22(Right), the load normalized height to depth ratios,  $\overline{\zeta/h}$ , are reported for indentations in thin polystyrene films ( $M_w = 12k$ ). For film thicknesses,  $\delta$ , exceeding  $\sim 100$  nm, the  $\overline{\zeta/h}$  ratio displays a constant value, which reflects the bulk material response. For film thicknesses below 100 nm, the rim height increases with decreasing film thickness. This behavior depends on the substrate material. The rim

enhancements were effectively masked by adding a compliant 230 nm thick crosslinked buffer film polystyrene-benzocyclobutane (PS-BCB) between the rigid substrate and the indented PS film. It is important to note that the indentation depth was less than 10 % of the film thickness, which excludes strain shielding effects as cause for the increase in rim heights below 100 nm thick films.



**Fig. 4-22:** (Left) AFM image of a residual indentation in polystyrene with rim height,  $\zeta$ ; indentation depth,  $h$ ; rim diameter,  $D_R$ ; and indentation diameter,  $D_i$ . (Right) Strain shielding at the substrate interface is evident in the load normalized ratio of rim height to indentation depth ( $\zeta/h$ ). For PS on a rigid silicon substrate, rim heights are enhanced for films thinner than 100 nm. A compliant PS-BCB buffer masks the substrate constraints.

A final analysis, in which we compared the effective modulus of indentation with the change in the glass transition, at last disclosed the underlying molecular origin for the enhancement of the rim.<sup>31</sup> Thereby, we compared the phenomenological *effective modulus* that the indenter experiences during an indentation with the local glass transition  $T_g(\delta)$ . The combined plot of the two quantities as function of the film thickness, Fig. 4-23, reveals the significant qualitative similarity between the modulus and  $T_g$ . Thus, viewing the glass transition as a molecular mobility barrier (c.f. sec. 2.1), the molecular mobility strongly affects the TDS process. As higher mobility (more precise a positive  $d(T_g(\delta))/d\delta$  gradient) leads to smaller rim heights the critical thickness  $\delta_{max}$  represents an important engineering parameter for TDS. First important steps have been explored by our group in collaboration with IBM on crosslinked material as discussed in subsection 2.2,



**Fig. 4-23:** Combination plot of the effective modulus and the local glass transition. The qualitative correspondence is reflective of the impact of local mobility changes on the indentation mechanics.

With the TDS NEMS application we investigated an ultrahigh density recording scheme that is strongly affected by the underlying molecular mobility in the heterogeneous interfacial region of materials. In summary, our applied research towards devices in opto-electronics, membrane technology and NEMS illustrates the wide applicability of our research on intra/intermolecular and interfacial/dimensional constraints in materials.

in opto-electronics, membrane technology and our research on intra/intermolecular and interfacial/dimensional constraints in materials.

## 5. Classification and Summary

The prior sections of this report provided a review of our group's research at the University of Washington. The intent was to present more than just a compilation of our efforts, but to transmit the motivation that drives our research, the technical challenges we (the society) face, and to introduce the onset of a classification scheme of nanoscience based on *constraints* that offers a cognitive approach towards developing future technological solutions. It also provides the framework for research expansions.

An approach such as this has to break out of the boundaries imposed by traditional academic disciplines, and thus, our research involvements have to be multidisciplinary. Our efforts reflect in many ways the approach taken in the vast field of Chemical Engineering, a discipline that has been known, in the past at least, for its interdisciplinarity and particular strength in physical sciences. The challenge with interdisciplinarity is the possible loss or the lack of an identity. The most modern example is Nanotechnology, which is currently just only a compilation of technologies that are impacted by the sub-one-hundred nanometer scale. It is insufficient just only to pair researchers and engineers from different disciplines, and then assume an identity to arise. It is the common "language" and "philosophy" that has to be developed. Again, I like to refer to Chemical Engineering in the past that linked successfully Physics with Chemistry and Engineering. In the process, it developed a language and understanding of its own that showed very effective. Nanotechnology is missing such a common language, as it lacks (i) a well defined driving force in form of well defined (overarching) objective, and (ii) a science based classification scheme that is effective.

Here, I contrast two commonly made classification attempts with a scheme that evolved in the course of our research. Table 5-1 lists, with the first two perspectives on *materials* and *manufacturing*, two common classification schemes that are widely used in attempts to bring some structure into the immense field of nanotechnology. Unfortunately both do not provide a coherent basis and result in a laundry list of topics (not shown here). In analogy, Chemical Engineering faced a similar dilemma with their classification scheme of Unit Operations, which originally was very insightful but lost with increasing process complexity its appeal. It was replaced by a transport classification concept (Transport Phenomena), which was at its time revolutionary, as it provided the appropriate logical foundation for this growing field. Thus, in response to the demand of a fundamental classification scheme for Nanotechnology, I propose in Table 5-1 a third scheme, that is based on constraints.

From a science perspective, I have recognized *constraints* to provide the most effective characteristics of Nanotechnology. It offers a subdivision that is tied to fundamental aspects in Thermodynamics, Statistical Mechanics, Quantum Mechanics, and Transport Phenomena (including also electronic transport). In this document, I tried to convey, to some degree, with our research this perspective.

Taking both an *internal and external perspective* of our research involving molecular mobility, we have investigated

- *inter- and intramolecular constraints* in organic systems with enhanced rotational degrees of freedom (c.f. sec. 1.1 and 4.1.2) and stiff and conductive backbones (c.f. sec. 4.1.1), polymers with dissociation groups in aqueous solutions (c.f. 4.2.1), and highly translationally mobile and linked molecular systems (c.f. sec. 1.3).

Furthermore, we explored

- *interfacial and dimensional constraints* in terms of cooperativity (c.f. 1.2), critical transitions and instabilities (c.f. sec. 2.2 and 2.1.1), entropic cooling (c.f. sec. 2.3 and 3.3), free volume (c.f. 4.2.2), and finite size (c.f. 2.1.2).

Our research has tight constraints to *reaction kinetics* (c.f. 3.4) and *transport phenomena*, such as energy dissipation (c.f. 3.1 and 3.2), photonic and electronic transport (c.f. 4.1.1 and 4.1.2), mass transport (4.2.1 and 4.2.2), and momentum transport (c.f. 2.1.1, sec. 3.4, and 4.3). A fundamental understanding of materials and transport properties on the submolecular and

molecular scale has finally provided us with a cognitive approach towards engineering that is based on molecular and nanoscale principles.

**Table 5-1:** Classification Schemes of Nanotechnology based on Perspectives

<b>Classification of Nanotechnology</b>		
<i>Perspective</i>	<i>Scheme</i>	<i>Elements/Aspects</i>
<b>Nanomaterials</b>	<b>Number of Dimensions</b> 1,2, and 3 dimensional	Nanoparticles, Nanopores Nanotubes, Nanofilaments Mono-, multi layered, and thin films
<b>Nanomanufacturing</b>	<b>Fabrication Methods</b> Top Down, Bottom Up	Milling, lithography, machining Vapor phase and liquid phase deposition methods, solid-state routes
<b>Nanoscience</b>	<b>Constraints</b> - Internal and External,  - Thermo/Statistical/Rheological,  - Electronic/Structural	Inter- and intramolecular constraints, and interfacial and dimensional constraints  Enthalpic, entropic, organizational, transitional, relaxational, fluctuational constraints  Quantized transport, mobility, fluctuations, interactions



## 6. References and Citations Therein

- <sup>1</sup> D. B. Knorr, T. Gray, and R. M. Overney, *Cooperative and Submolecular Dissipation Mechanisms of Sliding Friction in Complex Organic Systems*, J. Chem. Phys. **129**, 074504 (2008).
- <sup>2</sup> M. Y. He, A. S. Blum, G. Overney, and R. M. Overney, *Effect of interfacial liquid structuring on the coherence length in nanolubrication*, Physical Review Letters **88**, 154302 (2002).
- <sup>3</sup> T. Gray, T. D. Kim, D. B. Knorr, J. D. Luo, A. K. Y. Jen, and R. M. Overney, *Mesoscale dynamics and cooperativity of networking dendronized nonlinear optical molecular glasses*, Nano Letters **8**, 754-9 (2008).
- <sup>4</sup> D. B. Knorr, T. Gray, and R. M. Overney, *Intrinsic Friction Analysis - Novel Nanoscopic Access to Molecular Mobility in Constrained Organic Systems*, Ultramicroscopy **in press** (2008).
- <sup>5</sup> R. M. Overney, E. Meyer, J. Frommer, D. Brodbeck, R. Luthi, L. Howald, H. J. Guntherodt, M. Fujihira, H. Takano, and Y. Gotoh, *Friction Measurements on Phase-Separated Thin-Films with a Modified Atomic Force Microscope*, Nature **359**, 133-5 (1992).
- <sup>6</sup> T. Gray, R. M. Overney, M. Haller, J. Luo, and A. K. Y. Jen, *Low temperature relaxations and effects on poling efficiencies of dendronized nonlinear optical side-chain polymers*, Applied Physics Letters **86** (2005).
- <sup>7</sup> S. Sills, R. M. Overney, W. Chau, V. Y. Lee, R. D. Miller, and J. Frommer, *Interfacial glass transition profiles in ultrathin, spin cast polymer films*, Journal of Chemical Physics **120**, 5334-8 (2004).
- <sup>8</sup> S. Sills, T. Gray, and R. M. Overney, *Molecular dissipation phenomena of nanoscopic friction in the heterogeneous relaxation regime of a glass former*, Journal of Chemical Physics **123** (2005).
- <sup>9</sup> R. Overney and E. Meyer, *Tribological Investigations Using Friction Force Microscopy*, Mat. Res. Soc. Bulletin **18**, 26-34 (1993).
- <sup>10</sup> T. Gray, J. Killgore, J. D. Luo, A. K. Y. Jen, and R. M. Overney, *Molecular mobility and transitions in complex organic systems studied by shear force microscopy*, Nanotechnology **18** (2007).
- <sup>11</sup> R.M. Overney and S. E. Sills, in *Interfacial Properties on the Submicron Scale*, edited by J. Frommer and R. M. Overney (Oxford Univ. Press, New York, 2001), p. 2-23.
- <sup>12</sup> R. M. Overney, D. P. Leta, L. J. Fetters, Y. Liu, M. H. Rafailovich, and J. Sokolov, *Dewetting dynamics and nucleation of polymers observed by elastic and friction force microscopy*, Journal of Vacuum Science & Technology B **14**, 1276-9 (1996).
- <sup>13</sup> R. M. Overney, G. Tindall, and J. Frommer, in *Handbook of Nanotechnology*, edited by B. Bhushan (1439-1453, Heidelberg, 2007).
- <sup>14</sup> S. R. Ge, L. T. Guo, M. H. Rafailovich, J. Sokolov, R. M. Overney, C. Buenviaje, D. G. Peiffer, and S. A. Schwarz, *Wetting behavior of graft copolymer substrate with chemically identical homopolymer films*, Langmuir **17**, 1687-92 (2001).
- <sup>15</sup> A. Karim, T. M. Slawacki, S. K. Kumar, J. F. Douglas, S. K. Satija, C. C. Han, T. P. Russell, Y. Liu, R. Overney, O. Sokolov, and M. H. Rafailovich, *Phase-separation-induced surface patterns in thin polymer blend films*, Macromolecules **31**, 857-62 (1998).
- <sup>16</sup> C. Buenviaje, S. R. Ge, M. Rafailovich, J. Sokolov, J. M. Drake, and R. M. Overney, *Confined flow in polymer films at interfaces*, Langmuir **15**, 6446-50 (1999).
- <sup>17</sup> R. M. Overney, C. Buenviaje, R. Luginbuhl, and F. Dinelli, *Glass and structural transitions measured at polymer surfaces on the nanoscale*, Journal of Thermal Analysis and Calorimetry **59**, 205-25 (2000).
- <sup>18</sup> S. Ge, Y. Pu, W. Zhang, M. Rafailovich, J. Sokolov, C. Buenviaje, R. Buckmaster, and R. M. Overney, *Shear modulation force microscopy study of near surface glass transition temperatures*, Physical Review Letters **85**, 2340-3 (2000).
- <sup>19</sup> E. Meyer, R. Overney, R. Luthi, D. Brodbeck, L. Howald, J. Frommer, H. J. Guntherodt, O. Wolter, M. Fujihira, H. Takano, and Y. Gotoh, *Friction Force Microscopy of Mixed Langmuir-Blodgett-Films*, Thin Solid Films **220**, 132-7 (1992).
- <sup>20</sup> E. Meyer, R. Overney, D. Brodbeck, L. Howald, R. Luthi, J. Frommer, and H. J. Guntherodt, *Friction and Wear of Langmuir-Blodgett-Films Observed by Friction Force Microscopy*, Physical Review Letters **69**, 1777-80 (1992).
- <sup>21</sup> L. Howald, R. Luthi, E. Meyer, G. Gerth, H. G. Haefke, R. Overney, and H. J. Guntherodt, *Friction Force Microscopy on Clean Surfaces of NaCl, NaF, and AgBr*, Journal of Vacuum Science & Technology B **12**, 2227-30 (1994).
- <sup>22</sup> R. M. Overney, T. Bonner, E. Meyer, M. Reutschi, R. Luthi, L. Howald, J. Frommer, H. J. Guntherodt, M. Fujihira, and H. Takano, *Elasticity, Wear, and Friction Properties of Thin Organic Films Observed with Atomic-Force Microscopy*, Journal of Vacuum Science & Technology B **12**, 1973-6 (1994).

- <sup>23</sup> R. M. Overney, H. Takano, M. Fujihira, W. Paulus, and H. Ringsdorf, *Anisotropy in Friction and Molecular Stick-Slip Motion*, Physical Review Letters **72**, 3546-9 (1994).
- <sup>24</sup> R. M. Overney, H. Takano, and M. Fujihira, *Elastic Compliances Measured by Atomic-Force Microscopy*, Europhysics Letters **26**, 443-7 (1994).
- <sup>25</sup> R. M. Overney, H. Takano, M. Fujihira, E. Meyer, and H. J. Guntherodt, *Wear, Friction and Sliding Speed Correlations on Langmuir-Blodgett-Films Observed by Atomic-Force Microscopy*, Thin Solid Films **240**, 105-9 (1994).
- <sup>26</sup> F. Dinelli, C. Buenviaje, and R. M. Overney, *Glass transitions of thin polymeric films: Speed and load dependence in lateral force microscopy*, Journal of Chemical Physics **113**, 2043-8 (2000).
- <sup>27</sup> C. Buenviaje, F. Dinelli, and R. M. Overney, *Investigations of heterogeneous ultrathin blends using lateral force microscopy*, Macromolecular Symposia **167**, 201-12 (2001).
- <sup>28</sup> S. Sills and R. M. Overney, *Creeping friction dynamics and molecular dissipation mechanisms in glassy polymers*, Physical Review Letters **91**, 095501 (2003).
- <sup>29</sup> S. Sills, H. Fong, C. Buenviaje, M. Sarikaya, and R. M. Overney, *Thermal transition measurements of polymer thin films by modulated nanoindentation*, Journal of Applied Physics **98** (2005).
- <sup>30</sup> S. Sills, T. Gray, J. Frommer, and R. M. Overney, in *Applications of Scanned Probe Microscopy to Polymers*, (2005), Vol. 897, p. 98-111.
- <sup>31</sup> S. Sills, R. M. Overney, B. Gotsmann, and J. Frommer, *Strain shielding and confined plasticity in thin polymer films: Impacts on thermomechanical data storage*, Tribology Letters **19**, 9-15 (2005).
- <sup>32</sup> J. P. Killgore and R. M. Overney, *Interfacial mobility and bonding strength in nanocomposite thin film membranes*, Langmuir **24**, 3446-51 (2008).
- <sup>33</sup> R. M. Overney, D. P. Leta, C. F. Pictroski, M. H. Rafailovich, Y. Liu, J. Quinn, J. Sokolov, A. Eisenberg, and G. Overney, *Compliance measurements of confined polystyrene solutions by atomic force microscopy*, Physical Review Letters **76**, 1272-5 (1996).
- <sup>34</sup> M. Y. He, A. S. Blum, D. E. Aston, C. Buenviaje, R. M. Overney, and R. Luginbuhl, *Critical phenomena of water bridges in nanoasperity contacts*, Journal of Chemical Physics **114**, 1355-60 (2001).
- <sup>35</sup> S. Sills, K. Vorvolakos, M.K. Chaudhury, and R. M. Overney, in *Friction and Wear on the Atomic Scale*, edited by E. Gnecco and E. Meyer (Springer Verlag, Heidelberg, 2007), p. 659-76.
- <sup>36</sup> E. Meyer, L. Howald, R. M. Overney, H. Heinzelmann, J. Frommer, H. J. Guntherodt, T. Wagner, H. Schier, and S. Roth, *Molecular-Resolution Images of Langmuir-Blodgett-Films Using Atomic Force Microscopy*, Nature **349**, 398-400 (1991).
- <sup>37</sup> R. Luthi, R. M. Overney, E. Meyer, L. Howald, D. Brodbeck, and H. J. Guntherodt, *Measurements on Langmuir-Blodgett-Films by Friction Force Microscopy*, Helvetica Physica Acta **65**, 866-7 (1992).
- <sup>38</sup> F. Schabert, A. Hefti, K. Goldie, A. Stemmer, A. Engel, E. Meyer, R. Overney, and H. J. Guntherodt, *Ambient-Pressure Scanning Probe Microscopy of 2d Regular Protein Arrays*, Ultramicroscopy **42**, 1118-24 (1992).
- <sup>39</sup> J. Frommer, R. Luthi, E. Meyer, D. Anselmetti, M. Dreier, R. Overney, H. J. Guntherodt, and M. Fujihira, *Adsorption at Domain Edges*, Nature **364**, 198- (1993).
- <sup>40</sup> R. M. Overney, E. Meyer, J. Frommer, H. J. Guntherodt, M. Fujihira, H. Takano, and Y. Gotoh, *Force Microscopy Study of Friction and Elastic Compliance of Phase-Separated Organic Thin-Films*, Langmuir **10**, 1281-6 (1994).
- <sup>41</sup> R. M. Overney, manuscript in preparation.
- <sup>42</sup> T. Gray, C. Buenviaje, R. M. Overney, S. A. Jenekhe, L. X. Zheng, and A. K. Y. Jen, *Nanorheological approach for characterization of electroluminescent polymer thin films*, Applied Physics Letters **83**, 2563-5 (2003).
- <sup>43</sup> T. D. Kim, J. W. Kang, J. D. Luo, S. H. Jang, J. W. Ka, N. Tucker, J. B. Benedict, L. R. Dalton, T. Gray, R. M. Overney, D. H. Park, W. N. Herman, and A. K. Y. Jen, *Ultralarge and thermally stable electro-optic activities from supramolecular self-assembled molecular glasses*, Journal of the American Chemical Society **129**, 488-9 (2007).
- <sup>44</sup> J. H. Wei, M. Y. He, and R. M. Overney, *Direct measurement of nanofluxes and structural relaxations of perfluorinated ionomer membranes by scanning probe microscopy*, Journal of Membrane Science **279**, 608-14 (2006).
- <sup>45</sup> J. P. Killgore, W. King, K. Kjoller, and R. M. Overney, *Heated-tip AFM: Applications in Nanocomposite Polymer Membranes and Energetic Materials*, Microscopy Today **15**, 20-5 (2007).